DOCTORAL THESIS, 2012

Reconstruction of the gradient refractive index of the crystalline lens with optimization methods

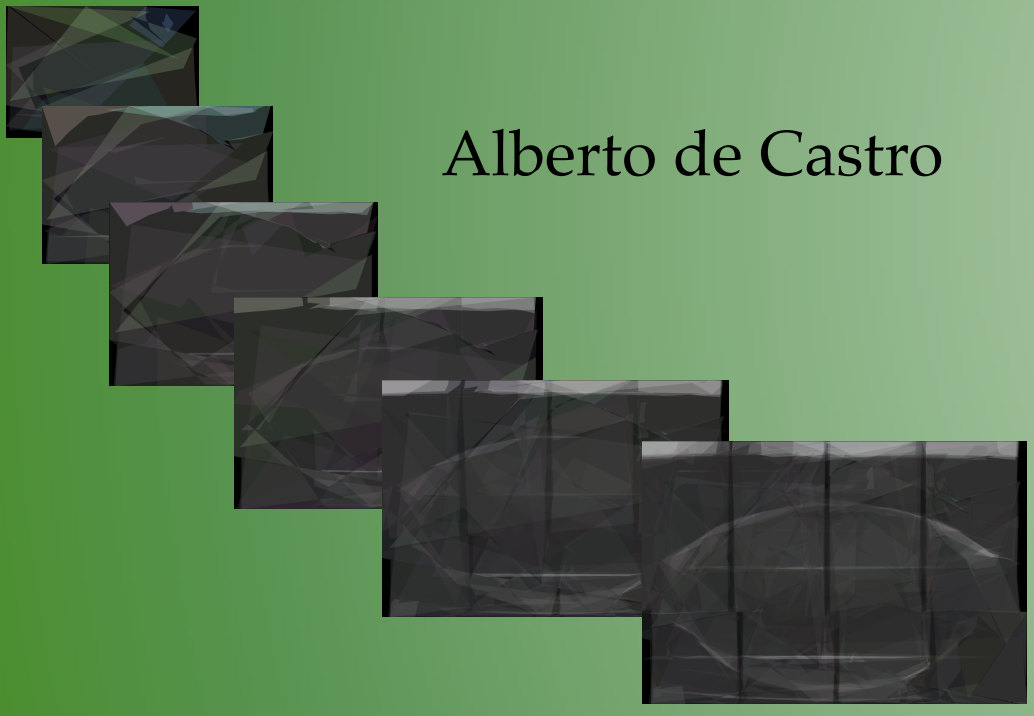

Alberto de Castro

Direction: Susana Marcos
Instituto de Óptica, CSIC

Universidad de Valladolid

INSTITUTO DE OFTALMOBIOLOGÍA APLICADA

TESIS DOCTORAL:

RECONSTRUCTION OF THE GRADIENT REFRACTIVE INDEX OF THE CRYSTALLINE LENS WITH OPTIMIZATION METHODS

Presentada por ALBERTO DE CASTRO ARRIBAS
para optar al grado de doctor
por la Universidad de Valladolid

Dirigida por:
SUSANA MARCOS CELESTINO

Instituto de Óptica “Daza de Valdés” 2012
Cover designed with Roger Alsing’s code:
code.google.com/p/alsing/downloads/

Contents

Page

Table of contents **iii**

Table of contents in Spanish **ix**

Chapter 1. Introduction **1**

1.1 Motivation . . . 3
1.2 Crystalline lens optics and structure . . . 4
1.2.1 Crystalline lens anatomy . . . 4
1.2.2 Crystalline lens shape in vitro . . . 5
1.2.3 Crystalline lens shape in vivo. Changes with age and accommodation . . . 7
1.2.4 Equivalent refractive index . . . 10
1.2.5 Spherical aberration of the crystalline lens . . . 11
1.2.6 Gradient refractive index . . . 12
1.2.7 Gradient index models . . . 12
1.2.8 Chromatic dispersion . . . 15
1.3 Destructive measurements of the gradient refractive index . . . 16
1.3.1 First measurements, before Abbe refractometer . . . 16
1.3.2 Refractometry . . . 18
1.3.3 Measurements over a section of the lens . . . 19
1.3.4 Reflectometry . . . 20
1.4 Non destructive measurements of the gradient refractive index 21
1.4.1 Integral inversion methods . . . 21
1.4.2 Optimization methods . . . 23
1.4.3 Magnetic resonance imaging . . . 25
1.4.4 X-ray phase contrast tomography . . . 26
1.5 Imaging the crystalline lens: optical distortion correction . . . 27

1.6 Open questions on the gradient refractive index 29
1.7 Goals of this thesis 30
1.8 Hypothesis 31
1.9 Structure of this thesis 32

Chapter 2. Methods **33**
2.1 Introduction 34
2.2 Ray tracing algorithm 35
2.2.1 Homogeneous refractive index media 35
2.2.2 Gradient refractive index media 37
2.2.3 Validation of the ray tracing algorithm 39
2.2.4 Effect of Sharma's step size 40
2.3 Optimization algorithm 41
2.3.1 Genetic optimization 42
2.3.2 Hybridation with local search algorithms 45
2.4 Experimental measurements systems 47
2.4.1 Ray Tracing 47
2.4.2 Optical Coherence Tomography systems 48
2.4.3 Optical Coherence Tomography data analysis 53

Chapter 3. Accuracy of the reconstruction with optimization methods from Ray Tracing and Optical Coherence Tomography data **55**
3.1 Introduction 56
3.2 Methods 57
3.2.1 Estimation of experimental errors 57
3.2.2 Studied gradient refractive index models 58
3.2.3 Simulations 59
3.3 Results 61
3.3.1 Limits of the reconstruction algorithm based on laser ray tracing and Optical Coherence Tomography input data 61
3.3.2 Estimation of the experimental errors 61
3.3.3 Influence of experimental errors on the gradient refractive index reconstruction 63
3.3.4 Influence of the surface shape measurement error on the gradient refractive index reconstruction 64
3.3.5 Influence of the ray sampling density on the reconstruction of the gradient refractive index 65

3.4 Discussion 66
3.5 Conclusions 69

Chapter 4. Three-dimensional reconstruction of the crystalline lens gradient index distribution from Optical Coherence Tomography imaging **71**
4.1 Introduction 72
4.2 Methods 73
4.2.1 Gradient refractive index model 73
4.2.2 Merit function 73
4.2.3 Simulations 74
4.2.4 Experimental measurements 76
4.2.5 Optical Coherence Tomography system parameters . . 76
4.2.6 Optical Coherence Tomography images processing . . 76
4.2.7 Crystalline lens surfaces shape and thickness 78
4.2.8 Three-dimensional gradient refractive index reconstruction algorithm 78
4.2.9 Analysis of the influence of the gradient refractive index in the optics of the lens 79
4.3 Results 79
4.3.1 Simulations: Predicted performance of the gradient refractive index reconstruction algorithm 79
4.3.2 Experimental results: Reconstruction of the gradient refractive index of a porcine crystalline lens in 3-D . . . 80
4.3.3 Contribution of the estimated gradient refractive index to the aberrations of the crystalline lens 81
4.4 Discussion 82
4.5 Conclusions 85

Chapter 5. Age-dependent variation of the gradient refractive index profile in human crystalline lenses **87**
5.1 Introduction 88
5.2 Methods 89
5.2.1 Human lens samples 89
5.2.2 Optical Coherence Tomography imaging 90
5.2.3 Image processing 90
5.2.4 Gradient refractive index reconstruction algorithm . . 91
5.2.5 Gradient refractive index model 91

5.3 Results . . . 92
5.3.1 Lens surface shape and thickness . . . 92
5.3.2 Average refractive index . . . 92
5.3.3 Gradient refractive index . . . 93
5.4 Discussion . . . 95
5.5 Conclusion . . . 97

Chapter 6. Distortions of the posterior surface in optical coherence tomography images of the isolated crystalline lens: effect of the lens gradient refractive index 99
6.1 Introduction . . . 100
6.2 Material and methods . . . 101
6.2.1 General description . . . 101
6.2.2 Donor tissue preparation . . . 101
6.2.3 Image acquisition . . . 101
6.2.4 Optical Coherence Tomography image analysis . . . 102
6.2.5 Simulations . . . 103
6.3 Results . . . 106
6.3.1 Experimental results . . . 106
6.3.2 Simulation of the distortion of the Optical Coherence Tomography images . . . 107
6.3.3 Optical Coherence Tomography distortion correction analysis . . . 110
6.4 Discussion . . . 112
6.5 Conclusion . . . 113

Chapter 7. Distortion correction of Optical Coherence Tomography images of the crystalline lens: a gradient refractive index approach 115
7.1 Introduction . . . 116
7.2 Methods . . . 117
7.2.1 Human lens samples . . . 117
7.2.2 Gradient refractive index model . . . 117
7.2.3 Gradient refractive index distortion correction algorithm 118
7.2.4 Data analysis . . . 120
7.3 Results . . . 121
7.3.1 Accuracy in the reconstruction of the posterior lens shape . . . 121
7.3.2 Accuracy in the estimates of lens thickness . . . 121

7.3.3 Influence of Sharma step size 123
7.3.4 Convergence 123
7.4 Discussion 125
7.5 Conclusions 128

Chapter 8. Conclusions **131**

Summary of the chapters in Spanish **135**

Translation of the conclusions to Spanish **151**

Bibliography **155**

Publications during this thesis **169**

Acknowledgments **175**

Índice

Página

Índice en inglés **iii**

Índice en español **ix**

Capítulo 1. Introducción **1**
1.1 Motivación 3
1.2 Óptica y estructura del cristalino 4
1.2.1 Anatomía del cristalino 4
1.2.2 Forma del cristalino in vitro 5
1.2.3 Forma del cristalino in vivo. Cambios con la edad y la acomodación 7
1.2.4 Índice de refracción equivalente 10
1.2.5 Aberración esférica del cristalino 11
1.2.6 Gradiente de índice de refracción 12
1.2.7 Modelos de gradiente de índice 12
1.2.8 Dispersión cromática 15
1.3 Métodos destructivos de medida del gradiente de índice de refracción 16
1.3.1 Medidas anteriores al refractómetro de Abbe 16
1.3.2 Refractometría 18
1.3.3 Medidas en una sección del cristalino 19
1.3.4 Reflectometría 20
1.4 Medidas no destructivas del gradiente de índice de refracción 21
1.4.1 Métodos de inversión de integral 21
1.4.2 Métodos de optimización 23
1.4.3 Imágen de resonancia magnética 25
1.4.4 Tomografía de contraste de fase de rayos X 26

1.5 Corrección de la distorsion en las imágenes del cristalino . . . 27
1.6 Preguntas abiertas acerca del gradiente de índice de refracción 29
1.7 Objetivos . . . 30
1.8 Hipótesis . . . 31
1.9 Estructura de esta tesis doctoral . . . 32

Capítulo 2. Métodos **33**
2.1 Introducción . . . 34
2.2 Algoritmo de trazado de rayos . . . 35
2.2.1 Medios de índice de refracción constante . . . 35
2.2.2 Medios con gradiente de índice de refracción . . . 37
2.2.3 Validación del algoritmo de trazado de rayos . . . 39
2.2.4 Estudio del paso en el algoritmo de Sharma . . . 40
2.3 Algoritmo de optimización . . . 41
2.3.1 Algoritmo genético . . . 42
2.3.2 Hibridación con algoritmos de búsqueda locales . . . 45
2.4 Sistemas de medida experimentales . . . 47
2.4.1 Trazado de rayos . . . 47
2.4.2 Sistemas de Tomografía de Coherencia Óptica . . . 48
2.4.3 Análisis de los datos de Tomografía de Coherencia Óptica 53

Capítulo 3. Precisión de la reconstrucción con métodos de optimización usando datos de trazado de rayos y Tomografía de Coherencia Óptica **55**
3.1 Introducción . . . 56
3.2 Métodos . . . 57
3.2.1 Estimación de los errores experimentales . . . 57
3.2.2 Modelos de gradiente de índice de refracción estudiados 58
3.2.3 Simulaciones . . . 59
3.3 Resultados . . . 61
3.3.1 Límites del algoritmo de reconstrucción usando datos de trazado de rayos y Tomografía de Coherencia Óptica 61
3.3.2 Estimación de errores experimentales . . . 61
3.3.3 Influencia de los errores experimentales en la reconstrucción de la distribución de gradiente de índice de refracción . . . 63

3.3.4 Influencia del error en la medida de la forma de las superficies en la reconstrucción del gradiente de índice de refracción 64
3.3.5 Influencia de la densidad de rayos utilizados para reconstruir el gradiente de índice de refracción 65
3.4 Discusión 66
3.5 Conclusiones 69

Capítulo 4. Reconstrucción tridimentional del gradiente de índice de un cristalino utilizando datos de Tomografía de Coherencia Óptica 71
4.1 Introducción 72
4.2 Métodos 73
4.2.1 Modelo de gradiente de índice de refracción 73
4.2.2 Función de mérito 73
4.2.3 Simulaciones 74
4.2.4 Medidas experimentales 76
4.2.5 Parámetros del sistema de Tomografía de Coherencia Óptica 76
4.2.6 Procesado de las imágenes de Tomografía de Coherencia Óptica 76
4.2.7 Forma de las superficies y espesor del cristalino 78
4.2.8 Algoritmo de reconstrucción del gradiente de índice de refracción tridimensionalmente 78
4.2.9 Análisis de la influencia del gradiente de índice de refracción en la óptica del cristalino 79
4.3 Resultados 79
4.3.1 Simulaciones: precisión del algoritmo de reconstrucción 79
4.3.2 Resultados experimentales: reconstrucción del gradiente de índice de refracción del cristalino en 3 dimensiones 80
4.3.3 Contribución del gradiente de índice de refracción reconstruido a las aberraciones del cristalino 81
4.4 Discusión 82
4.5 Conclusiones 85

Capítulo 5. Variación con la edad del gradiente de índice de refracción en cristalinos humanos 87
5.1 Introducción 88

5.2 Métodos . . . 89
5.2.1 Muestras de tejido humano . . . 89
5.2.2 Imágenes de Tomografía de Coherencia Óptica . . . 90
5.2.3 Procesado de imágenes . . . 90
5.2.4 Algoritmo de reconstrucción del gradiente de índice de refracción . . . 91
5.2.5 Modelo de gradiente de índice de refracción . . . 91
5.3 Resultados . . . 92
5.3.1 Forma de las superficies y espesor del cristalino . . . 92
5.3.2 Índice de refracción promedio . . . 92
5.3.3 Distribución de índice de refracción . . . 93
5.4 Discusión . . . 95
5.5 Conclusión . . . 97

Capítulo 6. Distorsión de la superficie posterior en imagenes de Tomografía de Coherencia Óptica en cristalinos aislados: efecto del gradiente de índice de refracción 99
6.1 Introducción . . . 100
6.2 Materiales y métodos . . . 101
6.2 Descripción general . . . 101
6.2.2 Preparación del tejido . . . 101
6.2.3 Acquisición de imágenes . . . 101
6.2.4 Análisis de las imágenes de Tomografía de Coherencia Óptica . . . 102
6.2.5 Simulaciones . . . 103
6.3 Resultados . . . 106
6.3.1 Resultados experimentales . . . 106
6.3.2 Simulación de la distorsión de las imágenes de Tomografía de Coherencia Óptica . . . 107
6.3.3 Análisis de la corrección de la distorsión en imágenes de Tomografía de Coherencia Óptica . . . 110
6.4 Discusión . . . 112
6.5 Conclusiones . . . 113

Capítulo 7. Corrección de la distorsión de las imágenes de Tomografía de Coherencia Óptica del cristalino considerando el gradiente de índice de refracción 115
7.1 Introducción . . . 116

7.2 Métodos 117
7.2.1 Muestras de tejido humano 117
7.2.2 Modelo de gradiente de índice de refracción utilizado . 117
7.2.3 Algoritmo de corrección de la distorsión producida por el gradiente de índice de refracción 118
7.2.4 Análisis de los datos 120
7.3 Resultados 121
7.3.1 Precisión en la reconstrucción de la forma de la superficie posterior del cristalino 121
7.3.2 Precisión en la estimación del espesor del cristalino . . 121
7.3.3 Influencia del tamaño del paso del algoritmo de Sharma 123
7.3.4 Convergencia del algoritmo 123
7.4 Discusión 125

Capítulo 8. Conclusiones **131**

Resúmen de los capítulos en español **135**

Traducción de las conclusiones a español **151**

Bibliografía **155**

Publicaciones surgidas del trabajo en esta tesis **169**

Agradecimientos **175**

Chapter 1

Introduction

The crystalline of the eye is the biconvex lens suspended behind the iris that contributes to around one third of the total power of the optical system of the eye. The crystalline lens can change its external shape to accommodate allowing the eye to focus to far and near objects in young subjects. The lens looses with age its ability to accommodate, and becomes opaque upon the development of cataract later in life.

The optical properties of the crystalline lens depend not only on the geometry of the external shape, but also on its refractive index. In many species, the refractive index shows a non-homogeneous distribution, with higher index values in the nucleus than in the surface. The precise knowledge of the optics of the crystalline lens and its changes with accommodation and aging are currently limited by the challenges of estimating the gradient refractive index (GRIN) distribution.

Understanding of the role of the gradient index distribution of the crystalline lens on the crystalline lens optics will allow not only to gain deeper insights into the optical properties of the lens, and their variation with accommodation and aging, but also to improve the imaging of the lens with optical techniques in which the posterior lens surface appears distorted by refraction from preceding ocular surfaces and GRIN.

In this thesis we proposed and developed a novel method for reconstruction of the gradient refractive index distribution of non-spherical crystalline lenses and applied it experimentally in porcine and human lenses. We also studied the effects of GRIN on the visualization of the posterior lens surface

with Optical Coherence Tomography and its correction.

In this chapter we present the background and state of the art on crystalline lens optical properties, and the measurement and contribution of GRIN in particular. The geometrical structure of the crystalline lens have been studied in vivo and in vitro, although there are many conflicting reports in the literature, arising from the inherent differences of the lens shape in vivo and in vitro, and the lack of refraction correction in many imaging systems in vivo. There have also been many attempts to measure the gradient index distribution of the lens, although not many studies addressed non-spherical lenses, and the most successful data in human lenses were obtained from non-optical techniques. In this chapter, the most relevant methods described in the literature, used to measure the non-spherical gradient refractive index, both destructive and non destructive, are revised, studying its benefits and drawbacks.

1.1 Motivation

This thesis addresses the study of the optics of the eye, in particular the structure of the crystalline lens, developing methods to estimate the gradient refractive index (GRIN) distribution of the crystalline lens. Although there is a long tradition on modeling the refractive properties of the eye, the optics of the crystalline lens or the specific values of refractive index and its distribution are still debated. The precise knowledge of the gradient index of the crystalline lens will allow a better understanding of the optical properties of the crystalline lens and its contribution to the optical quality of the eye.

The crystalline lens allows to change the refractive state of the eye to accommodate to image objects at different distances. The study of lens accommodative changes has been limited until very recently to the measurement of the surface shape changes. In addition, the lens grows continuously with age and this may affect the refractive index distribution. To describe precisely the optics of the eye, more detailed knowledge of the internal optics of the lens is needed.

The research in this thesis addresses the reconstruction of the crystalline lens gradient refractive index with optimization methods. Following an appropriate modeling of the crystalline lens GRIN, the best fitting parameters to experimental data (and therefore the GRIN distribution) can be retrieved with an optimization algorithm.

The first studies on the refractive index of the crystalline lens used destructive methods, i.e., small sections of the lens were cut and analyzed to measure the index of refraction or the whole eye was frozen and sectioned to analyze a thin layer. There are several more recent studies that propose methods to extract the GRIN structure using experimental data from the whole isolated lens. One of those studies, using Magnetic Resonance Imaging, was also applied in vivo in a single study.

However there are still open questions, since all the methods have its drawbacks. The published values of the refractive index of the center or the edge of the lens reported in literature appear to be very scattered and it is still unknown whether this arises from imprecisions of the measurements or from a real variation across the population. In addition, the distribution of indices, i.e. the way in which the index changes from nucleus to surface is under debate in the scientific community. The challenges of the GRIN measurement have prevented until now from a clear understanding of the role of GRIN in the crystalline lens optics.

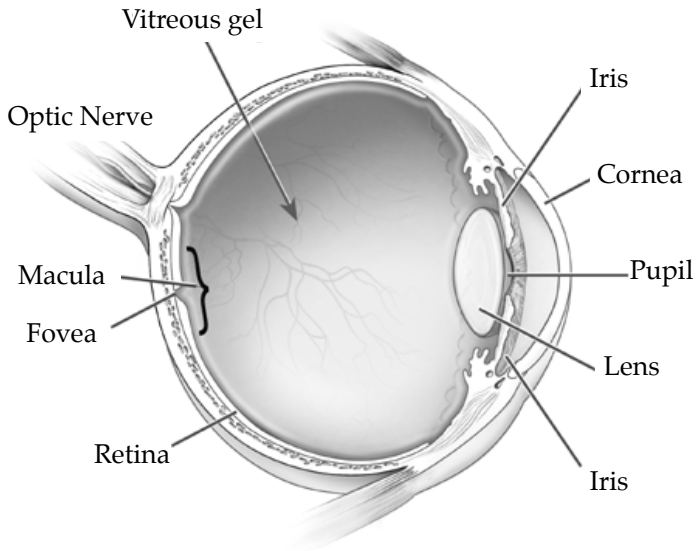

Figure 1.1: Schema of the human eye adapted from an image of the National Eye Institute Catalog (number NEA09). The cornea and the crystalline lens refract the light to form an image on the retina.

1.2 Crystalline lens optics and structure

1.2.1 Crystalline lens anatomy

The eye refracts the light with two optical elements, the cornea and the crystalline lens. An image is formed on the retina where a mosaic of cones and rods samples the light distribution. The diameter of the incoming beam of light is controlled by the iris, which contracts and dilates when needed.

The cornea contributes to around two thirds of the power (around 40 diopters) of the relaxed eye. Although the anterior corneal surface is not a smooth surface due to its cellular structure, an optically smooth surface is achieved with a very thin tear film which covers the cornea. The average shape of this surface is not spherical but flattens in the periphery. The posterior surface of the cornea is less important in optical terms and subtracts around 6 diopters to the power of the cornea due to the lower refractive index in the aqueous humor.

The crystalline lens is a biconvex lens with aspheric surfaces. The lens

is contained in the capsule which is a transparent membrane attached to the ciliary body by the zonules. In the crystalline lens, there is a layer of epithelial cells that extend from the anterior pole to the equator. This lens epithelium is responsible for the continuous growth of the lens throughout life with new epithelial cells forming at the equator. These cells elongate as fibers which under the capsule and epithelium, meet at the sutures of the lens originating its characteristic onion-like layered structure. The different concentration of a type of proteins produces changes in the refractive index across layers. This inhomogeneity is noticeable, and even the first efforts to measure the refractive index of the lens reported that the lens was not composed of a homogeneous material but by a "humor that grows sensibly less and less compact, as you recede from the center" [1]. In fact its refractive index is higher in the center than in the edge.

The young eye is capable to focus near targets by the action of the ciliary muscle which contracts decreasing the tension of the zonules. This lets the crystalline lens to thicken and curve its surfaces, and therefore increase the focal power allowing the eye to focus at different distances, i.e. allowing the eye to accommodate. It is well known that the crystalline lens looses this ability with age in a condition known as presbyopia. The loss of accommodation affects the whole population beyond 45 years but there is no satisfactory solution for its correction. Improved solutions of presbyopia, for example in the form of accommodative intraocular lenses, require a profound understanding of the natural crystalline lens properties and their contribution to accommodation

1.2.2 Crystalline lens shape in vitro

Probably the first reports on the shape of the crystalline lens were presented by Helmholtz [1924] using Helmholtz ophtalmometer in 1855. He studied the magnification of the reflected images on the lens surfaces.

In the seventies, some studies [Parker, 1972; Howcroft and Parker, 1977] used eye samples frozen before lens extraction to avoid deformation and

[1] Complete sentence from Wintringham [1740]: *Hence also appears the reason, why the crystalline humor is not an uniform density and consistence thro' all its parts, but grows sensibly less and less compact, as you recede from the centre towards the circumference, insomuch that as the anatomist Morgagani has assured us, and indeed any one from his own observation of the crystallines of men and other animals may be convinced, the substance immediately under its Tunic is of so liquid as a nature, as to flow out upon making the least incision into it.*

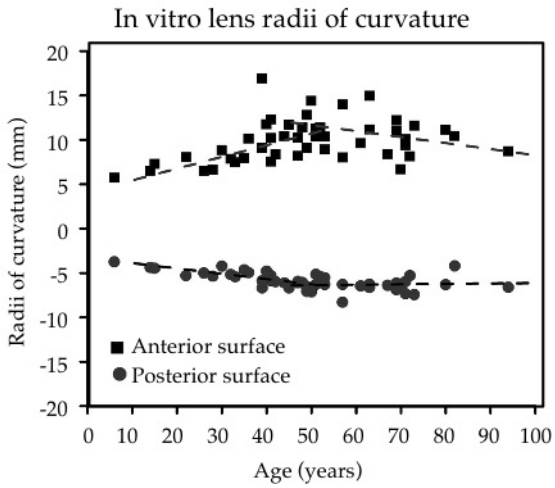

Figure 1.2: In vitro crystalline lens radii of curvature as a function of age measured with Shadowphotography. Reproduction from Borja et al. [2008] (Investigative Ophthalmology & Visual Science).

cut a thin section to study its shape. Today, digitalization of images of the sagittal and meridional plane of the excised lens are the usual technique to study the shape, central thickness and diameter of the in vitro crystalline lens [Pierscionek and Augusteyn, 1991; Glasser and Campbell, 1999; Manns et al., 2004; Rosen et al., 2006; Borja et al., 2008]. In most of these works, the variation of thickness and radii with age exhibited a change of tendency on the onset of presbyopia (40-60 years). Below this age, the radii of curvatures of the crystalline lens increased and then decreased slightly after the appearance of presbyopia. It has been argued [Borja et al., 2008] that these changes are associated to the age-related loss of accommodation. This finding is consistent with the fact that the lens in vitro appears maximally accommodated.

Data of the asphericity of the in vitro surfaces of the lens were first reported in the studies on frozen crystalline lenses [Parker, 1972; Howcroft and Parker, 1977]. These works found that the anterior lens surface was hyperbolic while the posterior surface was parabolic. However, the tissue handling and freezing of the lens may have affected the measurements [Manns et al., 2004]. Recent experimental results with topographers or digital photographs of sagital sections [Manns et al., 2004; Rosen et al., 2006]

found a high variablilty between eyes although on average the anterior lens surface steepened towards perifery. The asphericity values for posterior surface found were positive and negative.

The power of the in vitro lens was measured in different studies [Sivak and Kreuzer, 1983; Glasser and Campbell, 1998, 1999; Borja et al., 2008] and in some of them [Glasser and Campbell, 1998; Borja et al., 2008] the accommodation was simulated using a stretching system. Since not only the shape but also the power measured with these techniques are in a good agreement with in vivo measurements it can be assumed that removing zonular tension does not increase the power of the lens significantly compared with the maximum accommodated state in the in vivo eye [Borja et al., 2008].

1.2.3 Crystalline lens shape in vivo. Changes with age and accommodation

The first systematic studies of the shape of the in vivo crystalline lens were performed usign phakometry systems. The third and fourth Purkinje images are formed by reflection in the anterior and posterior crystalline lens surfaces and their magnification can be used to estimate the crystalline lens radii of curvature. Several algorithms [Smith and Garner, 1996; Garner, 1997] have been proposed to estimate, using these reflections, not only the radii of curvature of the anterior and posterior surfaces but also the power of the lens or its tilt and decentration with respect to the optical axis of the eye. Different works [Wulfeck, 1955; Sorsby et al., 1961; Veen and Goss, 1988; Phillips et al., 1988; Mutti et al., 1992; Rosales and Marcos, 2006; Tabernero et al., 2006; Rosales et al., 2008; Atchison et al., 2008] have studied the shape, power, and tilt and decentration of the crystalline lens using Purkinje images.

A Scheimpflug camera can record images of the anterior segment of the eye but since its magnification is not constant and each surface is seen through the previous refractive surfaces, these suffer geometrical and optical distortion. Correction of the images with the approximation of a constant refractive index in the lens allowed the study of the shape of the crystalline lens and its change with age and accommodation [Brown, 1973a, 1974; Koretz et al., 1984, 2001; Dubbelman et al., 2003, 2005b; Rosales et al., 2006; Rosales and Marcos, 2009].

Ultrasound-based techniques are commonly used in clinical applications to measure the intra ocular distances. With its extension to three dimensions (ultrasound biomicroscopy) images of the anterior segment of the eye

have been possible [Silverman, 2009]. Its precision in the measurement of distances allowed the study of the change of thickness of the lens with age and accommodation [Beers and van der Heijde, 1996] but, to our knowledge, there are not reports of quantitative data on the shape of the crystalline lens with this instrument.

Optical Coherence Tomography (OCT) has been extensively explored to study the retina. In the last decade, this technique has been increasingly used to image the anterior segment [Goldsmith et al., 2005; Grulkowski et al., 2009]. Again, the images are distorted since each surface is seen through the preceding surfaces, but correction algorithms [Westphal et al., 2002; Podoleanu et al., 2004; Ortiz et al., 2010] can be applied to extract the topography of the anterior crystalline lens surface, and a homogeneous index can be approximated to correct the distortion in the posterior surface of the lens.

Magnetic resonance imaging is capable of producing undistorted images of the whole eye in vivo and was used to study the shape of the anterior segment of the eye [Koretz et al., 2004]. However, a disadvantage of this method is its low resolution. Radii of curvature of anterior and posterior surfaces were reported although the resolution was not enough to study the conic constant of the surfaces.

In vivo measurements of the radii of curvature of the crystalline lens surfaces in unaccommodated lenses have been shown to decrease constantly in anterior and posterior surfaces of the crystalline lens with age. This decrease appears more significant in the anterior surface (radii values from around 12 mm at 20 year old subjects to 9 mm at 70) than in the posterior (between 6.5 mm at 20 and 5.5 mm at 70 year old subjects). The thickness increases with age from around 3.5 mm in young subjects to more than 4.5 mm in old subjects. If the index of the lens was homogeneous this would result in an increase of power of the lens, yet there is not a tendency for myopia (so called lens paradox [Brown, 1974]), the changes in the GRIN distribution with age may be the reason behind the effect [Moffat et al., 2002b].

Studies in vivo on the change of the lens surfaces with accommodation [Koretz et al., 1984; Dubbelman et al., 2003, 2005a; Rosales et al., 2006, 2008] showed average changes in anterior and posterior radii, from around 12 and 6.5 mm (relaxed accommodation) to 7.5 and 5 mm (fully accommodated lens) respectively, and changes in lens thickness of around 0.5 mm over a 6 D accommodative range

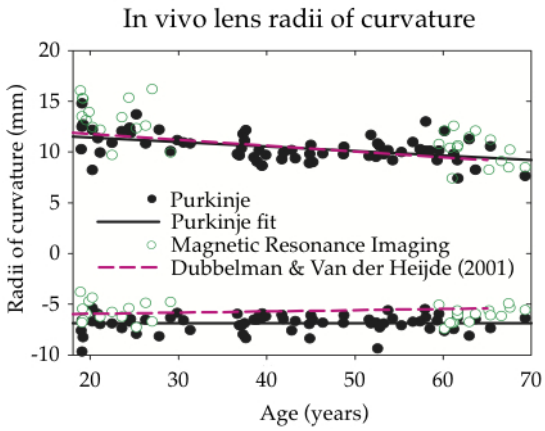

Figure 1.3: In vivo crystalline lens radii of curvature as a function of age measured with Phakometry and MRI. Scheimpflug fittings are shown for comparison purposes. Reproduction from Atchison et al. [2008] (Journal of Vision).

The measurement of the asphericity of the lens surfaces in vivo is still a challenge since the image of the crystalline lens is limited by the diameter of the iris. Phakometry is generally limited to radii of curvature measurements only. Scheimpflug imaging has additional pupillary limitations to the visualization of the lens posterior surface. In addition, posterior asphericity estimates are limited by the assumption of constant refractive index in the lens. As mentioned above, the resolution of MRI is poor to attempt conic fittings of the lens surfaces. Anterior chamber OCT may be the best technology to quantify the lens shape [Grulkowski et al., 2009; Gambra et al., 2010] but application to the crystalline lens is recent, and the number of tested subjects is still limited. Brown [1973a, 1974] published data obtained from Scheimpflug images and reported that the curvature of the anterior lens surface decreased towards the periphery, while the posterior surface steepened toward periphery. In a more recent work Koretz et al. [1984] found a good fit of the surfaces using parabolas. Dubbelman and van der Heijde [2001] found that both anterior and posterior surface were hyperbolic, i.e. lens surface steepened towards periphery.

1.2.4 Equivalent refractive index

In some of the studies, the contribution of the GRIN to the total lens power was quantified with a homogeneous index known as the equivalent refractive index. This is defined as the refractive index of a homogeneous lens with the same shape and dioptric power of the crystalline lens.

While Glasser and Campbell [1998] found no age dependence of the in vitro lens equivalent refractive index, Borja et al. [2008] measured the focal length using a commercial lens meter and a custom developed optical system based on the Scheiner principle and, despite significant variability, found a decrease in the equivalent refractive index, more clearly in younger lenses. The change of this parameter indicates that the change of the crystalline lens optics with age is not only due to the change of its shape but also to the GRIN distribution. The relative surface refractive contribution is still under discussion. Borja et al. [2008] found that surfaces contribute only with a 40% to total lens power. This percentage was found to be nearly constant for the different age groups.

The in vivo equivalent refractive index was studied in unaccommodated crystalline lenses with Scheimpflug [Dubbelman and van der Heijde, 2001] and Purkinje images [Garner and Smith, 1997; Atchison et al., 2008]. These studies also found a decrease in the equivalent refractive index with age, as reported in vitro.

The change of this equivalent refractive index with accommodation was studied with Phakometry and Scheimpflug imaging. Garner and Smith [1997] found a constant equivalent refractive index with accommodation using Phakometry. Dubbelman's studies using Scheimpflug imaging [Dubbelman et al., 2005a] reported a significant increase in the equivalent refractive index with accommodation. However, Hermans et al. [2008] incorporated the accommodative lag to the calculations and reported an almost constant equivalent refractive index consistent with that of Garner. Hermans et al. [2008] also studied the shape of the nucleus of the lens and concluded that the GRIN could be approximated with a two-compartment model with a homogeneous refractive index in the nucleus and in the cortex, which would not change significantly with accommodation.

1.2.5 Spherical aberration of the crystalline lens

The spherical aberration of the crystalline lens was studied in excised lenses by Sivak and Kreuzer [1983] who found both positive and negative spherical aberration in the human lenses of different subjects. Glasser and Campbell [1998, 1999] found that the spherical aberration was negative in young lenses and positive in old crystalline lenses. Animal models such as porcine or macaque were also studied in vitro. Sivak and Kreuzer [1983] reported that porcine lenses were almost free of spherical aberration. Vilupuru and Glasser [2001] studied 20 porcine lenses and found positive and negatives values of spherical aberration unrelated to any other measured variables. Roorda and Glasser [2004] measured negative spherical aberration in one single porcine lens and Acosta et al. [2010] measured the aberrations of 12 porcine lenses with a point-diffraction interferometer and found negative spherical aberration in all of them. Wong et al. [2007] studied the aberration before and after refilling the lens with a silicon oil and found a change in the sign of spherical aberration, from negative in the natural lens to positive in the refilled one. A change toward negative spherical aberration with simulated accommodation was found in macaque lenses [Roorda and Glasser, 2004].

The studies of the spherical aberration of the lens in vivo have involved different types of measurements. Some studies measured the aberrations of the whole eye while neutralizing the aberrations of the cornea [Young, 1801; Millodot and Sivak, 1979]. Most studies have measured the aberrations of the internal optics by subtracting corneal aberrations (generally estimated from corneal topography) from total aberrations. Jenkins [1963] measurements suggested that the spherical aberration of the lens was approximately zero. El-Hage and Berny [1973] found a negative spherical aberration in a single subject study. Millodot and Sivak [1979] studied 20 subjects and found, on average, a positive spherical aberration similar to the one of the cornea. Tomlinson et al. [1993] found negative spherical aberration in the crystalline lens in the 20 subjects of their study. and Smith et al. [2001] also found negative values in the 26 tested subjects. Smith and Atchison [2001] speculated that a decrease in the power of the crystalline lens due to changes in its gradient refractive index would increase the spherical aberration. Artal et al. [2002] found that in most of the younger subjects, total ocular spherical aberration was lower than corneal spherical aberration suggesting a compensatory mechanism that would fail in elder subjects. This behavior was also reported by Barbero et al. [2002].

1.2.6 Gradient refractive index

Many theoretical studies have modeled the optics of the eye. The most relevant eye models including a GRIN distribution to simulate the lens optical performance are presented in section 1.2.7. Some of these GRIN models will be evaluated in this thesis to address the precision of the reconstruction and to find the best gradient index which fits the experimental data obtained from in vitro crystalline lenses.

The different techniques used over time to measure the refractive indices and to reconstruct the GRIN distribution of the crystalline lens are described in section 1.3 and 1.4. The methods have been divided following the natural classification of destructive and non-destructive. First of all, because although destructive methods contribute with valuable information, any manipulation of the crystalline lens can affect the hydration of the tissue and therefore the refractive index can be altered, and second, since only the non-destructive methods could be envisioned in vivo.

1.2.7 Gradient index models

There are numerous proposals of theoretical eye models in the literature. These are built with the purpose, among others, of better understanding the role and relative importance of the optical elements or to make predictions on the optical and image quality upon changes, for example, refractive surgery or implantation of an intraocular lens.

The first eye model was built in the 17^{th} century (Huygens' simplified eye in 1653). However, the incorporation of a GRIN distribution in the crystalline lens of model eyes is relatively recent. Gullstrand [Helmholtz, 1924] built an eye model with a GRIN in the lens taking as reference the values reported by Freytag (1907) among others. Using this model, Blaker [1980] simulated accommodation with linear changes of the GRIN parameters and used a parabolic function to describe the GRIN. Pomerantzeff et al. [1971] simulated the GRIN distribution as a large number of shells with different curvature, thickness and refractive index each and build a wide angle optical eye model. The input data to build this model were the mean focal length and spherical aberration of the eye.

Smith et al. [1991] proposed the modeling of the crystalline lens with elliptical or bi-elliptical models fitting experimental data from Pierscionek and Chan [1989] to power functions or polynomial distributions up to sixth or-

der. Atchison and Smith [1995] studied this model and described a method to transform a gradient index distribution into a shell model with different refractive indices. Although this was used as a method to study the paraxial behavior of the lens, they noticed that these shell models were not appropriate to study the aberrations associated with the GRIN distributions.

Al-Ahdali and El-Messiery [1995] proposed a lens GRIN model with 300 layers, and used an exponential function to describe the change in the refractive index through the layers. The proposed model had three free parameters to simulate the increase in thickness, curvature and refractive index of each layer. Popiolek-Masajada [1999] studied the influence of the shell stucture in the refractive state and spherical aberration of this model.

Pérez et al. [2003] modeled the refractive index distribution in the paraxial region and calculated theoretically its paraxial power, cardinal points, the dependency of paraxial properties on changes of the shape of the axial profile [Pérez et al., 2005] and its magnification, transmitance and point spread function [Rama et al., 2005; Flores-Arias et al., 2006]. Flores-Arias et al. [2009] introduced the studied crystallline lens in a model eye to evaluate the paraxial properties of the GRIN model of the human eye and compare them to a homogeneous indices model.

Liou and Brennan [1997] fitted the data by Pierscionek and Chan [1989] assuming different weights in the fitting from nucleus to surface because of the increasing uncertainty of the measurement at greater distances from the lens center, and proposed a parabolic profile to model the GRIN distribution.

Navarro et al. [2007a] proposed a parametric model where anterior and posterior hemispheres did not intersect at the equator but on a conicoid surface. The GRIN was modeled with the power equation proposed by Smith et al. [1992]. The four free parameters of the model (refractive index of surface, refractive index of the center of the lens, thickness of the anterior hemisphere and exponential value of the power equation) were fitted to data from Jones et al. [2005] for different ages, and found that the exponent of the power equation changed with age following a fourth-order power law. In a companion study, Navarro et al. [2007b] used Scheimpflug's data [Dubbelman et al., 2001, 2005a] to incorporate in the model changes in surface and GRIN distribution with age and accommodation.

Goncharov et al. [2007] proposed a GRIN model described with a fourth-order equation in axial and meridional axis (only pair power terms in meridional axis). They presented three models with increasing complexity (2, 3 and 4 free variables) for ages of 20 to 40 years and fitted free parameters to

match the spherical aberration of the Indiana eye model [Thibos et al., 1997] or Liou and Brennan [1997] eye model. Wavefront root mean square off-axis were in good agreement with the predictions of Navarro's homogeneous media eye model [Escudero-Sanz and Navarro, 1999].

Díaz et al. [2008, 2011], studied the possibility of using sinusoidal functions to model the GRIN on axis, with a parabolic decrease in the meridional plane. An eye model with such a profile fitted chromatic difference of focus, on-axis MTF data and accounted for the chromatic aberration and the age related changes in spherical aberration.

Recently, Campbell [2010] discussed the advantage of a shell model to account realistically for the anatomy of the crystalline lens. The model was based on cell layers, with constant index and thickness, added progressively to an embryonic lens model. As the lens ages it is assumed that the innermost layers dehydrate and their indices of refraction approach that of the nucleus, as a result the gradient index of refraction moves toward the lens surface with age.

Manns et al. [2010] built in 2010 a simple model where the center of the lens was placed at a distance from the anterior surface vertex equal to 0.41 times the lens thickness [Rosen et al., 2006]. The GRIN distribution was modeled with a power equation, similar to Smith et al. [1992] previous reports, in all directions from the center of the lens to the surfaces, described by conics:

$$n(x, y, z) = n_N - \Delta n \cdot \left(\frac{\rho(x, y, z)}{\rho_S(x, y, z)} \right)^p , \tag{1.1}$$

where n_N is the nucleus refractive index, Δn is the difference between nucleus and surface refractive index, $\rho(x, y, z)$ is the distance from a point to the center of the lens and $\rho_S(x, y, z)$ is the distance from the center to the surface in that direction. The model had constant index in the surfaces, and the variables were the shape and thickness of the lens, the values of refractive index in nucleus and surface and the exponential decay constant that can vary from optical to meridional axis (Manns personal communication).

Bahrami and Goncharov [2012] proposed a model where the external geometry were defined by conic equations with a higher-order aspheric term, the iso-indicial surfaces of the model follow the surfaces shape and the GRIN distribution was described with a power law. They derived the analytical equations for paraxial ray tracing and calculated its optical power and third-order monochromatic aberration coefficients.

1.2.8 Chromatic dispersion

The crystalline lens medium has a significant impact on the chromatic aberration of the eye. Knowledge of the chromatic dispersion of the lens is also of practical interest, as usually the experimental data combine results gathered from instruments that work at different wavelengths. However, there are very few reports in the literature on the dispersion in crystalline media. Palmer and Sivak [1981] measured the index of the peripheral and central material of lenses of different species with a Pulfrich refractometer at wavelengths between 410 and 680 nm, although the study only included one human lens. In a later study, Sivak and Mandelman [1982] presented additional data using Pulfrich and Abbe refractometers and six human lenses, although the standard deviation of the values were very high. Pierscionek et al. [2005] reconstructed the GRIN of the meridional plane of porcine lenses with 532 and 633 nm, using a ray tracing method and found, as expected, small differences.

For the purpose of building a chromatic eye model, Le-Grand [1964] took intermediate values between the power measurements reported by Knust (1895) and Polack [1923], and Navarro et al. [1985] used data from Polack [1923].

Atchison and Smith [2005] reviewed recently the chromatic dispersion of the ocular media in human eyes. They proposed a variation of the index of refraction of the crystalline lens fitting the data reported by Le-Grand [1964] and Navarro et al. [1985] to the Cauchy equation:

$$n(\lambda) = A + B/\lambda^2 + C/\lambda^4 + D/\lambda^6 + \dots. \tag{1.2}$$

The reference refractive indices used were those of surface and core of Gullstrand model at 555 nm. However they observed that if the refractive index of reference was changed, the ratio of the higher to lower index values was almost constant. Therefore if the index is calculated at a wavelength λ_1, $\bar{n}(\lambda_1)$, they proposed to use a constant scaling formula to calculate the index at a wavelength λ_2, $\bar{n}(\lambda_2)$

$$\bar{n}(\lambda_2) = \bar{n}(\lambda_1) * \frac{n(\lambda_2)}{n(\lambda_1)}, \tag{1.3}$$

where $n(\lambda_1)$ and $n(\lambda_2)$ are the index calculated with the Cauchy equation proposed.

The values of the constants were calculated for high and low crystalline lens refractive indices:

	A	B	C	D
High	1.389248	$6.521218\ 10^3$	$-6.110661\ 10^8$	$5.908191\ 10^{13}$
Low	1.369486	$6.428455\ 10^3$	$-6.023738\ 10^8$	$5.824149\ 10^{13}$

For the purposes of this thesis, following Uhlhorn et al. [2008] calculations, we will use the Cauchy equation to transform from group refractive index to phase refractive index using the relation Saleh and Teich [1991]:

$$n_g(\lambda_0) = n(\lambda_0) - \lambda_0 \frac{dn}{d\lambda}(\lambda_0), \tag{1.4}$$

where $n_g(\lambda_0)$ is the group refractive index at the measurement wavelength, $n(\lambda_0)$ is the phase refractive index and $\frac{dn}{d\lambda}$ is the slope of the dispersion curve calculated from the Cauchy equation. The phase refractive index at the measurement wavelength can be converted to the desired wavelength using the linear relation suggested by Atchison and Smith (equation 1.3).

1.3 Destructive measurements of the gradient refractive index

1.3.1 First measurements, before Abbe refractometer

The literature of the last decades[2] usually refers as first measurements those with Abbe refractometers. However, there is a significant body of research before the patent of Abbe in 1874. These first measurements were always destructive and many of the refractive indices values are far from reasonable with actual knowledge of the lens. However, it is remarkable that the first publications reporting experimental GRIN data (in the ox) go back three centuries.

History texts [Wade, 1998] explain that prior to Kepler, the lens was considered to be the organ of light-perception of the eye. Celsus described in the year 29 a "drop of humor" in the center of the eye that, according to the theories of vision at the time had to be the organ from which proceed

[2]Many of the reference of this first measurements were extracted from pages 41 and 42 of Huggert's book [Huggert, 1948]. Since many of them were unaccessible, they will not be listed in the references of this thesis but can be consulted in the text by Huggert.

the faculty of vision. Platter (1583) and later Kepler (1604) stated that the lens was transparent and that an image was formed on the concave surface retina. In 1619, Scheiner estimated the index of the lens to be equal to that of glass while fluids had the same refractive power as water.

It seems that the first estimates of the refractive index of the lens derives from Hauksbee [1710]. He obtained a value of 1.464 by placing "lens substance" in a cavity in a prism and measuring the deviation of a ray passing through. He pointed out the difficulty of determining the exact value due to the increasing optical density of the lens towards the center. This was observed also by Leeuwenhoek, Petit and Porterfield in the same century. Porterfield reported a value of 1.3645 for the lens refractive index. Other estimations were made in first half of XVIII century by Pemberton, Jurin, Helsham, Wintringham, Steno and Petit. Wintringham [1740] reported an index of 1.4026.

Wollaston [Chossat, 1818] used in 1802 total reflection to achieve more accurate estimations of the index of the lens. He measured the intensity of the reflection ray and searched for the angle in which this intensity was maximum, this is, the critical angle. The values obtained by Wollaston in a cattle lens were 1.447 in the core and 1.38 in the surface. Young [1801] applied the same method to investigate in human crystalline and obtained a core index of 1.4026. Young was probably the first author to stress the importance of the structure of the refractive index with regard to refraction of the crystalline lens.

Chossat [1818] reported values of 1.338, 1.395 and 1.42 for superficial, intermediate and nucleus layer of human crystalline lens respectively. He used a method developed by Brewster, where the examined medium was placed between a convex lens and a plane glass-plate. This system was used as an objective in a microscope and the refractive power of the system was estimated. Senff reported 1.374 and 1.453 for surface and nucleus layers and 1.539 for total index with the same method. Engel examined 22 human lenses, but the data showed high intersubject variability (total index varying between 1.2734 and 1.547). Freytag critized that lenses in that study had been exposed to different treatments and times after death.

Krause improved Brewster's method by measuring the size of the images instead of the focal distances. He reported main values of 1.40, 1.42 and 1.45 for outer, intermediate layer and core respectively, although again, the data showed high dispersion (refractive index between 1.3431 and 1.4541). Helmholtz used a similar system, and estimated a value of 1.4189 for the

outer layer of the lens. Further attempts were made by Woinow, Mauthner and Becker, among others, before Abbe designed his refractometer in 1874.

1.3.2 Refractometry

Abbe's refractometer is, like Wollaston's method, based on the measurement of the critical angle of refraction between glass and the medium under test. However, instead or measuring the maximum intensity of the reflected ray, Abbe measured the minimum intensity of the refracted ray. The measurement error was calculated to be around 0.0002 (Mathiessen, Valentin, Moennich, Freytag). Almost all the authors suggested that estimating the refractive index using the Abbe refractometer was difficult, since often, no sharp border-line was obtained but a more or less broad band.

Perhaps, the first measurements of refractive index of human lenses with the Abbe refractometer were performed by Aubert, who measured the two crystalline lenses of a 50-year old man. Results were 1.3953 and 1.3967 for the outer layer, 1.4087 and 1.4067 for the intermediate layer and 1.4119 and 1.4093 for the core of the lens. During the years 1876 to 1891 Mathiessen carried out measurements on different animals and human cadaver lenses, and obtained values of 1.3880, 1.4060 and 1.4107 for surface, intermediate layer and nucleus respectively in the human. He found that the refractive index from the surface to the center of the lens increased following a parabolic curve. He showed the same phenomenon in dried gelatin balls which were left to swell in water.

Heine examined human lenses and found that the anterior and posterior lens poles had equal refractive indices and that the index of the lens surface was not equal in all parts but higher at the poles than at the equator.

Freytag published an extensive study with measurements on animal models and human lenses in 1907. The main conclusions of his work were (1) the refractive indices of the surface increase from the lens equator toward the poles, (2) the surface values do not change with age, (3) nucleus refractive index increases considerably with age but this tendency is least pronounced in man, (4) a smaller number of 'steps' occur in the index curves of young lenses than in older ones (5) the maximum refractive index is more often observed slightly closer to the anterior lens pole than to the posterior one.

Huggert [1948] discussed two different views on the refractive index of the lens surface. According to one, the refractive index should be uniform in the whole lens surface. According to the other, the refractive index

should decrease continuously from the poles towards the equator. Using Abbe refractometetry, Freytag reported large changes (1.385 for the pole, 1.375 for the equator), which was opposite to Matthiessen and Moennich's conclusions. Changes in surface refractive index were also found by Zehender (1877), Bertin-Sans (1893), Heine (1898), Speciale-Cirincione (1913) and Tagawa (1928). However, Huggert did not found any significant difference across the surface reporting values between 1.382 and 1.392 for the center of the lens surface, and around 1.373 and 1.383 out of the central zone. He also noted that Freytag's values of refractive index varied greatly (1.375-1.398 in polar and 1.368-1.391 in equator). Sixty years later this discussion is still not closed and the scientific community has not a uniform opinion on this subject.

1.3.3 Measurements over a section of the lens

Schlieren interferometry

Nakao measured rabbit [Nakao et al., 1968] and human [Nakao et al., 1969] crystalline lenses with a technique based on Schlieren interferometry previously developed by Shinoda et al. [1964]. The lenses were frozen and a layer (between 0.5 and 1 mm thickness) was cut off with a micro-tome. Fraunhofer diffraction pattern was studied when introducing the lens section in a simple optical system. This allowed to show the areas with the same gradient of refractive index. Abbe refractometry was used to determine the refractive index in the center of the lens.

Densitometry

Densitometry techniques are based on the fact that in a solution the refractive index and the concentration of the solute can be related in many cases linearly. Philipson [1969] determined the concentration of proteins in frozen slices of rat crystalline lenses using a quantitative microradiographical technique, and reported values of gradient index in the rat lens at different ages. He showed that the results were in good agreement with refractometric measurements in isolated parts of the lens and concluded that in normal transparent lenses (non cataractous lenses), the changes in refractive index were always regular and continuous, except for the intracellular variations. He found a constant surface refractive index with age, 1.39, and an increas-

ing refractive index of the nucleus of the lens, from around 1.40 to 1.50 in the older rats (around 800 days).

Fagerholm et al. [1981] applied in 1981 the method to 21 human lenses of different ages along the lens axis. The lenses were frozen in liquid nitrogen to about -140 °C and sectioned to a thickness of about 20 μm. In terms of protein concentration no significant change with age was found either at the center of the lens or in anterior sub-capsular cortex but a statistically significant increase was found in posterior sub-capsular cortex. The measurements were consistent with a clear lens nucleus at all ages, but the study did not report refractive index values.

Pulfrich refractometry

Jagger [1990] presented in 1990 a work where refractive index distributions of isolated cat lenses were measured with a modification of Pulfrich refractometer. The lenses were frozen and cut, and the refractive index was measured in the surface of the sample. A prism was placed on the frozen cut lens surface, and the lens was then defrozen and illuminated. As surface was observed through the vertical prism face, the critical angle for internal reflection at the lens-prism marked the areas of the lens which were visible or not. Moving the camera, the different iso-indicial surfaces could be observed.

1.3.4 Reflectometry

Pierscionek [1993] used a fiber optic sensor to estimate the refractive index on the surface of the crystalline lens. The amount of light reflected in the interface between two media depends on the refractive index difference between them. The technique was applied to one sheep lens and three rabbit lenses. Pierscionek found differences between species: while in the sheep an increase in refractive index with distance to the pole and no differences between anterior and posterior surface refractive index value were found, in the rabbit the index was constant over the surface and there was a difference between anterior and posterior surface refractive index of more than 0.02.

In 1994 Pierscionek presented results using the same methodology in bovine [Pierscionek, 1994a] and human [Pierscionek, 1994b] lenses and concluded that surface refractive index was constant with age in both bovine and human (age range 27-84 year-old lenses) lenses. For the human lenses, the

study reported a higher value of refractive index in anterior surface (between 1.346 and 1.379) than in posterior surface (between 1.345 and 1.364).

In a subsequent study on human lenses [Pierscionek, 1997] the index of refraction along the equatorial and sagittal planes were measured in 14 crystalline lenses. In young and in one older lens, the equatorial refractive index profile was found to be different than the sagittal in a normalized scale, i.e. the concentric, iso-indicial contours model was found not to be accurate, at least for young lenses. The equator index increased with age, but not the poles refractive index (a small correlation was found for anterior pole refractive index). The indices of anterior and posterior poles were found to be in the same range (between 1.385 and 1.410).

1.4 Non destructive measurements of the gradient refractive index

1.4.1 Integral inversion methods

For a spherically symmetric gradient index lens, in which the refractive index distribution depends only on the distance from the lens center, the angle of deflection of an incident ray can be expressed as a function of the refractive index distribution. The inverse problem was solved by Chu [1977] by relating the exit angles of beams and the refractive index distribution into the form of an Abel inversion integral.

The method could be generalized [Barrell and Pask, 1978] to sightly elliptical GRIN distributions. Campbell [1984] reported data on a rat lens, although the method required matching the external media and the surface refractive indices, as well as using iso-indicial concentrical surfaces GRIN model.

Chan et al. [1988] expanded the method to apply it to non-spherical crystalline lenses by measuring the refraction of the rays in the equatorial plane of the lens, where the isoindicial contours of the lens were modeled as a family of concentric ellipses. The result was projected to the rest of the lens assuming constant index in the lens boundary. A ray tracing was performed along the equatorial plane to asses the accuracy of the result. The method is limited by the matching needed between surface and media refractive index but, with some approximations, it was proved [Chan et al., 1988] that, if differences were small, the result was accurate. Pierscionek

et al. [1988] measured a set of 11 human lenses with ages ranging from 16 to 84 using this method and found an index of around 1.34 in the surface and between 1.40 and 1.41 in the center of the lens. The results showed a steeper GRIN in humans than in animal lenses with an almost constant index in the central two thirds of the lens. No changes were found with age. The authors noted that the comparison between experimental and theoretical ray tracing through extended GRIN in the equatorial plane was not satisfying for the human lenses measured, suggesting that the assumption of a coincident distribution in both equatorial and sagittal planes may not be valid for human lenses. This was later studied by the authors [Pierscionek, 1997] using a reflectometric fiber optic sensor as described in section 1.3.4. More recently Pierscionek et al. [2005] used the method to reconstruct the GRIN in the meridional plane of porcine lenses finding a parabolic distribution ranging from around 1.35 to 1.40 in the center.

Beliakov and Chan [1998] proposed the use of the trajectory of the rays inside the lens and not the deflections of the rays as input data. The method is complex, since the trajectories are seen through the lens with unknown GRIN. An iterative algorithm retrieved the real paths from the images so that they could be used to calculate the refractive index distribution. This method was never applied but in simulations.

Acosta et al. [2005] and Vazquez et al. [2006] presented a new algorithm that used as input data the ray deflection after (but not inside) the lens. This method allowed the reconstruction of mono or bi-polynomical GRIN profiles of spherical and non-spherical crystalline lenses. The algorithm involved experimental ray tracing across the lens at several angles (tomographic method) and was applied to porcine lenses. They related mathematically the angle of the rays deflected by the lens with the value of the eikonal and this last with the optical path. Since the gradient index of the lens was described with a polynomial function the optical path difference could be calculated analytically by summation of line integrals over the trajectory of the ray. The coefficients of the polynomial were obtained with a least squares fitting and the trajectory was approximated iteratively. Simulations with mono and bi-polynomial models (9 and 14 variables respectively) showed that with a Gaussian error added to the optical path (standard deviation equal to the wavelength used, $\lambda = 633$ nm) and projections up to 75° (500 rays per projection), the difference between nominal and retrieved GRIN was around 10^{-4} (in terms of root mean square) if the GRIN was described with one polynomial and 10^{-3} if a bi-polynomial distribution was used. Results of

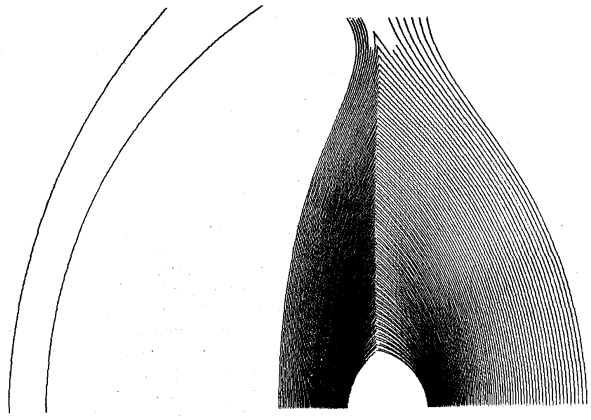

Figure 1.4: Model of the human eye proposed by Pomerantzeff. The change of the refractive index, thickness and curvature between layers followed a third polynomial function. (Reproduction from [Pomerantzeff et al., 1972]: Pomerantzeff et al. Journal of Modern Optics 1972)

the method on porcine lenses were 1.444 and 1.366 for nucleus and surface refractive index using a mono-polynomial model and 1.449 and 1.361 for nucleus and surface refractive index using a bi-polynomial model.

1.4.2 Optimization methods

Some authors studied the use of optimization methods to obtain the GRIN using as input data the external properties of the whole eye. Pomerantzeff et al. [1972] proposed the reconstruction of the GRIN distribution using focal length and spherical aberration of the eye. These authors built a shell model composed of a large number of layers where the radii of curvature, thicknesses and refractive index changed between layers following a third order polynomial function (figure 1.4). The constants of these polynomials were searched with a minimization algorithm. The high number of unknown variables made the optimization problem ill-defined as multiple solutions were possible.

Some studies have used Phakometry to study the GRIN distribution using much more simple models (only 1 variable). Garner and Smith [1997] and Garner et al. [1998] assumed a bi-elliptical model with a parabolic profile

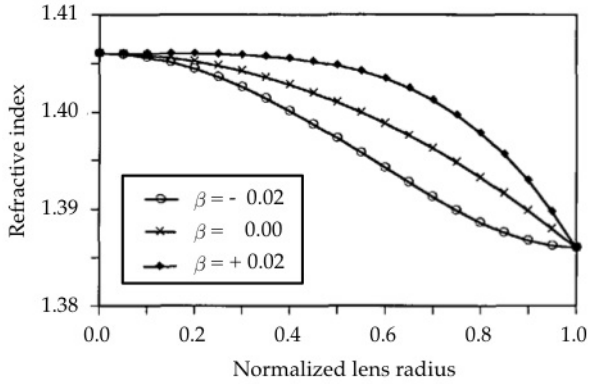

Figure 1.5: Model used by Hemenger et al. to study the change with age of the GRIN of the crystalline lens with a simple model (1 variable). The minimization algorithm used the position of the Purkinje image in posterior surface of the lens. (Reproduction from [Hemenger et al., 1995]: (Investigative Ophthalmology and Vision Science)

and fixed the nucleus refractive index at 1.406. Since the shape was fixed, the only variable was the surface refractive index. They found an increase of this variable with age from 1.386 at 22, to 1.394 at 54 year old group subjects. The study of the change of the GRIN with accommodation showed a constant surface refractive index with accommodation. Hemenger et al. [1995] used a similar approach assuming a nucleus refractive index of 1.406 and a surface refractive index of 1.386, and modeled the lens GRIN with a polynomial equation where the only variable β determined the decrease of the refractive index from nucleus to surface. Two age groups were studied: the younger group ranged in age from 19 to 31 and the older group from 49 to 61 years. The size of the fourth Purkinje image and the measurement of refractive error were used to find the value of β and results showed statistical differences between the age groups implying a steeper index gradient, on average, for the older group (figure 1.5).

With data from deflections of the rays passing through the lens, Axelrod et al. [1988] reconstructed the spherical GRIN of a fish lens using a simple model (parabolic GRIN profile with two variables). In a posterior work Garner et al. [2001] implemented a conjugate gradient method to reconstruct a more complicated (4 variables), although still spherical GRIN, and compared

the result with other techniques. Barbero et al. [2004], proposed the use of global search algorithms to reconstruct non-spherical GRIN using data of the direction cosine of the rays deflected by the lens.

Optical Coherence Tomography images of spherical fish lens were used by Verma et al. [2007] to reconstruct the in vivo GRIN distribution of an spherical fish lens. Since the fish crystalline lens is spherical, with a corrected OCT image the shape of the entire lens can be known. In addition, OCT provides the optical path difference (OPD) of each ray passing through the lens. Due to the symmetry of the problem, a local optimizer can find the best 4 variable GRIN that fits the OPDs recorded across the lens. In a previous work Ortiz et al. [2004] studied with simulations the possibility of estimating the GRIN from the intensity of the reflections in the layers of the crystalline lens in an OCT image.

In this thesis, optimization techniques applied to non-spherical GRIN lenses have been studied. If the shape of the lens is known, an optimization algorithm can search the set of variables that define a GRIN distribution that fits with the experimental measurements. First, we will compare the optimization using different possible experimental data (direction cosines of the rays deflected by the lens, impacts of the rays in a plane after the lens and optical path of the rays). Then results in porcine and human lenses are presented using Optical Coherence Tomography to extract data of the optical path of the rays through the lens.

1.4.3 Magnetic resonance imaging

Moffat and Pope [2002b] proposed to use the correlation between the transverse spin-spin relaxation time, measured in Magnetic resonance imaging (MRI) and the refractive index. Since the refractive index is linearly related to the concentration of protein [Pierscionek et al., 1987], and the relaxation time measured in MRI can be also related linearly with protein concentration, the technique was used to extract two-dimensional maps of the gradient refractive index of the crystalline lens. The nucleus refractive index was also found to statistically significantly change linearly with age

In an earlier study [Moffat and Pope, 2002a], 18 human lenses between 14 and 82 years old were measured. The results showed slight differences in the refractive index distribution in equatorial and axial direction and between anterior and posterior halves of the lens. The surface refractive index was found to be constant with age (between 1.35 and 1.37) and the

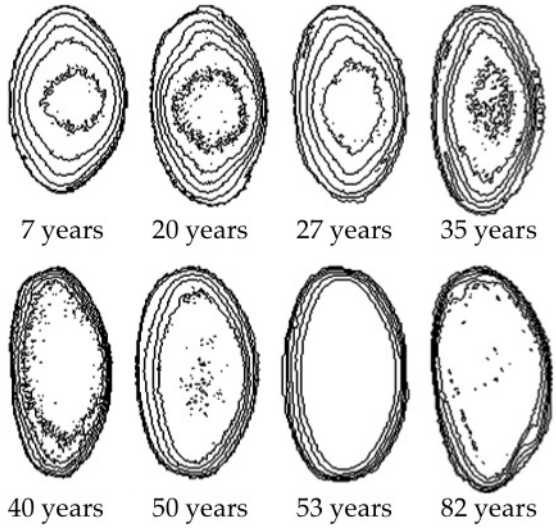

Figure 1.6: Gradient index distribution of in vitro human crystalline lenses of different ages extracted using Magnetic Resonance Imaging. (Reproduced from [Jones et al., 2005] (Vision Research).

nucleus refractive index was found to change statistically significantly with age linearly (from 1.44 to 1.41 at 15 and 80 year old lenses respectively). A later study [Jones et al., 2005], with 20 lenses, found also a clear flattening of the refractive index with increasing age, but nucleus and surface refractive index were noisy and the trends were not statistically significant.

The careful calibrations required by the technique have been contested in the literature [Pope et al., 2008]. Age related changes have been studied with this technique [Moffat et al., 2002a; Jones et al., 2005; Augusteyn et al., 2008] and some values have been reported even in vivo [Kasthurirangan et al., 2008].

1.4.4 X-ray phase contrast tomography

An X-ray Talbot interferometer was used to measure the gradient refractive index of the crystalline lens of a murine lens [Hoshino et al., 2010] and other animal models such as porcine lenses [Hoshino et al., 2011]. The system was used to estimate the protein density of the sample and allowed the

measurement of the whole in vitro eye, as it has the ability to tolerate large density differences.

The measurement time is near 30 minutes, since between 600 and 900 projections must be adquired rotating the sample for X-ray phase tomography. The phase shift was calibrated using solutions of known density and the relation was found to be linear in the range of concentration tested. A second linear relationship was used to relate the protein concentration and the refractive index. The gradient refractive index of the porcine lens measured ranged from 1.45 in the center of the lens to 1.35 in the periphery and was well fitted with second order polynomial functions although the authors reported some fluctuations in the GRIN profile that may be linked to growth process.

1.5 Imaging the crystalline lens: optical distortion correction

The study of the crystalline lens in vivo requires consideration of the distortion produced by the refracting surfaces of the eye. The anterior surface shape of the lens is distorted by the refraction of the rays at the cornea, and the posterior surface shape by the refraction at the cornea and at the lens itself. This effect is inherent to optical techniques aiming at direct imaging of the crystalline lens (i.e. Scheimpflug camera or Optical Coherence Tomography) or at the indirect estimation of the crystalline lens radii of curvature (i.e. Purkinje imaging).

Purkinje imaging has been extensively used for phakometry of the lens in vivo, as well as to measure tilt and decentration of crystalline and intraocular lenses. Typically, the algorithms used to estimate the radii of curvature from the magnification of a projected light source on the anterior segment of the eye consider the refraction at the anterior cornea, and iteratively that of the anterior lens. Some studies have actually used Purkinje images to explore the influence of GRIN on the changes of the crystalline lens optics with aging [Hemenger et al., 1990; Garner et al., 1998] or accommodation [Garner and Smith, 1997]. However, most algorithms used to estimate the posterior lens radius of curvature from Purkinje imaging [Smith and Garner, 1996; Garner, 1997], consider a homogeneous refractive index in the lens, typically the equivalent refractive index.

The first Scheimpflug imaging system used for studying the crystalline

lens was developed by Brown [1973b]. In this study, the correction of the geometrical distortion is mentioned, but the results seem to indicate that the optical distortion was not fully corrected. Cook and Koretz [1998] corrected the optical distortion with a method based on a Hough transform. Dubbelman and van der Heijde [2001] developed correction algorithms based on ray tracing through the refracting surfaces, and validated the measurements in Topcon SL-45 (Topcon Medical Systems Inc, Oakland, USA) and Nidek EAS-1000 (NIDEK Co. Ltd., Gamagori, Japan) systems. Rosales and Marcos [2009] applied a similar algorithm to correct the raw images provided by Pentacam (OCULUS Optikgeräte GmbH, Wetzlar, Germany). It was reported [Dubbelman and van der Heijde, 2001] that the study of the uncorrected images would produce an over estimation of the anterior and posterior radii of curvature and a decrease in the thickness of the lens. An increasing anterior chamber depth would increase the error in the measurement. In all cases, the proposed optical distoriton correction algorithms assume a homogeneous refractive index in the lens.

Optical Coherence Tomography images show the optical path of each ray (A-scan), i.e., the distance traveled by the ray multiplied by the refractive index of the media. In addition to the distortion due to the media refractive index, a non linear scan geometry can distort the image too. The easiest method to reconstruct the shape and position of the surfaces involves simply a division of the recorded optical paths by the value of refractive index of the media [Wang et al., 2002; Kim et al., 2009, 2011]. This method does not take into account the refraction of the rays at the optical surfaces. To correct the refraction distortion present in the images of the anterior chamber, an algorithm based on Fermat's principle [Westphal et al., 2002], and others using Snell's law [Podoleanu et al., 2004; Ortiz et al., 2010] have been proposed. Ortiz et al. [2010] studied the simplest correction (division by the refractive index neglecting the refraction at the surfaces) and reported an overestimation of the radius of curvature of anterior and posterior surface of the lens used in the study by 8.9 and 59.7% respectively. He proposed the use of 3-D Delaunay decomposition to refract the rays and corrected the distortion due to the non linear scan geometry, and achieved relative errors in the measurements of the radii of curvatures below 1% (with respect to non-contact profilometry). The correction algorithms are used to extract information of the crystalline lens but a homogeneous index must be assumed to trace the rays through the lens and reconstruct its posterior surface. To accurately estimate the posterior lens surface, the algorithms should incorporate the

inhomogeneous nature of the refractive index.

1.6 Open questions on the gradient refractive index

Refractive index values. There is not yet a clear consensus on the value of the refractive index of nucleus and surface of the crystalline lens. The values reported in the few studies of the literature (typically with a relatively low number of human crystalline lens samples), are very scattered. Whether this variability is associated with the error of the techniques or represents real dispersion in the population is still under question.

Refractive index profile. It is clear that the refractive index peaks at approximately the center of the lens. However, there is no consensus on the GRIN model best representing the refractive index distribution. The identification of the most suitable model has been somewhat tampered by the lack of experimental data.

Change of GRIN shape with age. Although Magnetic Resonance Imaging suggests that the crystalline lens index of refraction varies smoothly from the center to the surface in the young eye, and a central plateau is formed with aging Jones et al. [2005], there is still no consensus how the gradient index is displaced towards the surface. The limitations of the techniques, and the relatively high noise in the data available have created controversy on this question.

Optics of the crystalline lens: power and spherical aberration. The exact contribution of the gradient refractive index to the power of the crystalline lens remains unknown. In vitro studies [Borja et al., 2008] show that a lens with the same shape and a homogeneous index equal to the surface has around 40% of the total power of the crystalline lens. However, a similar analysis for the spherical aberration does not exist. Except for fish lenses (which exhibit an almost zero spherical aberration) little is known on the relative contribution of the surface shape and GRIN to the spherical aberration of mammal lenses.

GRIN contribution to accommodation. The change of the refractive index distribution when the lens accommodates is not clear. A change in the equivalent refractive index should be associated with a change in the contribution of the GRIN to the change of power. However, although some theoretical studies support this change [Garner and Smith, 1997], and the first reports of GRIN [Kasthurirangan et al., 2008] and its effects [Maceo et al., 2011] at

different levels of accommodation have been recently presented, the answer to the question is still debated. The study of the changes of GRIN with accommodation is beyond the scope of this thesis. Current developments in the laboratory using methodology developed in this thesis address that goal.

Presbyopia. The change in elasticity of the crystalline lens with aging leads to presbyopia. This change of elasticity likely encompass a change in the GRIN distribution. However, the relation has not yet been explored in detail. Interestingly, the elasticity of the lens, as measured recently with Brillouin scattering microscopy [Reiß et al., 2011; Scarcelli and Yun, 2012], and its changes with age, shows a very similar profile to that reported for the GRIN in this thesis.

Cataract surgery: intra-ocular lenses modeling. The opaque crystalline lens is replaced by an intraocular lens in a cataract procedure. There have been proposals in scientific studies [Siedlecki et al., 2004; Beadie et al., 2008] and patents [Hamblen, 1992; Roffman et al., 2004; Baer et al., 2006] of monofocal intraocular lens designs with a gradient structure. The first attempts for restoration of accommodation thought accommodative intraocular lenses (A-IOL) are still rather crude (the only FDA approved design is expected to change the power of the eye by moving axially). However, if GRIN plays a role in the accommodative-related power changes in the eye, one could envision sophisticated A-IOLs with GRIN properties.

1.7 Goals of this thesis

This thesis addresses the development of a new method for the reconstruction of the GRIN distribution of the crystalline lens, demonstration on the porcine lens, measurements on human crystalline lenses, and implications for quantitative imaging of the crystalline lens. The specific goals of the thesis are:

- To develop new optimization methods for the reconstruction of the GRIN of the crystalline lens, overcoming drawbacks of the previous methods: to use an anatomical model with sufficient variables to express the possible different distributions of GRIN, to calibrate the method, and to use a global search algorithms to avoid the solution to fall in a local minimum in the optimization process.

- To explore the advantages of the newly proposed technique, as well as the expected performance of the method on simulations, considering real error estimates.

- To measure the GRIN distribution of the lens three dimensionally in vitro.

- To explore the relative contribution of the surface shape and GRIN distribution on astigmatism and spherical aberration of the crystalline lens.

- To measure the possible change of the GRIN profile with age in human lenses.

- To quantify the effect of GRIN on the visualization and shape measurements of the posterior lens surface from OCT measurements.

- To develop optical distortion correction methods in OCT imaging to improve the quantitative measurements of posterior lens shape.

1.8 Hypothesis

- It is possible, through the use of novel optimization methods, to reconstruct the gradient refractive index (GRIN) of the crystalline lens (porcine and human), using data of the optical path accumulated by the rays when passing trough the lens, or ray tracing data as the cosines of the deflected rays or the impacts in a posterior plane. We will test the proposed method and the accuracy of the reconstruction using computer simulations with experimental estimates of the input data error.

- The GRIN plays a significant role in the optical properties of the lens. We will test this hypothesis by measurements in a porcine lens, and estimations of the lens aberrations with a homogeneous index and the reconstructed GRIN.

- The human GRIN profile changes with age. We will test this hypothesis with measurements of the GRIN distribution in human lenses of different ages.

- The correction of the images of the anterior segment of the eye acquired with Optical Coherence Tomography (OCT) will benefit from the consideration of the GRIN of the crystalline lens. The effect of the GRIN on the reconstruction of the posterior lens shape will be tested on lenses in vitro (i.e. with accessible posterior lens shape). Optical distortion correction algorithms through the GRIN structure will be developed.

1.9 Structure of this thesis

The thesis has been organized by chapters which roughly correspond to the articles published on the topic of the thesis. The current introductory chapter presents an extensive background, state of the art, and motivation of the thesis. The methods implemented in the thesis are also compiled and presented in detail in a single chapter (Chapter 2).

Chapter 2 presents the developed method for GRIN reconstruction, which uses ray tracing or optical coherence tomography data as input data, as well as the experimental systems used to obtain experimental data from crystalline lenses.

Chapter 3 presents the accuracy of the technique though computational simulations of the different experimental approaches using experimental estimates of data input errors.

Chapter 4 presents the reconstruction of the gradient refractive index of a porcine crystalline lens three dimensionally using data obtained from a spectral OCT system in our laboratory. The relative contribution of the surface shape and GRIN on astigmatism and spherical aberration of these lenses is presented.

Chapter 5 presents the reconstruction of the GRIN profile (in two dimensions) in a set of lenses of various ages. The variation of the values of surface and nucleus refractive indices, and in particular the shape of the GRIN profile, are discussed.

Chapter 6 explores the optical distortion produced by the GRIN on the posterior surface shape of a young crystalline lens imaged by OCT. The impact of the assumption of a simple correction method on the geometrical parameters of the crystalline lens are discussed.

Chapter 7 proposes a new optical distortion correction method considering the presence of GRIN in OCT images of the crystalline lens, which is applied on a set of human lenses in vitro.

Chapter 2

Methods

This chapter describes the algorithms developed to trace rays through homogeneous and gradient index (GRIN) media, the global and local search algorithms and the Laser Ray Tracing and the Optical Coherence Tomography systems used in the thesis.

The ray tracing algorithm is used to simulate the experimental measured data for a certain GRIN distribution. The algorithm was implemented in MatLab and was validated comparing the results with a well-known commercial software. The global search algorithm is used to search the best GRIN (i.e. the best parameters defining the GRIN distribution) that fits the measured data. It was implemented and designed in MatLab using the Genetic Algorithm Toolbox as a model. The Laser Ray Tracing and Optical Coherence Tomography system were used in a first step to calibrate the method and estimate the expected experimental error (chapter 3) and later to image porcine and human lenses (chapters 4 and 5).

The author of this thesis implemented and tested the algorithms and designed and constructed the experimental Ray Tracing System in collaboration with Sergio Barbero, Sergio Ortiz, Susana Marcos and the rest of the members of the Visual Optics and Biophotonics Laboratory.

2.1 Introduction

In this chapter we will describe the algorithms and experimental set-ups implemented to evaluate the potential for optical measurements of the lens gradient index (GRIN) with optimization methods. The goal of these methods is the measurement of physical properties of the lens and the reconstruction of the GRIN distribution that best matches the experimental data. The methods involved the development of: (*1*) algorithm to simulate the experimental measurements, (*2*) a search method to find the optimal GRIN and (*3*) experimental set-ups to obtain the input data to the algorithms.

The algorithm to simulate the experimental data from the crystalline lens consists of a ray tracing program through both homogeneous and GRIN refractive index media. Systems with axial symmetry and conical surfaces, this is centered crystalline lenses, were considered. Ray tracing through homogeneous media was solved by finding the intersections between rectilinear rays and surfaces, and applying Snell's law in the intersections, this was programmed in MatLab (MathWorks, Natic, MA) using the formulas derived by Stavroudis [1972]. To trace rays through graded-index media, the ray equation has to be solved. Although an analytical solution can be found in some situations, generally the ray equation requires a numerical solution. Some methods have been developed for ray tracing though a GRIN media [Hewak and Lit, 1985]. However Sharma et al. [1982] algorithm appears to be the most widespread in the field. For the purposes of this thesis, the Sharma algorithm was implemented, and the Stone and Forbes [1990] algorithm was used to find the intersection between rays inside the GRIN and surfaces.

An optimization algorithm was developed to search the GRIN distribution that matches the measurement. This algorithm involved the definition of a merit function to calculate the separation between the results of a model with a certain GRIN and the experimental data and a minimization algorithm. From the different possible optimization techniques that could have been used, we opted for a genetic algorithm [Holland, 1975] which does not need differentiation of the merit function and avoid solutions stuck in local minima. These algorithms are increasingly being used in different areas including optical design [Vasiljević, 2002].

Several experimental techniques to measure physical properties of the crystalline lens were used in this thesis and are described in the last section of this chapter. These include custom-instruments for 2-D time domain

Optical Coherence Tomography (OCT), 3-D spectral domain OCT and Laser Ray Tracing. OCT systems were used to image the lens and to extract the optical path difference between anterior and posterior surface. The Laser Ray Tracing system was built to measure the deflection of the rays when passing through the lens and to estimate the position of the rays in a plane after the lens. Those values represent potential input data that could be used as input data in an optimization algorithm to calculate the GRIN that best fits the measurements.

2.2 Ray tracing algorithm

2.2.1 Homogeneous refractive index media

For ray tracing through homogeneous media two simple operations are involved: transfer and refraction. While the first one finds the point of intersection of a ray with a surface, the seconds implements Snell's law to calculate the refraction in the inter-phase.

Transfer

A ray is defined with a point $\mathbf{W}$ and a direction vector $\mathbf{N}$, therefore the equation of any point $\mathbf{W}_\lambda$ on the ray is given by $\mathbf{W}_\lambda = \mathbf{W} + \lambda\mathbf{N}$.

For convenience, the equation for any refracting surface is given with reference to a coordinate system in which the z axis coincides with the axis of the optical system. The x and y axes lie on a plane perpendicular to the z axis, and are tangent to the refracting surface at the point where the axis and the surface intersect, i.e. the apex. Then, if t is the distance between the system origin where $\mathbf{W}$ is defined and the surface apex, and we define the unit vector in the direction of the axis of the optical system $\mathbf{A} = (0, 0, 1)$, the vectorial equation of the ray can be expressed by:

$$\mathbf{W}_\lambda = \mathbf{W} - t\mathbf{A} + \lambda\mathbf{N}. \tag{2.1}$$

As mentioned above, we considered a rotationally symmetric optical system where the refracting surfaces are surfaces of revolution, and the shape of the surfaces is going to be expressed by conics. The equation of a centered conic of revolution can be written as

$$\phi = ckz^2 + c(x^2 + y^2) - 2z = 0$$
$$\phi = c\bar{\mathbf{R}}^2 - c(1-k^2)(\bar{\mathbf{R}}\cdot\mathbf{A})^2 - 2(\bar{\mathbf{R}}\cdot\mathbf{A}) = 0 \tag{2.2}$$

where $\mathbf{A}$ is the unit vector in the direction of the z axis and $\bar{\mathbf{R}}$ is a point of the conic surface. The intersecion point between the ray defined by 2.1 and the conic defined by 2.2, $\bar{\mathbf{R}}$, can be calculated by substitution and the normal to the surface at that point, $\bar{\mathbf{N}}$, that will be used to apply Snell's law later, can be calculated with the operator nabbla. The formulas derived by Stavroudis [1972] to calculate the point of intersection and normal to the surface are:

$$\begin{aligned}\bar{\mathbf{R}} =& \mathbf{W} - t\mathbf{A} + \bar{\lambda}\mathbf{N},\\ \bar{\mathbf{N}} =& \frac{-c\bar{\mathbf{R}} + \mathbf{A} + c(1-k)(\mathbf{A}\cdot\bar{\mathbf{R}})\mathbf{A}}{[1 - c^2(1-k)(\bar{\mathbf{R}}\cdot\mathbf{A})^2]^{1/2}},\end{aligned} \tag{2.3}$$

where

$$\begin{aligned}\bar{\lambda} =& (1/V)c(\mathbf{W} - t\mathbf{A})^2 - 2\mathbf{A}\cdot(\mathbf{W} - t\mathbf{A}) - c(1-k)[\mathbf{A}\cdot(\mathbf{W} - r\mathbf{A}]^2,\\ V =& (\mathbf{A}\cdot\mathbf{N})(1+ct) - c(\mathbf{N}\cdot\mathbf{W}) + R + c(1-k)[\mathbf{A}\cdot(\mathbf{W} - t\mathbf{A})(\mathbf{A}\cdot\mathbf{N}),\\ R^2 =& [1 - (1-k)(\mathbf{N}\cdot\mathbf{A})^2]1 - [\mathbf{A}\times\mathbf{N}(1+ct) + c(\mathbf{N}\times\mathbf{W}]^2\\ &+(1-k)1 - \mathbf{A}\times\mathbf{N}\cdot[(\mathbf{A}\times\mathbf{N})(1+ct) + c(\mathbf{N}\times\mathbf{W})]^2.\end{aligned}$$

Refraction

The inputs to apply refraction function (Snell's law) are: (*1*) the direction of the normal to the surface; (*2*) the refractive index before and after the refractive surface and (*3*) the direction of the incident ray. The vectorial form of Snell's law can be expressed as:

$$\mathbf{N}^*\times\bar{\mathbf{N}} = \mu(\mathbf{N}\times\bar{\mathbf{N}}), \tag{2.4}$$

where $\mathbf{N}^*$ is the direction vector of the refracted ray, $\bar{\mathbf{N}}$ is the direction vector for the incident ray, $\mathbf{N}$ is the normal to the refracting surface and μ the ratio between refractive indices on opposite sides of the refracting surface (if n is the index of refraction on the incident-ray side of the refracting surface and n^* is the index on the refracted-ray side, then $\mu = n/n^*$.

The refracted ray direction vector can be calculated as:

$$\mathbf{N}^* = \mu\mathbf{N} + \gamma\bar{\mathbf{N}},$$
$$\text{where} \quad \gamma = -\mu(\mathbf{N}\cdot\bar{\mathbf{N}}) + \sqrt{1-\mu^2[1-(\mathbf{N}\cdot\bar{\mathbf{N}})^2]}. \tag{2.5}$$

2.2.2 Gradient refractive index media

As in a homogeneous media, the ray tracing algorithm in an inhomogeneous medium involves two steps: (*1*) ray tracing through the GRIN medium and (*2*) calculation of the intersection of the ray with the surface (in our case, the posterior surface of the crystalline lens) limiting the GRIN medium.

Sharma's algorithm

The Sharma et al. [1982] method to trace rays through gradient index media essentially transforms the ray equation

$$\frac{d}{ds}\left[n(\mathbf{r})\frac{d\mathbf{r}}{ds}\right] = \nabla n(\mathbf{r}), \tag{2.6}$$

into a convenient form, and uses Runge-Kutta method to solve numerically the resulting differential equation. If the following vectors are defined

$$\mathbf{R} = (x, y, z),$$
$$\mathbf{T} = \frac{d\mathbf{R}}{dt} = (n\frac{dx}{ds}, n\frac{dy}{ds}, n\frac{dz}{ds}) = (n\alpha, n\beta, n\gamma)$$
$$\mathbf{D} = n(\frac{\partial n}{\partial x}, \frac{\partial n}{\partial y}, \frac{\partial n}{\partial z})$$

where α, β and γ are the components of the unitary vector that define the direction of the ray, this is, the direction cosines of the ray, the equation 2.6 can be expressed in the following way.

$$\frac{d^2\mathbf{R}}{dt^2} = D(\mathbf{R}) \tag{2.7}$$

The equation 2.7 has to be resolved with the initial conditions $R = R_0$ and $T = T_0$. The next points of the solution will be generated by the Runge-Kutta

method:

$$\begin{aligned}\mathbf{R_{n+1}} &= \mathbf{R_n} + \Delta t\,[\mathbf{T_n} + (\mathbf{A} + 2\mathbf{B})/6]\,,\\ \mathbf{T_{n+1}} &= \mathbf{T_n} + (\mathbf{A} + 4\mathbf{B} + \mathbf{C})/6,\end{aligned} \tag{2.8}$$

where the vectors A, B and C are defined as:

$$\begin{aligned}\mathbf{A} &= \Delta t\, D(\mathbf{R_n}),\\ \mathbf{B} &= \Delta t\, D\left(\mathbf{R_n} + \frac{\Delta t}{2}\mathbf{T_n} + \frac{1}{8}\Delta t\mathbf{A}\right),\\ \mathbf{C} &= \Delta t\, D\,(\mathbf{R_n} + \Delta t\mathbf{T_n} + 1/2\Delta t\mathbf{B})\,,\end{aligned} \tag{2.9}$$

and Δt is the extrapolation distance, also known as Sharma's step. The value of Δt sets the desired accuracy, i.e. the smaller the value, the better the accuracy but also greater computation time.

Stone and Forbes' algorithm

The truncation error in position and direction for a single iteration of the Sharma's method is, in general, proportional to Δt^5. Since the number of steps needed is inversely proportional to Δt, the global error of the algorithm is proportional to Δt^4. This is the error at the Runge-Kutta points, but in certain cases, the trajectory is needed between those points, as it occurs for finding the point of intersection of a ray with a given surface. The Runge-Kutta method does not provide a method to find the trajectory that connects the Runge-Kutta points, and therefore one must be constructed. Sharma and Ghatak [1986] proposed the parametrization of the ray equation within an accuracy of Δt^4 using a third order polynomial. The coefficients of this polynomial can be calculated with the ray positions and ray slopes at Runge-Kutta points using Hermite interpolation. Stone and Forbes [1990] showed that using this method, the error introduced in the location of the ray-surface intersection could dominate the error accumulated in transferring across the inhomogeneous region.

The method that Stone and Forbes [1990] proposed aims at finding an optimal step size t_{int} to transfer from the last Runge-Kutta point to the surface, by applying the numerical ray equation with the a term dependent on t^4 to the ray equation:

$$\mathbf{R_{n+1}} = \mathbf{R_n} + t\mathbf{T_n} + \frac{1}{2}t^2\frac{\mathbf{A}}{\Delta t} + \frac{1}{6}t^3\frac{4\mathbf{B} - \mathbf{C} - 3\mathbf{A}}{\Delta t^2} + \frac{1}{24}t^4\frac{4(\mathbf{A} - 2\mathbf{B} + \mathbf{C})}{\Delta t^3} \tag{2.10}$$

The surface after the inhomogeneous media should be described with an implicit formula, $F(x, y, z) = 0$, and the value of t_{int} that ensures that $\mathbf{R_{n+1}}(t_{int})$ belong to the surface is found evaluating F and dF at the Runge-Kutta points previous to the surface. This method has been shown to use approximately the same amount of computation time as the one proposed by Sharma and Ghatak. One advantage of this method is that it does not require the evaluation of the gradient index in the point out of the inhomogeneous region, unlike Sharma and Ghatak's.

Optical path

The computation of optical path length (OPL) in homogeneous media is straightforward, since it can be calculated as the multiplication of the geometric length of the path through the media by the index of refraction. However, if the refractive index varies through the path of the ray, the OPL must be calculated with the integral:

$$\mathrm{OPL} = \int n(s)ds \tag{2.11}$$

The path of the rays between the anterior and the posterior surface of the crystalline lens can be calculated using Sharma et al.'s and Stone and Forbes' algorithms but, as mentioned above, the Runge-Kutta method to solve the ray equation does not provide the trajectory between the Runge-Kutta points.

The simplest approach would be to assume linear trajectories between the Runge-Kutta points. However we approximated the path of the ray in each interval with the third order polynomial defined by the Runge-Kutta points and the director vector at those points, i.e. the Hermite polynomial. Regardless of the path selected for the ray between the Runge-Kutta points, in this thesis, we calculated the integral using Newton-Cotes formulas evaluating the GRIN in eleven points along the trajectory [Ueberhuber, 1997].

2.2.3 Validation of the ray tracing algorithm

To validate the implemented ray tracing method, we have compared the results of the algorithm written in MatLab with those from a well known commercial ray tracing program (ZEMAX, Zemax Development Corporation, Bellevue, Washington). Ray tracing through homogeneous and inhomogeneous lenses was studied. For this purpose we used the 20S GRIN model by

Goncharov and Dainty [2007], described by a polynomial equation in axial and meridional direction:

$$n(z,r) = n_0 + n_1 r^2 + n_2 r^4 + n_3 z + n_4 z^2 + n_5 z^3 + n_6 z^4 \tag{2.12}$$

This GRIN model can be easily implemented in ZEMAX with a built-in surface type (Gradient 5). The same lens shape with an homogeneous index was used to validate the ray tracing through homogeneous media.

Forty rays parallel to the optical axis in a 6-mm pupil were traced with both routines. Five types of ray tracing data were studied: (*1*) direction cosines of the rays deflected by the lens, (*2*) heights of the point where the ray impacts posterior surface of the lens, (*3*) impacts in a plane perpendicular to the optical axis after the lens, and (*4*) optical path differences accumulated up to the posterior surface of the lens and up to the plane where impacts were calculated.

Differences between algorithms for homogeneous lenses were machine precision. For ray tracing in a GRIN medium, the differences depended on the Sharma's algorithm step. For a 10 μm step, the differences were below 10^{-4} μm for ray intersections and optical path calculated at the posterior surface of the lens and at a plane after the lens, and below 10^{-13} for cosine of the rays deflected by the lens. These differences are probably due to differences in the ray tracing algorithm (although a more detailed comparison is not possible, as the ZEMAX algorithms are proprietary).

2.2.4 Effect of Sharma's step size

The step size sets the trade-off between the precision in the computation of the ray trajectories inside the GRIN and the computation time. Figure 2.1 shows the differences in the estimation of the ray tracing data for different step sizes compared to a smaller one (10^{-4} μm). We found that a 10 μm step size was a good trade-off, as the estimated errors were less than 10^{-9} μm for intersection, 10^{-14} for cosine of the deflected ray, and less than 10^{-6} μm for OPD, with a computation time of less than 0.2 seconds on an Intel Xeon process at 3 GHz.

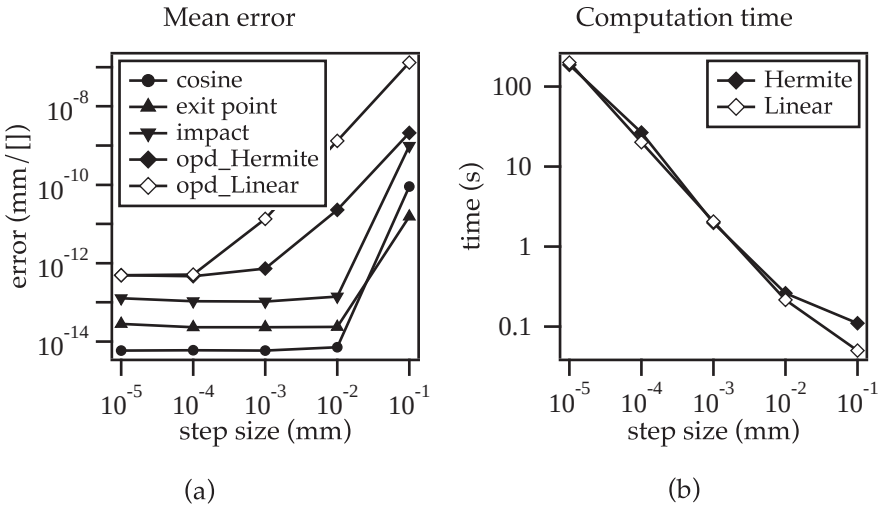

Figure 2.1: (a) Estimated error in simulated data (lateral deviations, impacts of OPD) as a function of the step size in the Sharma algorithm. (b) Computational time to ray trace and estimate the OPD as a function of the step size. The OPD was calculated either using straight segments or a Hermite polynomial interpolation between the Runge-Kutta points. Simulations were performed with Goncharov crystalline lens model 20S. (Reproduced from de Castro et al. [2011a], Optics Express).

2.3 Optimization algorithm

In optical system design, the goal of optimization is to find a system that fulfills some quality criteria with, usually, some boundary conditions [Vasiljević, 2002]. The reconstruction of the GRIN structure is based on an optimization method where the variables to optimize are the parameters that define the lens GRIN distribution. A merit function (MF) was constructed to quantify the agreement between the experimental data and the simulated data for a given set of parameters. The MF was defined as the root mean square (RMS) of this difference. An optimization algorithm is needed to minimize this MF.

We implemented two sequential optimization algorithms. First, a global search algorithm was used to find the global minimum area and avoid local minimum trapping. Second, starting from the best solution found by the

global search algorithm, a local search algorithm was used to descend to the minimum.

2.3.1 Genetic optimization

The genetic algorithm (GA) is an optimization and search technique based on the principles of genetics and natural selection. A population composed of many individuals evolve under certain selection rules to a state that minimizes the MF. The method was developed by Holland [1975]. Some of the advantages of GA are:

1. Optimizes with continuous or discrete variables,
2. does not require derivative information,
3. simultaneously searches a wide sample of solutions,
4. deals with a large number of variables,
5. optimizes merit functions with complex surfaces (the GA can jump out of a local minimum).

Although in some cases GA have produced satisfactory results where traditional optimization approaches had failed, GA are not adapted to solve every problem. Traditional methods have been adjusted to find rapidly the solution of a well-behaved convex analytical function of only a few variables. On the other hand, the large population of potential solutions used by the GA are a powerful tool, but generally, the computation time required to reach a solution is much higher than in conventional algorithms.

The algorithm starts with a population of solutions (generation) randomly selected within the expected range of solutions. The following generations are created combining Darwinian survival-of-the-best philosophy with a random but structured information exchange among the population. Each solution (individual) is determined by its variables (chromosomes) and the merit function of the problem evaluate whether each individual is adapted to the problem or not.

Since GA is a search technique, it must be limited to exploring a reasonable region of the variable space. Sometimes this is not necessary because the algorithm converges rapidly from the initial population, but in certain situations constrains must be set, particularly with noisy data. There are different alternatives to add constrains [Vasiljević, 2002]. For the purposes of this thesis we have added penalty terms to the MF if the constrains were violated.

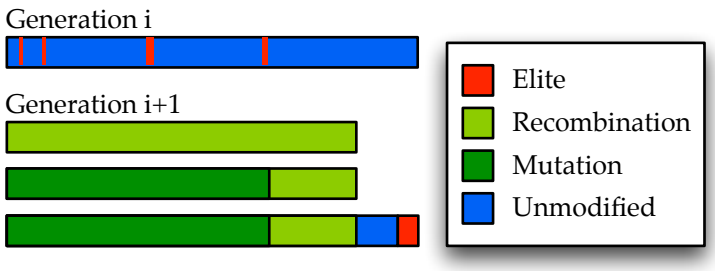

Figure 2.2: Schematic diagram of a genetic algorithm iteration. A percentage (85%) of the population is created by crossover and mutation. Some of the solutions (5%) are directly copied to the next generations (elite) and the rest of the population is randomly selected from previous generation.

A schematic diagram of the rules of the algorithm is shown in figure 2.2 and involves three basic steps: selection, crossover and mutation.

Selection

The selection of the individuals with which the next generation will be created can be done in many different ways. We implemented a roulette selection that essentially sorts the individuals of the generation as a function of their score and designs an expectation to be chosen for each one of them. This expectation is calculated with a function that can be constant (i.e. all the individuals have the same possibility to be chosen) or decreasing as a function of its score (MF value) or its range in the population. In our case the algorithm calculates the expectation following a decreasing function, $1/x^2$, which assigns the most fitted individuals higher probability to be chosen than the rest of the population.

Once the expectation is calculated, a roulette is created with all the individuals. In the roulette, the individuals with higher expectation take up more room than the ones with lower expectation. The roulette is spanned to select two individuals, and generate from those one individual of the next population with crossover.

Other selection rules are possible. To ensure the selection of the best individuals, a percentage of the solutions can be automatically selected and

copied to the next generation. In our implementation, a 5% of the population is selected as elite. These individuals are the ones with the best score and, not only are copied to the next generation, but also participate in the selection process as the rest do.

Crossover

In the selection process, two parents are chosen, the offspring will be a combination of these two parents. Many different approaches have been proposed. In our case the variables of the child will be selected randomly between those of the parents that contribute. This method is called uniform crossover. One child is created from each couple. As can be seen in figure 2.2, 80% of the population is created with this method.

Mutation

To explore the entire solution space, mutation is added to the solutions. This avoids partly the problem of overly fast convergence. There are many methods to add mutation and many possibilities to chose the individuals that will be mutated. In our implementation we chose to mutate some of the children created with the crossover function, and the mutation was simulated with Gaussian noise added to all the variables. The amount of mutated children was kept constant during all the calculations, 60%, as is illustrated in figure 2.2. The amplitude of mutation (amount of noise added to each solution) was decreased in subsequent generations to allow the algorithm to focus on smaller areas each generation.

The implementation of a Genetic Algorithm can be highly diverse. Selection can be done in different ways, for example considering not only the position in the ranking of solution,but also its merit function value. In our particular implementation, crossover was achieved by mixing the variables of the solutions, but another possibility is to create the children closer to the parent with best MF. Mutation adds random noise to the variables but, the algorithm could vary not all the variables but only some of them, even the amplitude of the mutation could be related with the MF value. The scheme of the GA could be varied too: part of the next generation could be created by mutating only the elite, crossover could be done mixing individuals with low and high MF values to try to use more extensively the elite; in some implementations, a generation can benefit from the distribution of solutions

of a previous generation, and some solutions could migrate. For this work, a simple GA allowed convergence, and the parameters (crossover, mutation ratio and amplitude of mutation, etc...) were adapted to the problem. Other variations could be studied to improve the performance and speed of convergence of the algorithm.

2.3.2 Hybridation with local search algorithms

A hybrid GA combines the power of the GA with the speed of a local optimizer. GAs are fast at showing the direction of the global minimum, but a local search algorithm is faster to descend to the minimum. Hybrid GAs can be implemented in different ways. For example, the local optimizer can be started after the GA, it can seed the GA population with local minima found starting the local search algorithm at random points in the population, or it can be applied every certain number of generations starting from the best solution found by the GA.

We implemented the first option and used a Simplex [Nelder and Mead, 1965] algorithm to descend to the expected global minimum. The algorithm starts from a simplex (a set of n + 1 points if n is the number of variables) and modify this simplex to find the minimum. Although the default implementation of the algorithm in MatLab calculates the starting simplex increasing each one of the variables of the starting point by 5%, we have used a smaller simplex to avoid loosing the local minimum. Each iteration of the simplex is composed of the following steps.

1. **Sort**. The n + 1 solutions are ordered to satisfy $f(x_1) \leq f(x_2) \leq \ldots f(x_{n+1})$

2. Calculate the center of gravity, $\bar{x}$ of all the points except x_{n+1},

3. **Reflect**. The point x_{n+1} is reflected with respect to the center calculated before: $x_r = \bar{x} + \rho(\bar{x} - x_{n+1})$,

4. **Expand**. If the function in the reflected point is lower than $f(x_1)$ the expansion point is calculated: $x_e = \bar{x} + \chi(x_r - \bar{x})$ to try to improve the reflected point. If there is not improvement, i.e. $f(x_e) \geq f(x_r)$, the expansion point is discarded and a contraction (see step 5) is performed. If the value of the function in x_e is lower, the point replace x_{n+1} in the simplex and the iteration is finished.

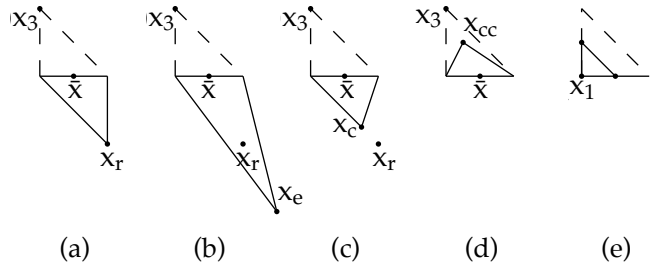

Figure 2.3: Nelder-Mead simplex possible steps: (a) reflection, (b) expansion, (c) outside contraction, (d) inside constraction and (e) shrink. (Reproducted from Lagarias et al. [1998], SIAM Journal on Optimization).

5. **Contract**. If the value of the function in the reflected point is higher than the rest of the points of the simplex, then a contraction is performed between $\bar{x}$ and the best of x_{n+1} and x_r.

   - **Outside**. If $f(x_n) \leq f(x_r) < f(x_{n+1})$ the contracted point is calculated as $x_c = \bar{x} + \gamma(x_r - \bar{x})$. If the value of the function in the contracted point is lower than the value in the reflected, the point is accepted and the iteration is finished, otherwise, the simplex is shrinked (see step 6).

   - **Inside**. If $f(x_r) \geq f(x_{n+1})$, an inside contraction is performed as $x_{cc} = \bar{x} - \gamma(\bar{x} - x_{n+1})$. If the value of the function in the contracted point is lower than the value in the original one, $f(x_{cc}) < f(x_{n+1})$, the point is accepted and the iteration is finished, otherwise, a shrink was performed.

6. **Shrink**. The simplex for the next iteration keeps the first point x_1 and the rest are calculated as $v_i = x_1 + \sigma(x_i - x_1)$, $i = 2, \ldots, n + 1$.

The coefficients ρ, χ, γ and σ are usually known as reflection, expansion, contraction and shrinkage coefficients. Standard values [Lagarias et al., 1998] were used: $\rho = 1$, $\chi = 2$, $\gamma = 1/2$ and $\sigma = 1/2$.

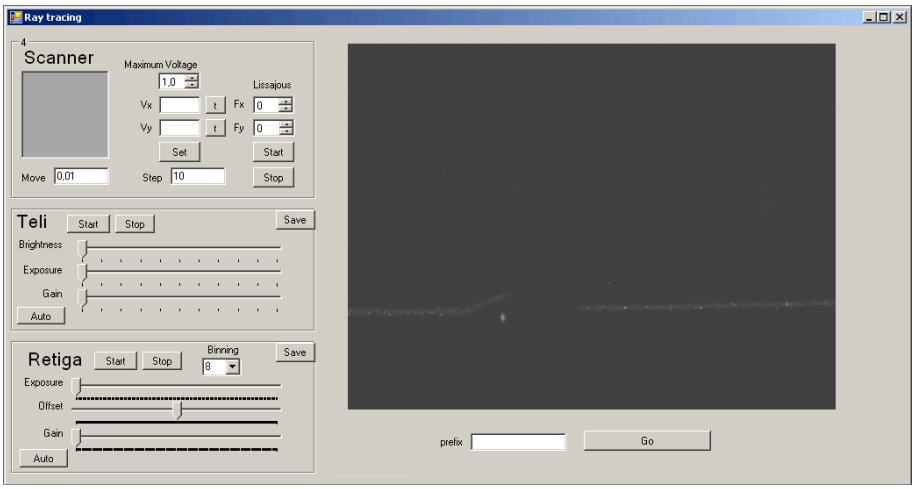

Figure 2.4: Snapshot of the Visual Basic program developed to control the scanner and the CCD cameras. One of the cameras took images of the lateral view of the ray tracing (one of them is shown in the image) and another imaged the ray directly.

2.4 Experimental measurements systems

2.4.1 Ray Tracing

A Laser Ray Tracing system that allows collection of the rays deflections (on a lateral viewing camera) as well as rays impacts behind the lens (on a second transverse viewing camera) was developed. Figure 2.5 and 2.6 show a schematic view of the system and examples of collected images and a photograph of the system respectively. A He-Ne laser (633 nm) was used for illumination, and an x-y galvanometer scanner (Cambridge Technology) deflected the laser to scan the pupil at different locations. The ray beams were delivered sequentially, sampling the lens (in 100 μm steps) two dimensionally across an 8-mm pupil. Measurement was automatized with a Visual Basic program, the measurement time was around 2 minutes per scan.

In the first mode (lateral viewing, Figure 2.5a), the lens was placed in a chamber and this was filled in with distilled water. A CCD camera (Toshiba Teli, 640x480 pixels, 7.4 μm pixel size) focused at the meridional plane of the lens, recorded images of the refracted rays (Figure 2.5b). In the second mode (transverse viewing, Figure 2.5c) the lens was placed in air and the

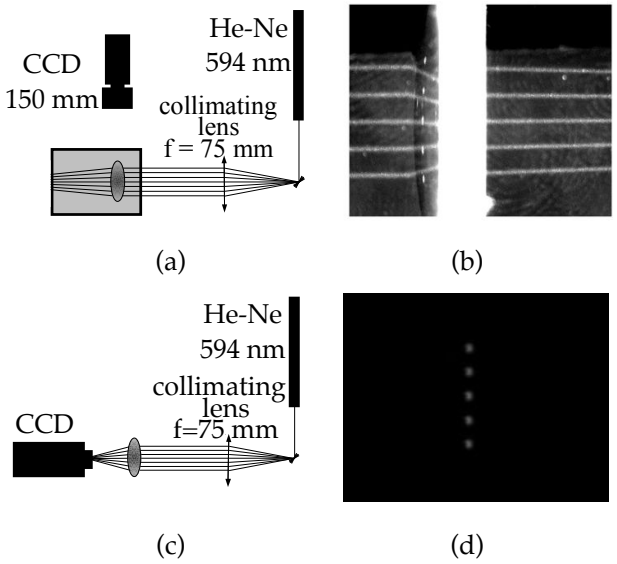

Figure 2.5: (a) Experimental setup for lateral ray tracing system (b) Corresponding ray images (integrated image of five rays) (c) Single-pass ray tracing configuration to measure the spot diagram in a plane after the lens. (d). Corresponding spot images for five rays. (Reproduced from de Castro et al. [2011a], Optics Express)

impacts of the outgoing rays with a plane perpendicular to the optical axis of the set-up were captured directly onto a bare CCD (Qimaging Retiga 1300, 6.7 μm pixel size, Figure 2.5d).

2.4.2 Optical Coherence Tomography systems

Two custom-developed anterior segment Optical Coherence Tomography (OCT) systems were used to collect the experimental OCT images in this thesis. One system was developed at the Laboratory of Jean Marie Parel and Fabrice Manns [Uhlhorn et al., 2008], at the Bascom Palmer Eye Institute (University of Miami), where it is combined with a stretcher device to simulate accommodation (not for the data presented here). The system is used in combination with a optical comparator system to measure the shape of crystalline lenses in vitro [Rosen et al., 2006]. A second system was developed at the Visual Optics and Biophotonics Laboratory, at the Instituto de Óptica (CSIC), in collaboration with Copernicus University [Grulkowski

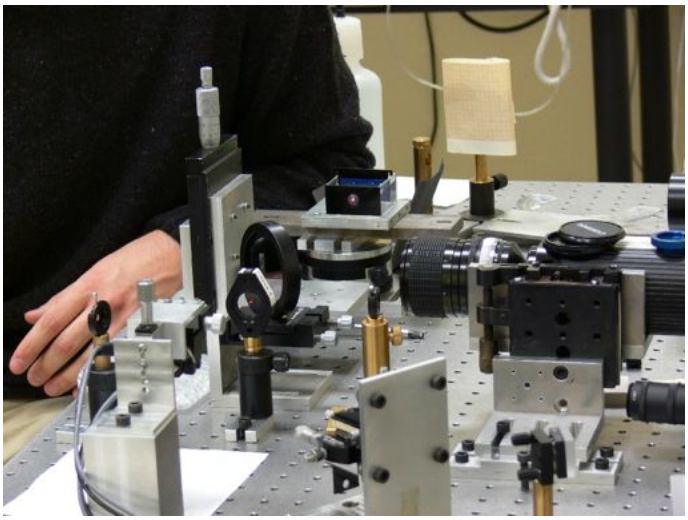

Figure 2.6: Experimental setup for lateral and single pass ray tracing. This system was also used for other projects. In the image, double-pass images are being recorded using an artificial cornea.

et al., 2009]. The instrument is normally used in in vivo and in vitro measurements of the cornea and crystalline lens in parallel experiments in our laboratory. This system was provided with algorithms developed in our laboratory for segmentation of the surfaces and correction of the distortion produced by the scanning architecture (fan distortion) [Ortiz et al., 2009].

Time-domain 2-D Optical Coherence Tomography system

The time domain OCT system was custom-built in the Ophthalmic Biophysics Center (Bascom Palmer, Miami) [Uhlhorn et al., 2008] to acquire cross-sectional images of the whole in vitro crystalline lens. The light source is a superluminescent diode with a Gaussian emission centered in 825 nm and a bandwidth of 25 nm, and an output power of 6 mW (SLD-38-HP, Superlum, Cork, Ireland). Sensitivity is 85 dB. The system has 12 µm axial resolution and imaged a maximum lateral length of 20 mm with a scan length in tissue of around 7.5 mm.

The beam delivery system uses a telecentric scanner to produce a flat scan field. The depth of focus of the delivery system was chosen to nearly

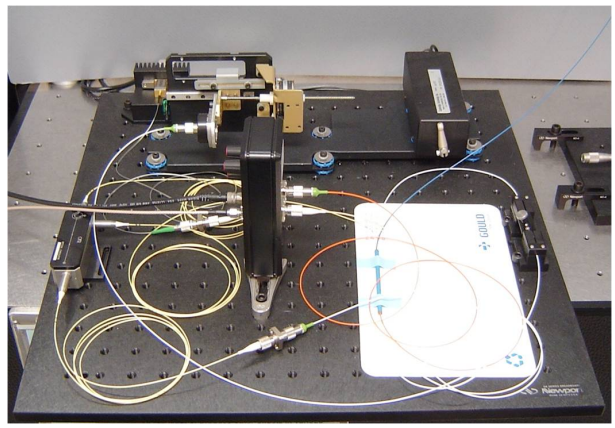

Figure 2.7: Time domain OCT of the Bascom Palmer Eye Institute used to image in vitro crystalline lenses.

match the axial scanlength of the OCT system (around 10 mm) and the beam diameters is 60 µm. The delivery system was aligned so that the midpoint of the interferometer scan depth coincides with the beam waist of the focused beam. Images were recorded with 5000 points in each A-Scan at a rate of 20 A-lines/s.

Spectral-domain 3-D Optical Coherence Tomography system

Fourier domain OCT using spectrometers or frequency swept lasers can dramatically improve the detection sensitivity and allow higher scan speeds than standard time domain OCT. In the OCT system used, a spectral fringe pattern (chanelled spectrum) is recorded by a spectrometer with a line-scan camera. A tomogram line is calculated by unevenly sampled Fourier transformation of the recorded fringe pattern. Since this method does not require mechanical depth scanning, it can perform imaging much faster.

The system was developed in collaboration with Nicolaus Copernicus University (Toruń, Poland) [Grulkowski et al., 2009] to image the anterior segment of the human eye two and three-dimensionally. A schematic diagram of the system can be seen in Figure 2.8. The set-up is based on a fiber-optic Michelson interferometer and uses a super luminescent diode with a nearly Gaussian emission centered in 840 nm and a bandwidth of 50 nm (Superlum, Ireland) as light source and a spectrometer consisting of

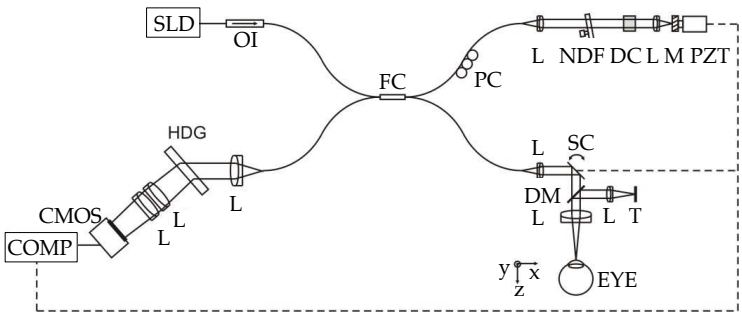

Figure 2.8: Layout of the spectral-domain OCT setup: SLD – superluminescent diode, OI – optical isolator, FC – 80:20 fiber coupler, PC – polarization controller, NDF – neutral density filter, DC – dispersion compensator, L1-L8 – lenses, M – silver mirror, PZT – piezotranslator, SC – galvanometric scanners, DM – dichroic mirror, T – target, HDG – holographic volume diffraction grating, CMOS – linescan camera, COMP – computer. (Reproduced from Grulkowski et al. [2009], Optics Express).

a volume diffraction grating and a 12-bit line-scan CMOS camera with 4096 pixels as detector. The signal to noise rate (SNR) of the instrument was estimated to be 97 dB. Acquisition speed was 25000 A-Scans/s resulting in an integration time of 40 nm. An unfolding mode used a piezoelectric motor to extend the axial range of the system up to 10 mm in air. A single 3-D image consisted of 1668 A-scans and 70 B-scans in a lateral range of 12x12 mm with a resolution of 170x7 μm. The axial range of the instrument is 7 mm, resulting in a theoretical pixel resolution of 3.42 μm and the axial resolution predicted by the bandwidth of the super luminescent diode is 6.9 μm. The acquisition time of a full 3-D image was 4.5 seconds.

If needed, to ensure optimal signal from both lens surfaces, two 3-D images were obtained per condition at two different focal planes. The images were merged using the cuvette as a reference to produce a full 3-D image of the crystalline lens. The merging algorithm was developed in MatLab. Figure 2.10 shows a full 3-D view of the crystalline lens.

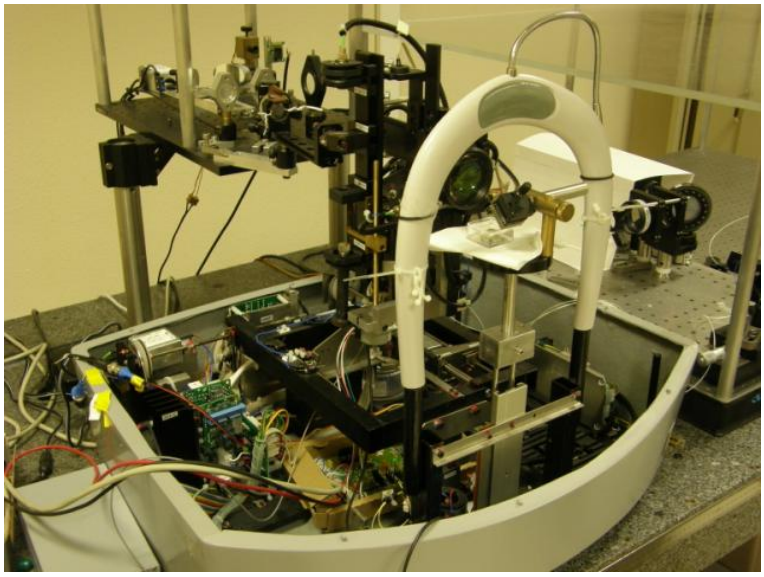

Figure 2.9: The spectral domain OCT imaging a crystalline lens.

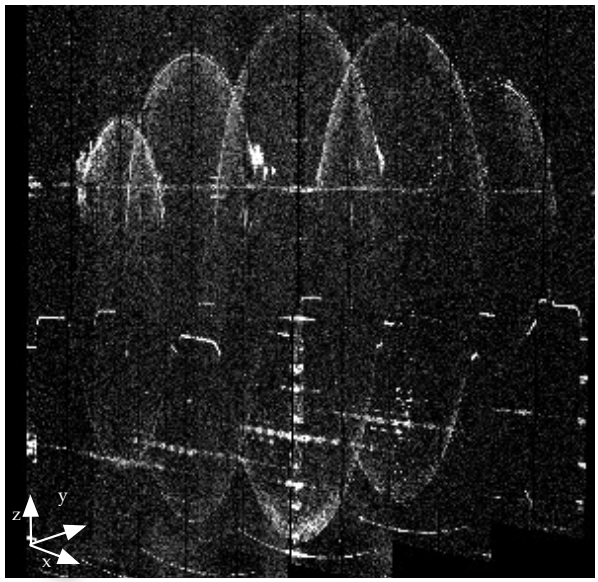

Figure 2.10: Five of the sixty B-scans of the crystalline lens obtained with the OCT.

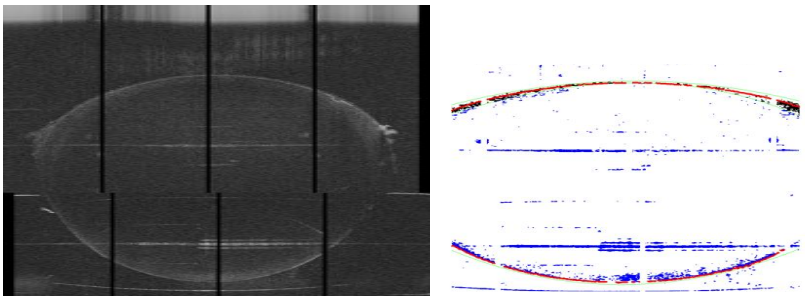

Figure 2.11: A-Scan extracted form OCT (left) and anterior and posterior surface detected (right)

2.4.3 Optical Coherence Tomography data analysis

OCT images were corrected for fan distortion, which arises from the scanning architecture. If the fan of principal rays is not perfectly flat with respect to the optical axis of the system, the surfaces are not well reproduced and even the image of a flat surface becomes curved. This effect can be characterized and minimized numerically by application of correction algorithms based on ray propagation and Snell's law. To correct the distortion in the images used in this thesis we have used an algorithm developed previously in our laboratory [Ortiz et al., 2009].

The improvement achieved when using the fan distortion correction algorithm was studied in a posterior work by Ortiz et al. [2011]. We imaged three-dimensionally spherical and aspheric lenses as well as 10 human corneas in vivo. The results of sOCT were compared with non-contact profilometry on the spherical lenses and state of the art commercial corneal topography instruments on aspheric lenses and subjects. We found that the mean discrepancy in the estimated radius of curvature from nominal values in artificial corneas decreased from 4.6% (without fan distortion correction) to 1.6% (after fan distortion correction), and the difference in the asphericity decreased from 130% to 5%.

According to the differences in reflectivity, we developed two different strategies for the detection of the surfaces of the crystalline lens and the cuvette used in the in vitro measurements. For the anterior surface, the segmentation algorithm searched the maximum of intensity in each A-scan, and for the posterior surface the segmentation algorithm is based on edge detection of the thresholded image. The surface of the distorted cuvette was

segmented using the first method. The detection algorithms were implemented in MatLab.

Chapter 3

Accuracy of the reconstruction with optimization methods from Ray Tracing and Optical Coherence Tomography data

This chapter is based on the article by de Castro et al. [2011a]: "Accuracy of the reconstruction of the crystalline lens gradient index with optimization methods from Ray Tracing and Optical Coherence Tomography data," Optics Express 19(20), 19265–79, 2011.

The contribution of the author of this thesis to this study was the performance of experimental measurements, programming of the simulations, analysis of both experimental and simulations results and writing of the manuscript.

The coauthors of the study are Sergio Barbero, Sergio Ortiz and Susana Marcos.

3.1 Introduction

In this thesis we developed a new optimization method to retrieve the gradient index of refraction (GRIN) of the crystalline lens from experimental data obtained with Optical Coherence Tomography (OCT) and Laser Ray Tracing. Optimization methods are based on finding the optical parameters of a specific lens model to fit certain experimental data. Pomerantzeff et al. [1971] used as experimental data the focal length and the spherical aberration of the eye, and a shell model lens composed of a large number of layers. Each layer thickness, radius of curvature and refractive index was changed according to a third degree polynomial. The minimization algorithm searched the variables of the polynomial to fit focal length and spherical aberration of the eye. The high number of unknown variables made the optimization problem ill-defined since, as Campbell and Hughes [1981] noted, multiple solution were possible.

Axelrod et al. [1988] and Garner et al. [2001] reconstructed a spherical GRIN using as input data those extracted from lateral view of the ray tracing through a fish lens. Barbero et al. [2004] studied the possibilities of using this direction cosine data and global search optimization for finding the optimal parameters in non-spherical lenses.

The potential of using OCT to extract information of the GRIN was studied by Ortiz et al. [2004], and the first data on a simple spherical fish lens using optical path differences (OPD) from OCT were provided by Verma et al. [2007].

Local search algorithms were sufficient in several of the cases above, due to simplicity and symmetric properties of the GRIN models used. In this chapter, we compared the accuracy and robustness of the optimization methods to reconstruct the GRIN using different input experimental data. Three realizations of the Goncharov model, with increasing number of variables were tested. The evaluation was performed based on computer simulations, and the noise expected in each input data estimated from experimental data collected on artificial lenses with the ray tracing setup and the OCT imaging system described in section 2.4. The effect of measurement error and experimental limitation of each technique are addressed.

3.2 Methods

Experimental measurements on artificial lenses provided real error data of the input information to the reconstruction algorithms. The experimental data acquisition was then simulated computationally on human crystalline lenses, assuming the Goncharov lens models. Ray tracing data (direction cosine of the deflected ray, intercept of the outgoing ray with the posterior lens surface and impact on a plane after the lens) and OCT imaging data (OPD) of the lenses were simulated. The merit function and optimization tools were applied on the simulated data (using the errors obtained experimentally) to reconstruct the GRIN. To quantify the accuracy of the reconstruction, the root mean square (RMS) error of the difference between the reconstructed GRIN and the nominal GRIN was used (GRIN RMS difference). For the computation of GRIN RMS difference the refractive index was evaluated for both the reconstructed and nominal GRIN on a grid of points (10 μm separation) over a 6 mm pupil. The metric is dimensionless and increases with increasing discrepancy of the reconstructed GRIN with respect to the nominal GRIN.

3.2.1 Estimation of experimental errors

Ray tracing measurements on artificial lenses

With the ray tracing system described in section 2.4.1, we collected data of direction cosines of the rays deflected by the lens and impacts in a plane after the lens of a homogeneous index lens (KPX088, Newport, f = 71 mm, D = 25.4 mm) and a gradient index lens (GPX-30-60, LightPath, f = 75 mm, D = 30 mm) to estimate the error in the measurement. The GRIN lens had a continuous axial decreasing variation of refractive index from 1.74 (anterior surface) to 1.67 (posterior surface), and a central thickness of 6 mm. The nominal GRIN profile was described by a 7^{th} order polynomial function. Data from 80 equally spaced rays sampling an 8 mm pupil were analyzed in five repeated measurements.

Optical Coherence Tomography measurements on artificial lenses

With the spectral-domain OCT described in section 2.4.2 we imaged two homogeneous lenses (EO 45-447 and EO 45-705, Edmund Optics, f = 60 and 72 mm respectively, D = 12.5 mm). Data of OPD of the rays between anterior and posterior surface were extracted three-dimensionally to estimate the

error of the measurement in all directions. The OPD was calculated in an 8 mm pupil range in five repeated measurements of each lens.

3.2.2 Studied gradient refractive index models

The crystalline lens was described using three different GRIN models, proposed by Goncharov and Dainty [2007]. One of the models was personalized for an individual eye in a later work [Goncharov et al., 2008]. The first and second GRIN models are defined by two 4^{th} order polynomials in radial and axial direction describing the GRIN distribution in anterior and posterior regions of the lens respectively. In the first model (unbalanced model, G20U), the refractive index is constant over the lens surfaces and the GRIN distribution is determined only by two variables: surface and nucleus refractive indices. In the second model (balanced model, G20B), the last posterior iso-indicial surface may not be coincident with the posterior lens surface and GRIN distribution is described by three variables: surface and nucleus refractive indices and radius of curvature of the posterior iso-indicial surface. The third model (symmetrical model, G20S) assumes a GRIN distribution with one polynomial described by four variables: surface and nucleus refractive indices, center position and a parameter setting the decay of the refractive index along the radial coordinate —this parameter could be related to the refractive index 3 mm off the optical axis, at the meridional plane. In this model, the marginal iso-indicial surfaces are more curved than the external surfaces.

As we observed that the merit function of the 2-variable model can be optimally minimized simply using the local search algorithm, we did not use the global search algorithm in this model. For the 3-variable and 4-variable models, the genetic algorithm was composed of 5 generations containing 200 individuals each, and 20 generations of 600 individuals respectively. Constraints —needed in presence of large experimental errors— were applied to the range of refractive indices in the nucleus and surface as well as the nucleus lens position, according to biologically plausible descriptions of the GRIN distribution. These constraints were included in the merit function using penalty terms [Vasiljević, 2002]. For all the models, the refractive index was constrained to have a value between 1.355 and 1.44, which fits most of refractive index values in human crystalline lenses found in the literature. For the 4-variable model, the position of the lens nucleus was constrained to a range from 1.1 to 1.8 mm. This constraint is justified by the observation

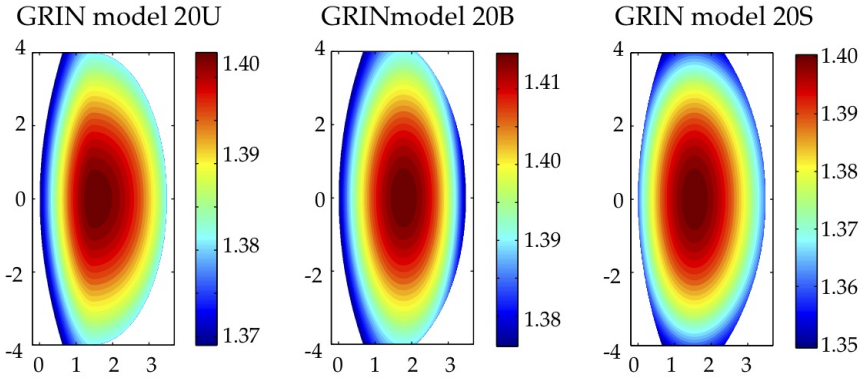

Figure 3.1: Gradient refractive index proposed by Goncharov and Dainty [2007] for a 20 year old crystalline lens. G20U variables are the nucleus and surface refractive index, B20B has one additional variable, the radii of the last posterior isoindicial surface and B20S variables are nucleus and surface refractive index, center position on axis and decay in meridional axis.

that values outside of this range can generate two refractive GRIN maxima. Finally, the refractive index at 3 mm off the optical axis (radial coordinate) was constrained between 1.35 and the nucleus refractive index value. This constraint forces a decrease of the GRIN profile along the radial direction, which is in accordance to the morphology of the crystalline lens.

3.2.3 Simulations

In all the simulations we assumed that the experimental data are limited to rays parallel to the optical axis, and within a 6 mm pupil diameter. Unless otherwise noted, 120 rays were traced, i.e. one ray each 50 μm across the 6 mm pupil.

The reconstruction algorithm was tested assuming simulated input data for five different configurations (three from laser ray tracing, and the other two from OCT):

1. Deflections of rays outgoing the lens, as used in previous studies to reconstruct GRIN distributions [Campbell, 1984; Garner et al., 2001].

2. Deflections of outgoing rays and intercepts of these with the posterior lens surface, as was used in the tomographic method proposed by

Acosta et al. [2005] and Vazquez et al. [2006].

3. Ray impacts on a CCD placed after the lens, as shown in Figure 2.5.
4. OPD of each ray intercepting the posterior lens surface, as used in some OCT-based reconstruction methods [Verma et al., 2007; de Castro et al., 2011b].
5. OPD of each ray that intercepts the posterior lens surface as well as the cuvette surface holding the lens (which can be imaged with the OCT in in vitro measurements [Uhlhorn et al., 2008], as used in our publication [de Castro et al., 2010] that will be described in chapter 4.

If a broad band source is used, as it is the case in configurations 4 and 5, the experimental data are associated to the group refractive index. However, as the ray tracing algorithm implicitly uses a phase refractive index, we assume that the refractive index reconstructed with the algorithm is equivalent to the group refractive index. The relation between group and phase refractive index is studied in the introduction (section 1.2.8). For clarity purposes, in the simulations of this study we used the same refractive index for the five configurations.

To explore the limits of the search algorithm in each configuration, we have reconstructed the GRIN distribution assuming no error in the experimental data, and low noise level (range of Gaussian errors ranging from 10^{-6} to 10^{-3}) added to the data. The aim of this simulation was to evaluate the reconstruction accuracy of the algorithm itself.

The reconstruction algorithm was then studied when expected experimental noise level was applied to the input data (direction cosines, impacts of OPDs). Noise was simulated introducing Gaussian error with a standard deviation calculated with the experimental ray tracing and OCT imaging described in methods chapter.

As the lens geometry represents additional input information for the GRIN reconstruction algorithms, we also studied the influence of the experimental errors of the lens shape measurements. The simulation of the ray tracing data was performed on lens surfaces where Gaussian noise (standard deviation given by the error measurement estimated with glass lenses) was added to surfaces radii of curvature. As before, the experimental error was also introduced in the input data (direction cosines, intercepts of the outgoing rays with posterior surface, impacts or OPDs). The GRIN reconstruction was evaluated using the nominal lens surface radii.

Finally, we studied the influence of the number of rays (ranging from 6 to 1200) in the reconstruction.

3.3 Results

3.3.1 Limits of the reconstruction algorithm based on laser ray tracing and Optical Coherence Tomography input data

Figure 3.2 shows the RMS of the difference between the nominal and reconstructed GRIN (GRIN RMS difference) for the three GRIN models studied and for the five proposed experimental configurations. The simulations were conducted assuming no input error and with added Gaussian errors (10^{-6} to 10^{-3}) to the input data (for all conditions). In absence of experimental errors, the GRIN was reconstructed with high accuracy (GRIN RMS difference $< 10^{-8}$) indicating that the global minimum can be theoretically retrieved for all the GRIN models and all conditions under study. As expected, the presence of experimental errors increases the reconstruction error. Also, the reconstruction accuracy decreases with the complexity (number of variables) of the lens model.

3.3.2 Estimation of the experimental errors

The experimental set-ups described before (LASER ray tracing system and spectral domain OCT) were used with artificial lenses to obtain estimates of the experimental errors of the input data.

Figure 3.3 shows the differences, for all rays, between the experimental and the simulated direction cosines of the rays deflected by the lens (a), impacts on a plane after the lens (b) and OPD (c) data for the artificial lenses under study. The standard deviation of the differences in each case was: $1.08 \pm 0.49 \cdot 10^{-3}$ for the homogeneous lens and $0.92 \pm 0.14 \cdot 10^{-3}$ for the GRIN lens (direction cosines); $6.0 \pm 2.2\,\mu m$ for the homogeneous and $6.9 \pm 0.3\,\mu m$ for the GRIN lens (ray impacts); and 2.40 ± 0.17 and $2.74 \pm 0.18\,\mu m$ (OPDs) for the two lenses under test.

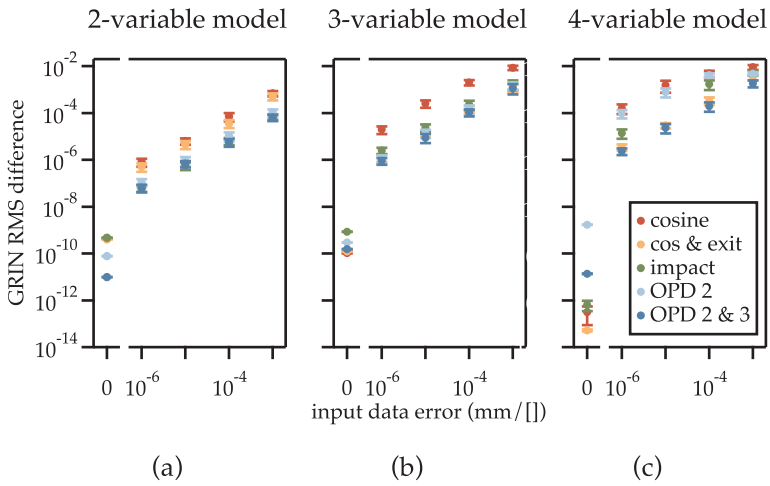

Figure 3.2: Difference between nominal and reconstructed GRIN (GRIN RMS difference) as a function of the experimental error of the input data. Data are the mean across 50 repetitions, and the error bars represent standard deviations. (Reproduced from de Castro et al. [2011a], Optics Express).

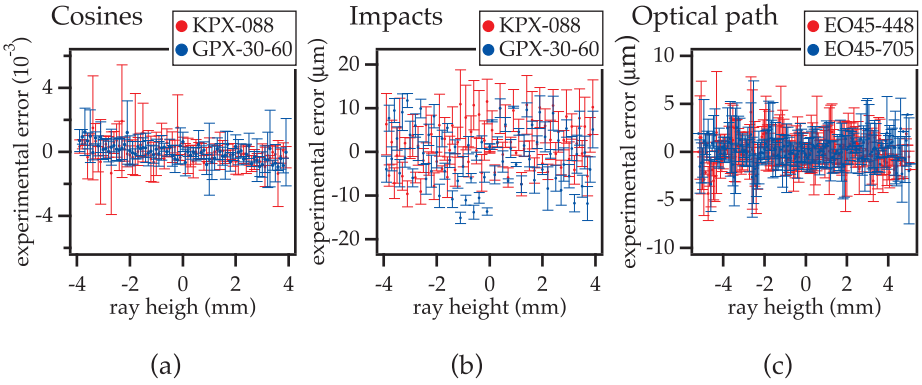

Figure 3.3: Difference between experimental and simulated data: mean and standard deviation for five repeated measurements. (a) Direction cosine of the outgoing rays, (b) Impacts on a plane after the lens and (c) OPD through the lens. (Reproduced from de Castro et al. [2011a], Optics Express).

3.3.3 Influence of experimental errors on the gradient refractive index reconstruction

The reconstruction algorithm was evaluated for different sets of simulated input data representing the 5 proposed experimental configurations (direction cosines of deflected rays, direction cosines and intercept of the outgoing rays with the posterior lens surface, impacts on a plane after the lens, optical path up to the posterior surface of the lens, and optical path up to the posterior surface of the lens and to a plane after the lens) with three different levels of experimental error and for the three Goncharov models.

For illustration purposes, we defined three different error levels: errors within the expected order of magnitude of the experimental measurements (error level R), lower (error level L) and higher (error level H) than the expected experimental error.

The simulated errors of the ray direction cosines were 0.5, 1 and $2 \cdot 10^{-3}$ for the error levels L, R and H respectively; the simulated errors of the intersection points (intercept of the outgoing ray with posterior lens surface and impact on a plane after the lens) were 3, 6 and 12 μm; and the simulated errors of the OPD 1.5, 3 and 6 μm for the error levels L, R and H respectively.

Figure 3.4 shows the mean value and the standard deviation of the GRIN RMS difference of the nominal and the reconstructed GRIN for 50 realizations of the reconstruction algorithm.

We found that, for many conditions, the reconstruction error increases with GRIN model complexity. For the three GRIN models, the best reconstructions were achieved using the input OPD data from OCT (with the lowest error occurring for the condition that used OPD data of both the posterior lens surface and cuvette). Increasing the error of the input data (L, R and H) increases the reconstruction error. Whereas all configurations induced low reconstruction errors (GRIN RMS difference < 0.005) for the two-variable Goncharov model, for three and four-variable Goncharov models the errors were higher when using the cosine and impact as input data.

Figure 3.5 shows the spatial distribution of the reconstruction error in the different conditions, across the axial and meridional axes for the 4-variable GRIN model and the error level R.

The error of the reconstructed refractive index is of the same order of magnitude in both the axial and meridional planes, although the error is slightly higher along the axial coordinate. Also, the error tends to increase towards the surface for most configurations.

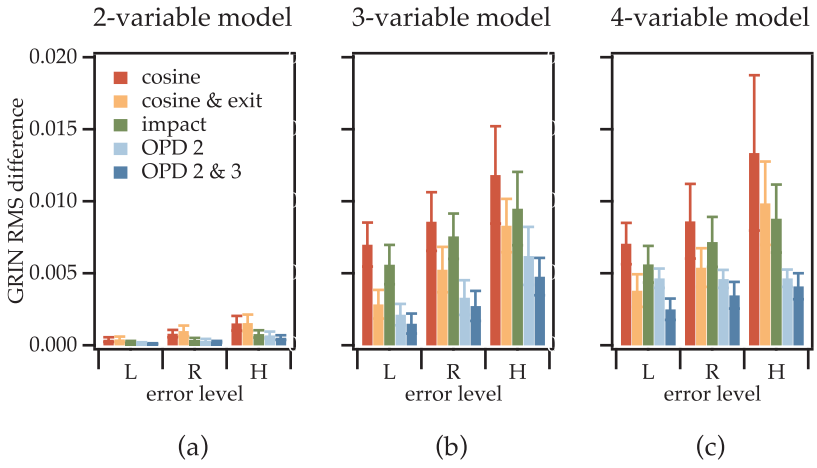

Figure 3.4: Axial (a) and meridional (b) deviation from the nominal GRIN profile for the proposed experimental configurations, for realistic input data error levels (R) and the 4-variable Goncharov model. Data represent the mean value and the error bars the standard deviation of 50 repetitions of the reconstruction algorithm. (Reproduced from de Castro et al. [2011a], Optics Express).

3.3.4 Influence of the surface shape measurement error on the gradient refractive index reconstruction

We found discrepancies in the measured radius of curvature of $1.02 \pm 1.16\%$ and $1.05 \pm 0.54\%$ for the two measured lenses. These results are in good agreement with previous studies of the group [Ortiz et al., 2010, 2011], where the error was found to be around 1%.

We estimated the relative contribution to the GRIN reconstruction induced by the surface shape measurement error (estimated in 1%) and the experimental input data errors (level R). Comparisons were made between the results of the simulations with and without errors in the surface shape measurement. Figure 3.6 shows the GRIN RMS difference for a 4-variable GRIN model with error in both the surface and input data, relative to the reconstructed GRIN with only input data errors. We found that the relative contributions of the surface errors in the reconstructed GRIN were significant ($p < 0.01$) in the configurations using direction cosines and intercept of the outgoing rays with posterior lens surface points (35%), OPD up to the

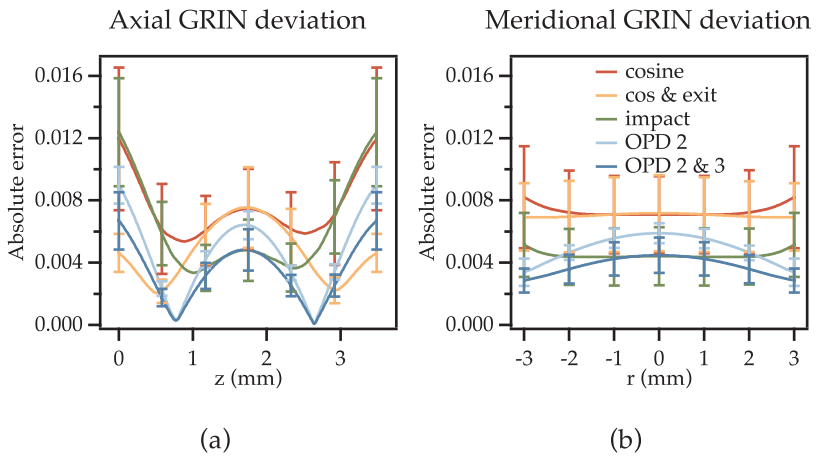

Figure 3.5: Axial (a) and meridional (b) deviation from the nominal GRIN profile for the proposed experimental configurations, for realistic input data error levels (R) and the 4-variable Goncharov model. Data represent the mean value and the error bars the standard deviation of 50 repetitions of the reconstruction algorithm. (Reproduced from de Castro et al. [2011a], Optics Express).

posterior surface of the lens (20%) and OPD up to the posterior surface of the lens and cuvette (40%).

3.3.5 Influence of the ray sampling density on the reconstruction of the gradient refractive index

We studied the effects of changing the number of input data in the reconstruction algorithm, or equivalently, increasing the corresponding number of rays in the laser ray tracing sampling pattern or increasing the number of A-scans in a cross-section of the OCT images.

While the pupil diameter was kept constant (6 mm), 7 different ray sampling densities were studied ranging from 6 to 1200 total rays, i.e. ray separation distance between 1 mm and 5 µm respectively. All simulations were performed for an error level R, and for the 4-variable Goncharov model, for the 5 proposed experimental configurations.

Figure 3.7 shows the GRIN RMS difference as a function of number of rays traced. The reconstruction improves as the number of rays increases,

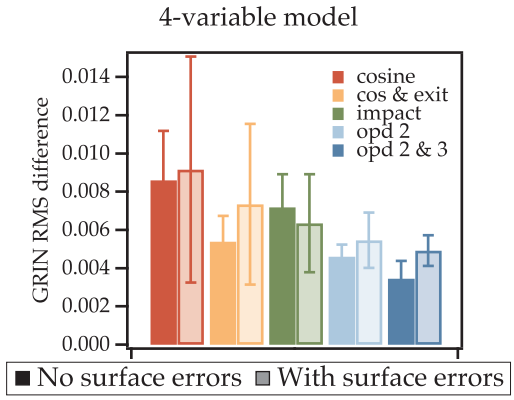

Figure 3.6: GRIN RMS difference of the reconstructed and the nominal GRIN data, with realistic error level (R) in the input data without error int he surface shape (solid colors), and with a random deviation of the surface geometry of 1% (light colors). The bars represent data and the error bars, the standard deviation of 50 repetitions of the reconstruction algorithm. (Reproduced from de Castro et al. [2011a], Optics Express).

although beyond 100 rays the changes are minor. The impact of the number of rays on the accuracy of the reconstruction is lower for the OCT-based input data than for the laser ray tracing-based input data.

3.4 Discussion

The reconstruction method based on optimization techniques was applied in this chapter to laser ray tracing (ray direction cosines and impacts) and optical coherence tomography input data. We have studied the GRIN reconstruction accuracy and the influence of the experimental errors of the different input data.

In the absence of experimental errors the algorithm has been proved to be sufficiently robust to reconstruct GRIN data for different GRIN models. In the presence of the estimated experimental errors, obtained using custom-developed laser ray tracing and OCT experimental devices, OCT-based data allowed highly accurate reconstructions (GRIN RMS difference < 0.005) of the GRIN. Also, the use of OCT-based input data appears less susceptible to errors in the surface radii of curvature, and also on the number of rays.

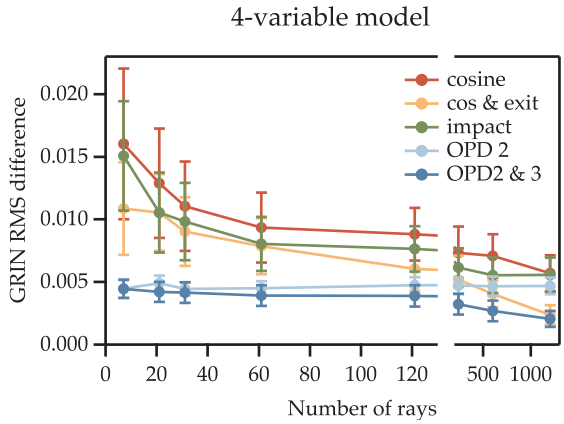

Figure 3.7: GRIN RMS difference of the reconstruction for the 5 proposed experimental configurations and with realistic error level R, versus number of rays. Pupil radius was set to 6 mm pupil. Data represents mean value, and the error bars, the standard deviation of 50 repetitions of the reconstruction algorithm. (Reproduced from de Castro et al. [2011a], Optics Express).

This indicates that OPD is a suitable method for retrieving the GRIN of the crystalline lens. The superiority of the optimization when using OPD data over the rest proposed in this study (direction cosines, intercept of the outgoing rays with posterior lens surface or impacts in a plane after the lens) might result from the more direct information on the GRIN that the OPD accumulates at the end of the ray trace. The accuracy of the reconstruction increased when incorporating additional information –at least for the levels of error studied– to the input data: adding the intercept of the outgoing ray with the posterior lens surface in addition to the direction cosines in the ray tracing procedure (configuration 2 versus 1), and adding cuvette OPD in addition to the lens OPD in OCT (configuration 5 versus 4).

To test the flexibility of the reconstruction algorithm, we used three GRIN models [Goncharov and Dainty, 2007] with increasing number of variables. The accuracy of the reconstruction decreased slightly when increasing the complexity of the model. The reconstruction algorithm can be used with other GRIN models. In chapter 4 the precision is studied in the reconstruction of an exponential 4-variable GRIN model and a similar accuracy is found (GRIN RMS difference of $4 \cdot 10^{-3}$) using OCT-based input data (posterior lens and cuvette distortions), as in configuration 5 and an estimated error of 5 μm

in the OPD.

A common problem to all optimization techniques is local minimum trapping, and the possible existence of multiple solutions. Since the merit function used is not described analytically, the absence of local minima or the existence of multiple solutions cannot be proved mathematically. However, the use of a global instead of a local search algorithm prevents local minimum trapping and the large set of multiple experimental input data and relatively low number of unknown variables reduces the possibility for several solution with the same merit function value.

The reconstruction algorithm and the error analysis for the various experimental approaches presented can be compared to those of previous studies. Vazquez et al. [2006] proposed a reconstruction algorithm based on laser ray tracing at different orientations to reconstruct a non-spherical GRIN. They simulated a Gaussian error of less than 1 μm. With data from orientations up to 80°, the RMS of the GRIN reconstructed was below 10^{-4} for a GRIN described by a 9-variable single polynomial and around 10^{-3} for a GRIN described by two polynomial expressions (strong GRIN). The RMS reconstruction error, if only orientations up to 10° were available, was $> 10^{-3}$ in both cases. In comparison, our reconstruction method, when using the same simulated input error, achieved a reconstruction error $< 5 \cdot 10^{-3}$ for the 4-variable GRIN model, which is comparable to the results by Vázquez et al. (with input data up to 10°). It is worth noting that our reconstruction algorithm could be extended for laser ray tracing data at different orientations. Although this was not studied in this thesis it is likely that the accuracy would increase further by incorporating input data obtained at different orientations. Verma et al. [2007] used OCT-based input data and an optimization algorithm (nonlinear least squares fitting) to reconstruct a spherical GRIN lens. Simulating a Gaussian noise of 11 μm they obtained a maximum error of around 0.013. We reproduced their simulations with our local search algorithm finding similar results (maximum error 0.010 and GRIN RMS difference of $5 \cdot 10^{-3}$).

There are other possible sources of experimental error, not addressed here, such as decentration or tilt of the lens, or inaccurate positioning of the ray entrance, which would affect the outcomes. However, several of these errors can be minimized when obtaining three-dimensional input data (particularly in the OCT based technique, where the surfaces of the lens are visualized directly). As it was mentioned in section 2.3, the refractive index retrieved from the reconstruction algorithm in configurations 4 & 5

is assumed to be equivalent to the group refractive index. The resulting index can be converted from the group to the phase refractive index at the central wavelength of the OCT light source and subsequently to a different wavelength using available data of the chromatic dispersion of the crystalline lens [Uhlhorn et al., 2008; Atchison and Smith, 2005].

The techniques described here are designed for estimations of the GRIN of the crystalline lens in vitro. However, the estimation of the GRIN distribution of the lens in vivo would be of major interest to understand the contributions of GRIN to the optical properties of the eye, and its influence in the optical changes with accommodation and aging, particularly considering that the shape of the isolated crystalline lens differs from its unaccommodated state in vivo. To date, all the laser ray tracing GRIN reconstruction methods have proposed imaging lateral ray deflections which are unavailable in vivo. In contrast, we have demonstrated that relatively good reconstruction performances (GRIN RMS difference < 0.01) can be obtained when using transverse imaging of the impacts after the lens. These impacts can actually be available in vivo (with additional contributions of the cornea) in a double-pass configuration as routinely shown in laser ray tracing (LRT) measurements of the wave aberrations in the eye [Moreno-Barriuso and Navarro, 2000; Moreno-Barriuso et al., 2001] although the algorithm also requires knowledge of the posterior shape of the crystalline lens. Nevertheless, while the OCT-imaging-based technique described here works with in vitro samples, it is likely that this technique, in combination with an in vivo LRT-based technique, operating at wide angles if possible, would provide sufficient information for attempting a reconstruction of the GRIN in vivo through optimization techniques.

3.5 Conclusions

The use of optimization methods to extract information of the gradient index of the crystalline lens using different experimental data was studied. In absence of experimental error the algorithms converged to the nominal GRIN and the accuracy of the reconstruction using different experimental data and different level of errors was proved to be of the same order of magnitude compared to that achieved with other methods. This implies that the use of optimization methods with low number of variables GRIN models is possible.

For the goals of this thesis, the results of the studies presented in this chapter indicate that the best experimental strategy for the reconstruction of the GRIN is based on Optical Coherence Tomography. Not only the accuracy studies results suggest that the GRIN is less sensitive to errors in OPD, but also, OCT systems are becoming increasingly used for anterior segment imaging as well as decreasing adquisition time. In the next chapters, we will use OCT images to study the gradient index on porcine and human crystalline lenses.

Chapter 4

Three-dimensional reconstruction of the crystalline lens gradient index distribution from Optical Coherence Tomography imaging

This chapter is based on the paper by de Castro et al. [2010]: "Three-dimensional reconstruction of the crystalline lens gradient index distribution from OCT imaging," Optics Express 18(21), 21905–17, 2010.

The author of this thesis took part in the experimental measurements (together with other coauthors), designed and programmed the simulations to validate the reconstruction with the GRIN model used, developed the algorithms to segment the surfaces in the OCT images, applied the reconstruction method described in previous chapters and analyzed the results.

The coauthors of this study were Sergio Ortiz, Enrique Gambra, Damian Siedlecki and Susana Marcos.

4.1 Introduction

In the previous chapter we analyzed the potential of using optical path differences (OPD) in the reconstructions, and found that the use of this experimental data allowed higher accuracy in the estimation of the lens gradient index (GRIN) with optimization methods. To our knowledge, only one study has attempted to use optical coherence tomography (OCT) to reconstruct experimentally the GRIN of a fish lens [Verma et al., 2007]. The application of an optimization method in the fish lens to reconstruct the GRIN from OCT images is relatively simple, as the simplicity of the GRIN model (due to the spherical symmetry of the problem) avoids local minimum problems in the optimization process.

The distortion produced by the isolated crystalline lens on the visualization of a plane surface (the base of the cuvette holding the lens) imaged with OCT technique has been previously used to estimate the physical thickness of the lens as well as the central average refractive index of human lenses of different ages [Uhlhorn et al., 2008]. The fact that the GRIN produces a significant distortion in the posterior lens surface and in the cuvette holding the lens can be actually used to attempt the reconstruction of the GRIN, provided that the lens can be measured in two orientations, as occurs in vitro.

In this chapter, we present the reconstruction method applied to a porcine crystalline lens with non-spherical geometry and a GRIN structure similar to that expected to be found in the human crystalline lens. The input data are the optical path accumulated by the rays passing through the lens measured with OCT, and the shape of the anterior and posterior crystalline lens surfaces (with the posterior directly measured in vitro by flipping the lens over), also obtained from OCT. The anatomical GRIN model used is a 4-variable model proposed by Manns et al. [2010]. The reconstruction using this model is demonstrated computationally. Three-dimensional OCT measurements allowed a full 3-D reconstruction of the GRIN structure in the porcine crystalline lens and avoided potential artifacts arising from measuring GRIN in a single meridian. Knowledge of both the surface geometry and GRIN allowed estimating the relative contribution of each to key optical aberrations as astigmatism and spherical aberration.

4.2 Methods

4.2.1 Gradient refractive index model

The model used to describe the crystalline lens GRIN structure was presented by Manns et al. [2010] and described in the introduction of this thesis (section 1.2.7). It brief, the anterior and posterior surfaces of the lens are described by conics, the GRIN follows the surface shapes with an exponential variation in the refractive index from the nucleus to the surface in both the axial and meridional directions. The center of the GRIN lies in the intersection of the optical axis and the equatorial plane. We implemented this model, setting the equatorial plane at a distance from the anterior surface vertex equal to 0.41 times the lens thickness [Rosen et al., 2006]. The GRIN can be expressed in polar coordinates as

$$n(\rho, \theta) = n_N - \Delta n \left(\frac{\rho}{\rho_S} \right)^{p(\theta)}, \tag{4.1}$$

where ρ_S is the distance from the center of the lens to the surface at angle θ; $p(\theta)$ is a monotonic function which expresses the change of the exponential decay value from the axial direction in $\theta = 0$, p_1, to the meridional direction, $\theta = \pi/2$, p_2. This function was chosen to depend on the fifth power of θ for this work; n_N is the refractive index in the nucleus of the lens, and Δn the difference between surface and nucleus refractive index.

4.2.2 Merit function

The merit function defined to search for the best GRIN fitting the optical path difference measured was defined as

$$\begin{aligned} &MF(GRIN_{coeffs}) = \\ &\quad RMS(OPD_{calc}(Surf2, GRIN_{coeffs}), OPD_{exp}(Surf2)) + \\ &\quad RMS(OPD_{calc}(Surf3, GRIN_{coeffs}), OPD_{exp}(Surf3)), \end{aligned} \tag{4.2}$$

where MF stands for the merit function as a function of the 4 variables of the GRIN ($GRIN_{coeffs}$), the RMS refers to the root mean square, OPD_{calc} is the estimated optical path difference for the posterior surface (Surf2) and the cuvette surface (Surf3), and OPD_{exp} the optical path difference measured by the OCT system. The merit function is therefore defined by the sum of the

RMS of the differences between the estimated and measured optical path differences for the posterior surface of the crystalline lens and the cuvette.

The search algorithm was described in section 2.3, it starts with a population of solutions randomly selected within the expected range of solutions. The starting population ranged from 1.36 to 1.39 for the surface refractive index (n_S), 1.38 to 1.42 for the nucleus refractive index (n_N) and 2 to 9 for the optical and meridional exponential decay (p_1 and p_2). The algorithms were set without constrains, i.e., there were not limits in the search of variable values. A schematic diagram of the rules of the algorithm was presented in figure 2.2. In brief, the merit function is evaluated in each solution and then a second population is created by selecting some of the solutions stochastically (taking into account the merit function value) and recombining (85%) two solutions (i.e. combining their variables) and mutating them (75% of recombined children) by adding Gaussian noise. Some of the best solutions of a previous iterations (5%) are directly copied to the next iteration and a few (10%) are chosen randomly. In the simulations presented here the population for each iteration was formed by 400 solutions and the process was repeated 10 times. A local search algorithm [Nelder and Mead, 1965] was then applied starting with the genetic optimization solution. The computation time was less than 45 minutes for each complete optimization using a 10 μm step in the Sharma algorithm. We tested that using different Sharma's algorithm steps below that value did not produce significant changes in the ray tracing algorithm or in the optimization results.

4.2.3 Simulations

The performance of the GRIN reconstruction method was studied simulating three human crystalline lenses (20, 40 and 60 years old) with realistic geometry and a GRIN distribution consistent with previous literature. The anterior and posterior lens surface shapes and lens thickness were obtained from Scheimpflug studies [Dubbelman et al., 2001; Dubbelman and van der Heijde, 2001] and the parameters for the GRIN model were obtained from MRI studies [Jones et al., 2005]. The nominal refractive indices were assumed to be 1.378 (surface index) and 1.410 (nucleus index). The axial exponential decay (p_1) were chosen to be 3 (young lens), 4 (middle age lens) and 6 (old lens); and the meridional exponential decay (p_2), 2 (young lens), 4 (middle age lens) and 8 (old lens). These values represent the commonly assumed GRIN profiles of a young human lens (distributed GRIN from the nucleus to

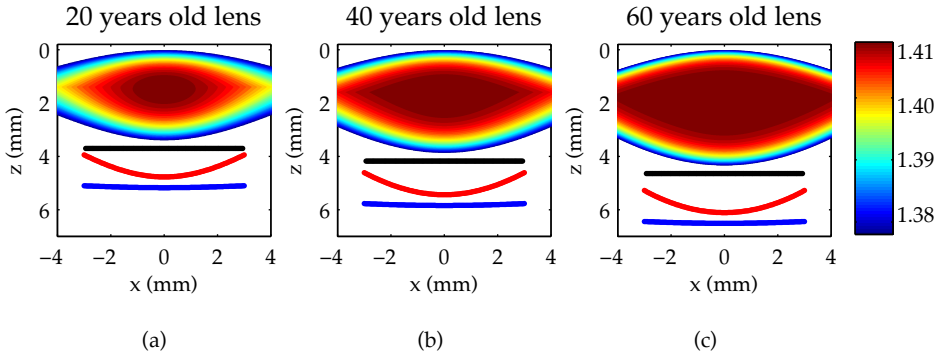

Figure 4.1: Crystalline lens GRIN tested in the simulations for a young human lens (*a*), a middle age lens (*b*) and an old human lens (*c*). The index of refraction ranged from 1.410 in the nucleus to 1.378 in the surface. The black line represents the undistorted cuvette, the red line represents the distorted posterior surface, and the blue line the distorted cuvette, for a 6 mm pupil diameter. These curves are the input data to the optimization algorithm. (Reproduced from de Castro et al. [2010], Optics Express).

the surface), and an old human lens (a large plateau and rapid index change toward the surface) [Jones et al., 2005]. Figure 4.1 presents assumed GRIN distributions for young (A), middle age (B) and old (C) human lenses used in simulations.

The optical path difference of each ray was obtained by simulating the distortion of the posterior surface of the lens and the cuvette produced by refraction and was calculated using the ray tracing algorithm (see section 2.2) over a 6 mm pupil. Gaussian noise was added to simulate inaccuracies in the detection of the surfaces from OCT in absence of other sources of experimental error. The standard deviations of the noise used in the simulations ranged from 0.1 (well below the expected experimental values) to 20 μm (much higher than the OCT resolution), with intermediate values of, 0.1, 1, 5, and 10 μm. Simulations of the GRIN reconstruction using the global search algorithm described above were performed, with 100 repetitions in each condition. The goodness of the reconstruction was assessed by comparison of the nominal and reconstructed GRIN parameters, and in terms of root mean square (RMS) of the differences between nominal and recovered GRIN in a grid of points over the lens.

4.2.4 Experimental measurements

Experimental measurements were performed on an isolated porcine lens. Enucleated porcine eyes were obtained in a local slaughterhouse, and used within 4 hours post-mortem. The lens was extracted from the cadaver eye and placed on a ring holder in a PMMA chamber filled with preservation medium (BSS plus, Alcon, Fort Worth TX, n = 1.345). The lens was aligned with the OCT system and 3-D OCT images were collected of the anterior and posterior lens surfaces, and the base of the cuvette. The lens was first imaged with the anterior surface up, and then flipped over and imaged with the posterior surface up. Also, the cuvette was imaged through the crystalline lens and through the preservation medium without passing through the lens in both cases. The whole procedure of the measurement took less than one hour, during which, the crystalline lens was continuously immersed in the preservation medium.

4.2.5 Optical Coherence Tomography system parameters

The unfolding mode of the spectral domain OCT [Grulkowski et al., 2009] was used to expand the axial range and to ensure optimal signal from both lens surfaces, two 3-D images were obtained per condition at two different focal planes and then merged using the cuvette as a reference, to produce a full 3D image of the crystalline lens. The merging algorithm was specifically developed in MatLab for this study. A single 3-D image consisted of 1668 A-scans and 70 B-scans in a lateral range of 12 x 12 mm with a resolution of 170 x 7 μm. The axial resolution of the images was 3.42 μm, and the acquisition time of a full 3-D image was 4.5 s. Figure 4.2 shows a full 3-D view of the crystalline lens acquired as described in the text.

4.2.6 Optical Coherence Tomography images processing

OCT images were corrected for fan distortion, which arises from the scanning architecture [Ortiz et al., 2009]. The fan distortion correction and posterior image analysis requires segmentation of the anterior and posterior crystalline lens surface, as well as the base of the cuvette. The detection of anterior and posterior surfaces of the crystalline lens was performed using two different strategies, according to the differences in the reflectivity of the surfaces as described in section 2.4.3.

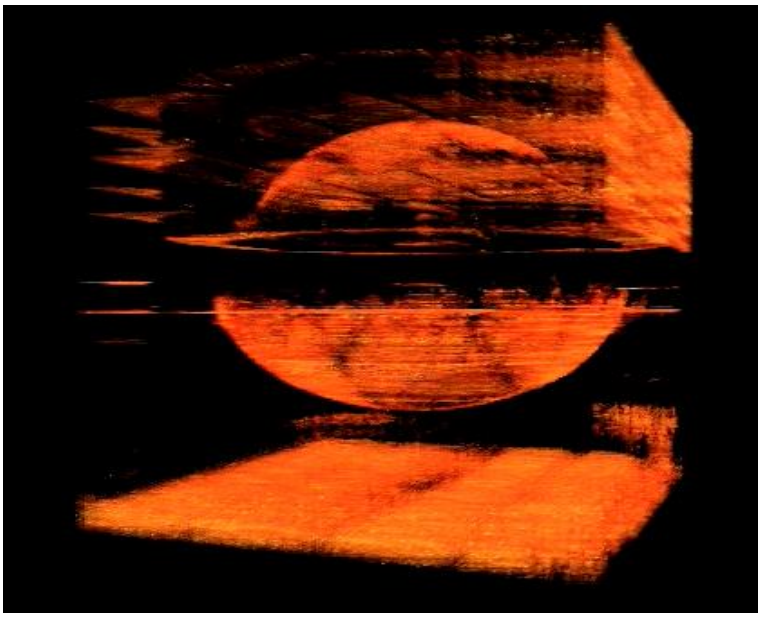

Figure 4.2: Three-dimensional image of the in vitro posterior-up crystalline lens measured with OCT. (Reproduced from de Castro et al. [2010], Optics Express).

The pair of 3-D full crystalline lens images obtained in two orientations (anterior surface and posterior surface up) was registered, to ensure that comparisons were made for the lens in an identical position. The axis of astigmatism of the entire lens (which should be the same in the two orientations of the lens) was used as a reference for alignment. The axis of astigmatism of each lens surface was computed from the Zernike fits (up to the 6^{th} order in a 6 mm diameter pupil) to each surface elevation map. The astigmatism axis of the lens was calculated from the astigmatic distortion of the image of the base of the cuvette. Using astigmatism as a signature for rotation leaves an uncertainty of 180 degrees, which is easily solved by carefully monitoring the lens handling while the lens was flipped, and by inspection of irregularities in the image that serve as landmarks. Figure 4.3 shows the data obtained from three dimensional OCT measurements of the crystalline lens placed with the anterior surface up (A) and the posterior surface up (B).

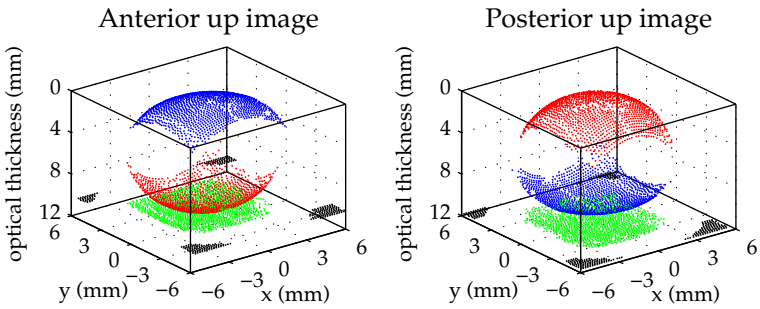

Figure 4.3: Three dimensional OCT data from images of the crystalline lens placed with the anterior surface up (left) and the posterior up (right). The blue and red points correspond to the segmented anterior and posterior surfaces of the lens, respectively. The green points correspond to the segmented cuvette surface imaged through the crystalline lens and the black points to the segmented cuvette surface seen through the preservation media without the crystalline lens. All data are fan distortion corrected, and the surfaces are also distorted due to the presence of preservation media. (Reproduced from de Castro et al. [2010], Optics Express).

4.2.7 Crystalline lens surfaces shape and thickness

The crystalline lens shape was obtained from the direct OCT images of the crystalline lens (anterior lens up and posterior lens up), i.e. not subject to optical distortion, and corrected from fan distortion. The 3-D elevation maps were fitted by Zernike polynomials up to 6^{th} order. However, as the GRIN model used is defined assuming conic surfaces, only symmetric Zernike coefficients and astigmatism were used to implement the lens surfaces in the algorithm. The crystalline lens thickness was calculated from the distortion induced on the cuvette, following Uhlhorn et al. [2008] method.

4.2.8 Three-dimensional gradient refractive index reconstruction algorithm

As the crystalline lens surfaces lacks from rotational symmetry, it was necessary to generalize the GRIN model of Eq. 4.1 to three dimensions. The generalization was made by selecting 18 meridians (from 0° to 170° in steps of 10°), and applying the optimization algorithm described before to a com-

bined merit function for all meridians. The GRIN profile of all meridians had the same values for three of the variables (surface index, nucleus index and the exponential decay in the optical axis, p_1. The exponential decay in the meridional axis, p_2, was left free, to account for the differences of the GRIN across meridians.

4.2.9 Analysis of the influence of the gradient refractive index in the optics of the lens

In order to study the influence of the GRIN distribution in the optics of the crystalline lens, aberrations of the entire lens were calculated with the experimental GRIN and with the homogeneous equivalent refractive index. The geometry of the lens was described by the Zernike fits to the raw data, as explained before. A standard computational ray tracing analysis was followed to estimate the lens aberrations. The plane of best focus was calculated searching the plane where the deviations of ray impacts (RMS) from the optical axis reached a minimum. The aberrations were calculated by fitting the optical path differences of rays (at best focus) with respect to central ray to a 6^{th} order Zernike polynomial. Calculations were done for a 6 mm pupil and 200 rays in each meridian.

4.3 Results

4.3.1 Simulations: Predicted performance of the gradient refractive index reconstruction algorithm

Figure 4.4 shows the goodness of the GRIN reconstruction in simulated crystalline lenses as a function of the amount of simulated noise in the lens surface detection. Without errors, the exact nominal parameters of the GRIN were obtained. The increase in surface detection noise increased the error in the reconstructed GRIN, as well as the standard deviation of the retrieved parameters.

The mean values and standard deviation for all the ages for a 5 μm error in the data are 0.010 ± 0.004 for the surface index, 0.003 ± 0.001 for the nucleus index and 1.4 ± 0.5 and 2.2 ± 0.5 for the exponential decay in optical and meridional axis values. As shown in Figure 5, no large differences were found in the quality of the reconstruction of the simulated lenses across ages, although for small errors, the reconstruction is worst for the surface index

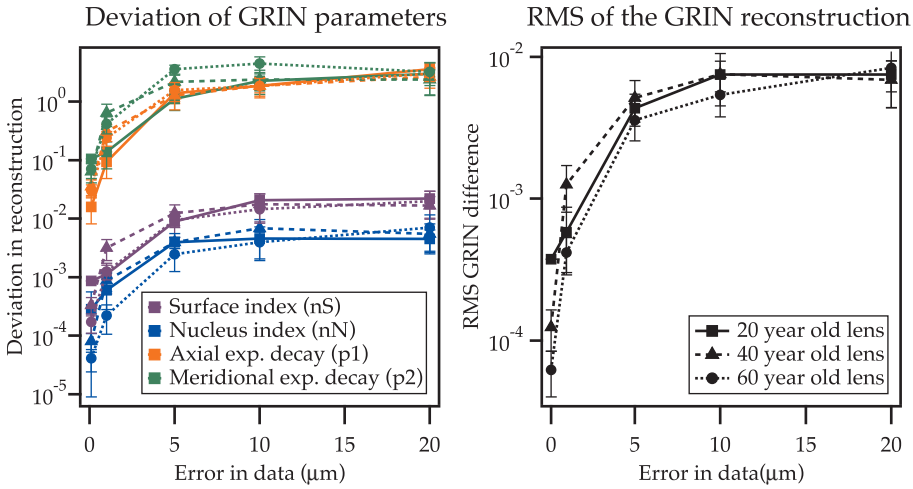

Figure 4.4: Simulations results. Deviation of the parameters resulting from optimization with different amounts of error in the detection of distorted surfaces (left) and RMS difference between reconstructed and nominal GRIN distribution (right). (Reproduced from de Castro et al. [2010], Optics Express).

and best for the nucleus index in older lenses. This is possibly due to the larger role of the nucleus in the description of the lens GRIN in old lenses in comparison to young lenses. The error in the global description of the GRIN in terms RMS of is 0.004 ± 0.001, and practically constant across ages.

4.3.2 Experimental results: Reconstruction of the gradient refractive index of a porcine crystalline lens in 3-D

The GRIN structure in the porcine lens was obtained by applying the global search algorithm, as described in section 4.2.8. The optimization search algorithm was run 5 times for the same set of data.

As said before, we assume that the results from the optimization are equivalent to the group refractive index at the central wavelength of the OCT (840 nm) with values of 1.443 in the nucleus, n_N, and 1.362 in the surface, n_S. The axial exponential decay, p_1, was 2.62, and the meridional exponential decay, p_2, varied from 3.56 to 5.18 depending on the meridian angle.

The standard deviation of these parameters across repetitions was 0.0007

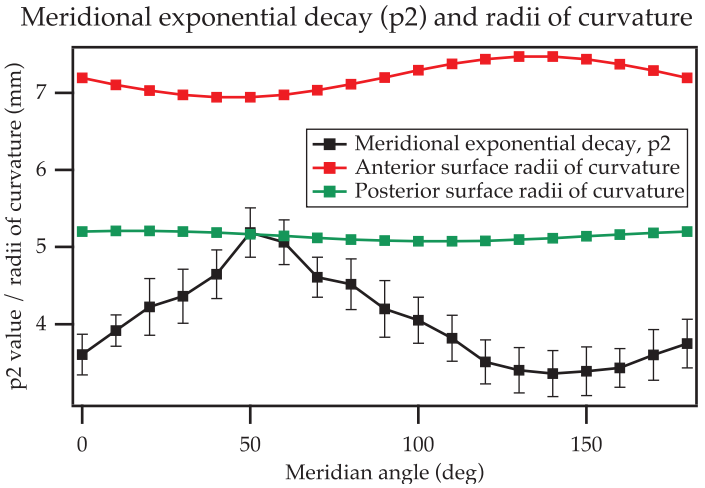

Figure 4.5: Radius of curvature of the anterior (red) and posterior (green) lens surface, in mm and meridional exponential decay parameter p_2 (black) as a function of meridional angle. (Reproduced from de Castro et al. [2010], Optics Express).

and 0.003 for the nucleus and surface index respectively, 0.09 for p_1, and 0.30 for p_2 (averaged across meridians).

The change in the meridional exponential decay p_2 is shown in figure 4.5, in comparison with the radius of curvature of the anterior and posterior lens surface, as a function of the meridional angle. Changes in these parameters across angle are indicative of astigmatism. The parameter p_2 peaks at an angle aroung 50 deg, making the gradient refractive index distribution less convergent in this meridian. The actual values of astigmatism are reported in section 4.3.3. Gradient index structure for different meridians is shown in figure 4.6.

4.3.3 Contribution of the estimated gradient refractive index to the aberrations of the crystalline lens

Figure 4.7 shows the simulated ray tracing on the measured porcine lens, for one meridian (0 deg), with the estimated GRIN (A) and with a homogeneous equivalent refractive index (B). The presence of GRIN does not affect significantly to the magnitude of the astigmatism of the crystalline lens, which changes from 0.19 D (homogeneous index) to 0.28 D (GRIN), but it shifts the

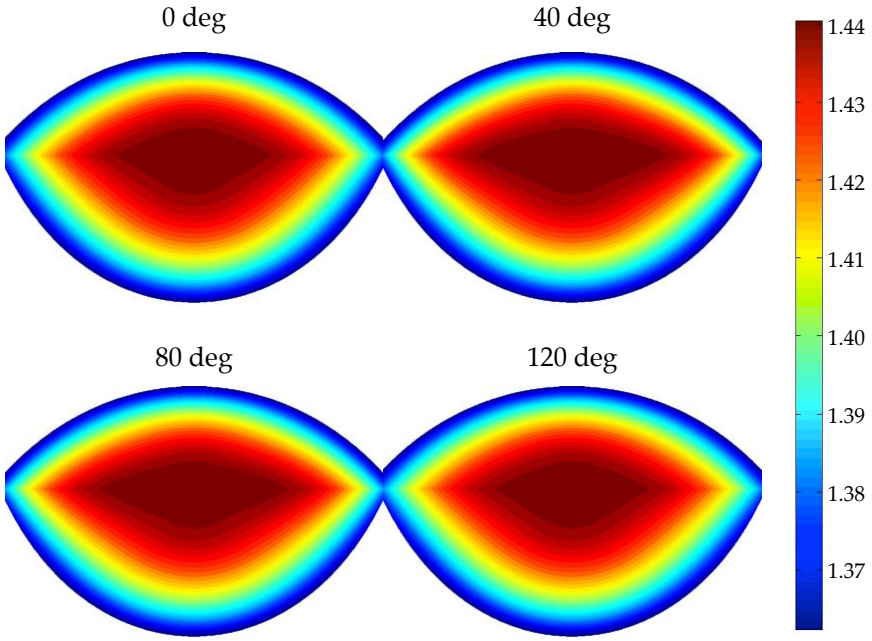

Figure 4.6: Change of the GRIN of the lens with meridian angle. Results for 4 of the 18 meridians considered.

axis of astigmatism from 35 deg (homogeneous index) to 15 deg (GRIN). The presence of GRIN has a large influence on spherical aberration, shifting the 4^{th} order spherical aberration term from positive (0.95 μm, homogeneous index) to negative values (-0.87 μm, GRIN).

4.4 Discussion

We have used the method proposed in chapter 2 to reconstruct the GRIN of the crystalline lens in vitro, using OCT imaging as input data to the global search algorithm. The method is based on the search of the best GRIN profile fitting the optical distortions produced on the posterior surface of the lens by the anterior surface and the GRIN. There are works in the literature that propose methods for compensation of the optical distortion in OCT [Zawadzki et al., 2003; Ortiz et al., 2010] assuming a homogeneous refractive index in the crystalline lens. Here, we take advantage of this distortion to reconstruct the GRIN.

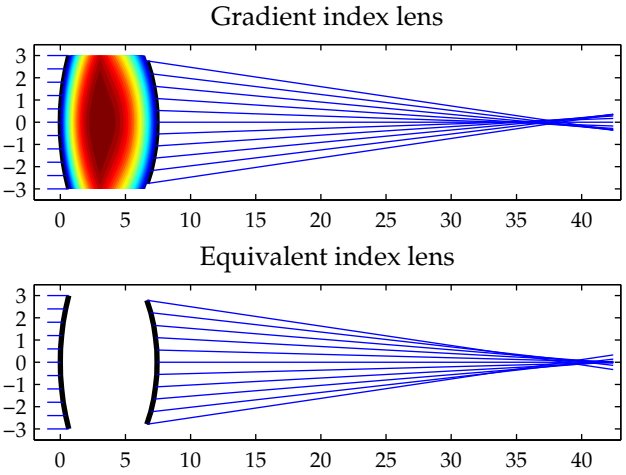

Figure 4.7: Ray tracing in one meridian for the crystalline lens with the reconstructed gradient index (A) and with the equivalent refractive index (B). The gradient refractive index affects the astigmatism of the lens (not visible here) and shifts the spherical aberration toward negative values. (Reproduced from de Castro et al. [2010], Optics Express).

Computer simulations show that, provided that the lens surfaces are known within certain accuracy, it is possible to retrieve the GRIN from the optical path difference of each ray, which is the information provided in OCT. For the detection errors and resolution of state-of-the-art OCT, we predict an accuracy in the GRIN reconstruction of 0.004 in terms of RMS of the differences. The algorithm is easily implemented in 3-D, and we have achieved, for the first time to the best of our knowledge, a 3-D reconstruction of the gradient index distribution in a porcine lens.

A critical aspect of the GRIN reconstruction is the model used to describe the index structure within the lens. We used a 4-variable GRIN model, which is sufficiently simple to allow an appropriate convergence of the optimization algorithm, while at the same time it is sufficiently flexible to accommodate differences in the variation of the refractive index from the nucleus to the surface (expected to vary strongly with age in humans) and across meridians (important in non-rotationally symmetric lenses such as the porcine lens studied). The GRIN model used is defined for a lens with biconic surfaces shapes, and therefore cannot capture all the potential complexity of surface

irregularities and refractive index inhomogeneities suggested by direct measurements of the high order aberrations in porcine crystalline lenses [Roorda and Glasser, 2004]. However, our estimates of spherical aberration of the porcine lens (from the geometrical and GRIN data) show negative values in agreement with aberrometry measurements. A 3-variable model such as Goncharov's balanced model [Goncharov and Dainty, 2007] was reconstructed with similar performance in simulations, but the lack of rotational symmetry in the crystalline lens required an additional parameter. The optimization method was not successful with polynomial GRIN models such as the Gullstrand's model, where coupling between coefficients and the high number of variables did not allow an easy relation between changes in the polynomial variables and changes in GRIN profile. To compare with previous reconstructions of GRIN on porcine crystalline lenses, the values of group refractive index at 840 nm must be converted to phase refractive index and then to the wavelength desired as was described in section 1.2.8. Despite the difference in the GRIN model and procedure, we retrieved similar values for the surface and nucleus refractive indices as those previously reported in porcine crystalline lenses by Vazquez et al. [2006] using a tomographic ray tracing algorithm in a 2-D GRIN reconstruction with a Ne-Ne at 633 nm: 1.366 and 1.444 using a mono-polynomial model and 1.361 and 1.449 for by-polynomial model, and 1.353 and 1.434 using our OCT method and genetic algorithm in a 3-D GRIN reconstruction using a 4-variable GRIN model (values converted form group refractive index at 840 nm, 1.362 and 1.443 for surface and nucleus respectively, to phase refractive index at 633 nm).

The presence of the GRIN structure in the lens has a strong impact on its optical quality. Numerous studies in the literature both in vivo and in vitro have shown that the spherical aberration in the young human and primate lens tends to be negative, compensating at least in part the positive spherical aberration of the cornea [El-Hage and Berny, 1973; Sivak and Kreuzer, 1983; Glasser and Campbell, 1998, 1999; Vilupuru and Glasser, 2001; Artal et al., 2002; Barbero et al., 2002; Roorda and Glasser, 2004; Acosta et al., 2010]. We found that the spherical aberration of the isolated lens would be positive if it had a homogeneous refractive index, while the measured GRIN structure makes the spherical aberration to be negative. This result agree with the study on refilling of porcine crystalline lenses by Wong et al. [2007] and were suggested by Vazquez [2007]. The estimated spherical aberration in the presence of GRIN (-0.87 μm) is in reasonable good agreement with reported [Roorda and Glasser, 2004] measurements on an isolated porcine lenses using

ray tracing ($-0.7\,\mu$m). By measuring the lens shape and GRIN we have been able then to identify the relative contribution of the surface shape and GRIN in the spherical aberration. As previous studies in other animals such as fish [Jagger, 1992] and rat [Campbell and Hughes, 1981], we have shown a compensatory effect of GRIN also in a more complex lens structure such as the porcine lens.

The measurement of the GRIN structure in 3-D has allowed us to evaluate the influence of GRIN in other, non-rotationally symmetric terms, such as astigmatism. In the lens studied, the presence of GRIN increase the impact of the magnitude of lens astigmatism, as it would be predicted with a homogeneous index, and also plays a role in the axis of the overall lenticular astigmatism axis.

As the method proposed requires knowledge of the posterior lens shape (as well as its distortion as it is imaged through the lens), it is suited for in vitro studies, but cannot be directly applied in vivo. However, while different optimization strategies will be needed to extract the gradient index from OCT images of the crystalline lens in vivo, knowledge of the GRIN structure in vitro have allowed to identify an anatomically plausible GRIN model and can help to limit the search of the solution space in vivo.

4.5 Conclusions

In this chapter we have tested experimentally the reconstruction method and successfully retrieved the gradient refractive index of a porcine crystalline lens three-dimensionally. Simulations with the model proposed by Manns et al. [2010] show similar accuracies as those presented in chapter 3 using the models described in Goncharov and Dainty [2007]. This validates the reconstruction method with another model and its use to estimate the refractive index of the crystalline lenses.

The three-dimensional reconstruction of the GRIN distribution show that the astigmatism of the GRIN, usually neglected in the studies of crystalline lens, may play a role in the optics of the eye. The understanding of the GRIN distribution, its contribution to the crystalline lens optics and potential changes with age are particularly relevant in humans. In the following chapter we will apply the developed techniques to human lenses

Chapter 5

Age-dependent variation of the gradient refractive index profile in human crystalline lenses

This chapter is based on the paper by de Castro et al. [2011b]: "Age-dependent variation of the Gradient Index profile in human crystalline lenses," Journal of Modern Optics 58(19-20), 1781-7, 2010.

The contribution of the author of this thesis to the study was part of the processing of experimental data, application of the search algorithms to reconstruct the GRIN and analysis of the results.

The coauthors of this study are Damian Siedlecki, David Borja, Stephen Uhlhorn, Jean Marie Parel, Fabrice Manns and Susana Marcos.

5.1 Introduction

There has been a great interest in understanding of the optical properties of the human crystalline lens over the last few decades. The primary interest of those studies address at gaining knowledge on the contribution of the crystalline lens to the overall retinal image quality [Smith et al., 2001; Artal et al., 2002], the mechanism of accommodation, and its failure in presbyopia.

One particularity of the lens is that it continuously grows throughout life. During aging, the crystalline lens undergoes several changes in several physical and biochemical properties, including geometry (thickness and curvatures), mass, volume, stiffness, elasticity and its gradient refractive index [Rosen et al., 2006; Augusteyn et al., 2008]. Age-dependent changes in the refractive index distribution were postulated by several authors based on the observations that ocular refraction remained practically constant with age, even though the lens shape experienced very significant changes [Koretz and Handelman, 1986; Pierscionek, 1990; Smith et al., 1992; Hemenger et al., 1995; Garner et al., 1998]. The lens paradox, as this effect was named, hypothesized that the equivalent refractive index should decrease with age in order to compensate for the decrease of the radii of curvature (and therefore increased surface power) of the relaxed crystalline lens with age [Koretz et al., 1997].

Experimental measurements of the gradient index distribution inside the lens and its age dependence have been challenging, and mostly restricted to measurements in vitro. For example, Pierscionek [1997] measured the local refractive indices directly using a fiber-optic sensor, and reported no significant variation of the surface index in the anterior and posterior poles with age, although she found that the index at the equator seemed to be lower in younger lenses. Using Purkinje images positions and a very simple GRIN model, Hemenger et al. [1995] reported a significantly flatter refractive index near the lens center in older than in younger lenses. Glasser and Campbell [1999] measured lens geometry in vitro, and used a laser ray tracing technique to measure the focal length from which they estimated the equivalent refractive index of the lens. They found no age-dependency of the equivalent refractive index with age. In contrast, Borja et al. [2008] reported a biphasic decline of the equivalent refractive index with age. Uhlhorn et al. [2008] used, for the first time, optical coherence tomography (OCT) for estimations of the refractive index of human crystalline lenses and reported a decrease in the average (not to be mistaken with equivalent) axial refractive

index with age. Magnetic resonance imaging (MRI) has been used as a non-destructive method to measure the GRIN distribution of the human crystalline lens, and results have been reported as a function of the age of the donor lenses [Moffat et al., 2002a; Jones et al., 2005]. These MRI results suggest that the surface and nucleus refractive index are constant with age, but that there is a flattening of the GRIN profile with age [Jones et al., 2005]. More studies using alternative methods are needed to verify the variability of the nucleus and surface refractive index values, and to confirm the changes in the shape of the profile with age.

In chapter 4 we presented the reconstruction of the GRIN distribution of a crystalline lens in vitro, based on OCT. The method was demonstrated in an isolated porcine lens, and provided for the first time three-dimensional (3D) reconstructions of a complex crystalline lens GRIN distribution. The method is based on the acquisition of OCT images of the lens (pairs of images with the anterior surface up and down), and an optimization routine based on a genetic algorithm. In the present chapter we apply the GRIN reconstruction method to the two-dimensional reconstruction of the GRIN from OCT images of human cadaver lenses of different ages.

5.2 Methods

5.2.1 Human lens samples

Human eyes were obtained from the Florida Lions Eye Bank and used in compliance with the guidelines of the Declaration of Helsinki for research involving the use of human tissue. Experiments were performed on nine lenses from nine different donor eyes within 1 to 4 days post-mortem. The donor age ranged from 6 to 72 years (average 44 ± 20 years). The donor globes arrived in sealed vials, wrapped in gauze soaked with BSS. Upon receipt, the vials were stored in a fridge at 4 °C. Before the experiment, the vials were removed from the fridge and the lens was carefully extracted and immersed in preservation medium (DMEM/F-12, D8437, Sigma, St. Louis, MO) at 25 °C, using a protocol that has been published previously [Augusteyn et al., 2006]. During measurements, the lens rested at the bottom of a cuvette on a soft rubber o-ring (Buna-N, Small Parts Inc, Miami, FL), which prevents any contact of the lens surface with the chamber wall [Uhlhorn et al., 2008]. All measurements were performed within an hour after the lens was extracted from the eye. Lenses that were swollen or damaged, as determined from

the OCT image and the methods described in Augusteyn et al. [2006], were excluded from the study.

5.2.2 Optical Coherence Tomography imaging

Lenses were imaged the custom-built time domain OCT system described in section 2.4.2 in two positions, with the anterior surface of the lens facing the OCT beam, and then in the reversed orientation (posterior surface lens up). The lens was carefully flipped and re-aligned with a surgical spoon and special care was taken to ensure that the OCT cross-sectional images were obtained on the same meridians for the two orientations of the lens, first visually and then by using features in preliminary OCT images as a guide. In practice, however, small differences in the alignment, which increase the variability of the results, are always expected.

5.2.3 Image processing

An edge-detection routine developed in MatLab was used to detect the position of the intensity peaks corresponding to the anterior and posterior surfaces of the lens on each A-scan of the uncorrected OCT image. Any residual tilt was corrected using a procedure that was described before [Urs et al., 2009, 2010].

The optical path difference (OPD) for each ray was calculated as the vertical distances between anterior and posterior lens surfaces in an uncorrected (distorted) OCT image. The actual shape of the lens was obtained from the undistorted images of the anterior and posterior surfaces. The segmented surfaces were fitted by conics. The true physical thickness of each lens was calculated from the distortion of the cuvette holding the lens during the measurements [Uhlhorn et al., 2008]. The average refractive index along the central axis was calculated dividing the optical thickness by the geometrical thickness of the lens. This calculation produces the average group refractive index for the OCT wavelength (825 ± 25 nm). The group refractive index was converted to a phase refractive index for monochromatic light at 825 nm. The phase refractive index at 589 nm was then calculated using lens dispersion data from the literature [Atchison and Smith, 2005] in a similar way as reported by Uhlhorn et al. [2008].

5.2.4 Gradient refractive index reconstruction algorithm

The GRIN profile of the lenses was estimated using the optimization method presented in chapter 2, and demonstrated in a porcine crystalline lens in chapter 4. In the previous study the method was applied on 3D OCT images of a porcine lens, while here it is applied to two-dimensional OCT images of human lenses. A merit function was built based on the difference between the experimental OPD data and the estimated OPD of each ray through a GRIN model and a genetic/Nelder–Mead algorithm searched for the best GRIN that matched the experimental optical path differences, i.e. the minimum of the merit function. The variables in the minimization procedure were those of the GRIN model.

Although the reconstruction was performed for several pupil diameters, the best results (lower values in the merit function) were found for 4 mm pupil diameters, and the reconstructed GRIN parameters are given for this pupil size.

5.2.5 Gradient refractive index model

A three-variable GRIN model was used in the reconstruction [Manns et al., 2010]. As in the case of the porcine lens study, the center of the lens was set in the meridional plane, at 0.41 times the thickness of the lens [Rosen et al., 2006]. The GRIN was described by means of a power coefficient from the nucleus (with a refractive index n_N) to the surface (with refractive index n_S):

$$\mathrm{n}(\mathrm{r}, \theta) = n_N - \Delta\mathrm{n} \cdot \left(\frac{\rho}{\rho_\mathrm{S}} \right)^p, \tag{5.1}$$

where Δn is the difference between nucleus and surface refractive indices, ρ is the distance from the center of the lens to the surface at angle θ, and p is the power coefficient of the GRIN.

A similar model (with additional variables to account for meridional variations in the refractive index) had been successfully used to reconstruct the GRIN 3D distribution in the porcine lens. The power coefficient allows the description of highly distributed refractive index (low exponents) as expected in young lenses, as well as a constant plateau and rapid decline of the refractive index toward the surface (high exponents) as expected in old lenses. The only constraint used in the search algorithm was a penalty if the surface refractive index was higher than the nucleus index.

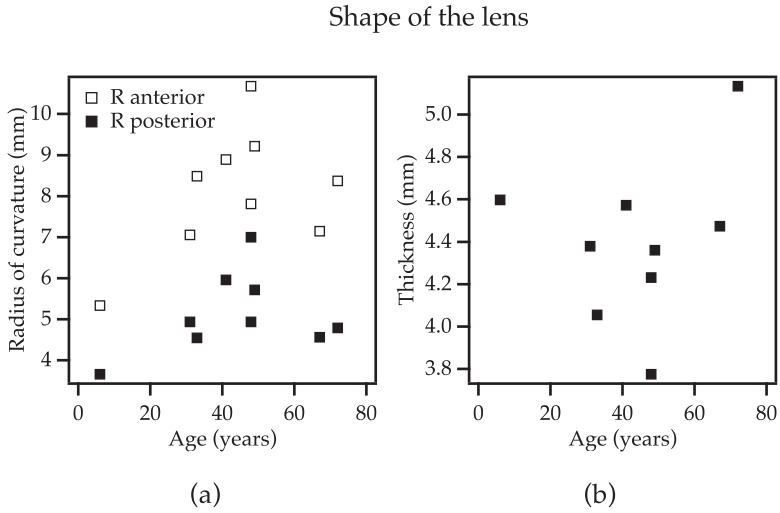

Figure 5.1: (*a*) Radii of curvature of the anterior and posterior surfaces of the lenses used in this study. (*b*) Thickness calculated from the OCT images. (Reproduced from de Castro et al. [2011b], Journal of Modern Optics).

5.3 Results

5.3.1 Lens surface shape and thickness

Anterior and posterior lens surfaces were fitted by conics over a 6 mm area. Fitting errors were in all cases in the order of the OCT resolution. Figure 5.1 shows the values of anterior and posterior radii of curvature and thickness as a function of age. Lenses steepened with age until at least 50 years.

5.3.2 Average refractive index

The average refractive index is the mean value of the GRIN profile along the optical axis of the lens. Figure 5.2 shows the average phase refractive index as a function of age at 589 nm. As reported previously in the literature [Uhlhorn et al., 2008], there is no clear age-related trend, and there is a wide range of average index values (1.392 to 1.425) for the 9 lenses measured in this study. The two extreme values for the adult eyes (at 31 and 49 years) could be caused by variability in the measurement due to positioning errors.

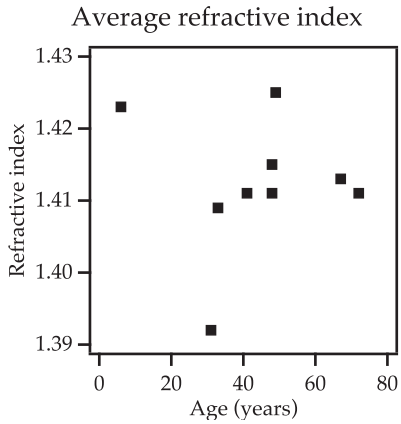

Figure 5.2: Average phase refractive index at 589 nm as a function of age. (Reproduced from de Castro et al. [2011b], Journal of Modern Optics).

5.3.3 Gradient refractive index

Table 5.1 shows the GRIN model parameters obtained in the reconstruction, and Figure 5.3 the age-dependence of the three parameters: nucleus and surface indices (Figure 5.3*a*) and power coefficient (Figure 5.3*b*).

The only systematic variation with age was found for the power coefficient. The goodness of the reconstruction (comparison of the experimental distorted posterior lens surface and the simulated from the reconstructed GRIN) was less than 15 μm in all cases.

In four lenses (ages 31, 33, 41 and 49) the lowest RMS was found with a homogeneous refractive index (similar nucleus and surface indices). A study of the space of solutions revealed another pair of values that represented the experimental OPDs with high accuracy (RMS = 6 ± 5 μm). For these lenses, another realization of the local search algorithm produced a local minimum, which was taken as the solution of the optimization problem.

There was no statistically significant change with age in the refractive index of surface and nucleus ($p = 0.37$ and 0.39, respectively). Average refractive index values in surface and nucleus was found to be 1.373 ± 0.014 and 1.417 ± 0.011. The power coefficient increased steadily with age and significantly ($p = 0.039$), with a rate given by 0.24 ± 0.05 ($r = 0.847$) per year. All values correspond to the phase index at 589 nm.

Figure 5.4 shows raw OCT images and the 2-D representations of the

Table 5.1: Values of average refractive index and GRIN parameters: surface and nucleus refractive index and power coefficient for the set of lenses imaged in this study. An asterisk in the age column indicates that a secondary minimum was taken as solution. All refractive index values correspond to the phase refractive index calculated at 589 nm.

Age	Average	GRIN results		
(years)	(phase 598 nm)	Surface	Nucleus	Exp decay
6	1.423	1.386	1.434	3.2
*31	1.392	1.362	1.399	2.6
*33	1.409	1.388	1.414	7.6
*41	1.411	1.387	1.418	4.4
48	1.411	1.351	1.412	11.9
48	1.415	1.356	1.418	13.6
*49	1.425	1.382	1.432	6.5
67	1.413	1.365	1.412	17.7
72	1.411	1.376	1.413	16.7

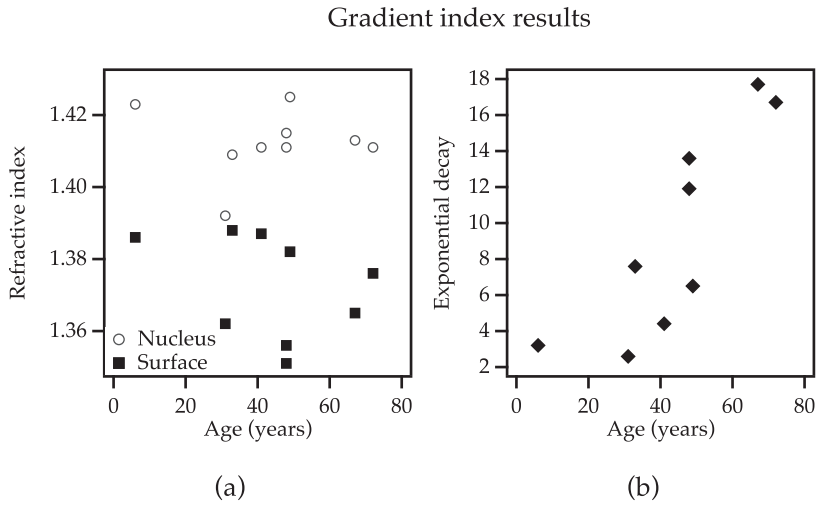

Figure 5.3: Nucleus and surface refractive indices (*a*) and power coefficient (*b*). The refractive index values correspond to the phase refractive index at 589 nm. (Reproduced from de Castro et al. [2011b], Journal of Modern Optics).

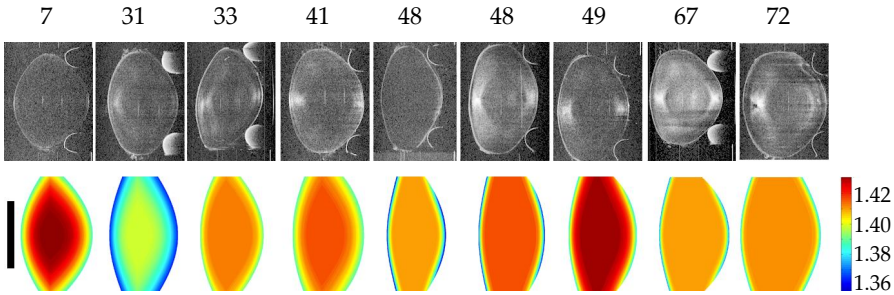

Figure 5.4: Two-dimensional OCT image (upper row) and reconstructed GRIN distribution (lower row) of the nine lenses of different ages the study. Data of the central 4 mm pupil were used, the vertical black bar indicates the area reconstructed. (Reproduced from de Castro et al. [2011b], Journal of Modern Optics).

reconstructed GRIN in the nine lenses of the study.

5.4 Discussion

We have shown that OCT imaging allows high-resolution imaging of the crystalline lens surfaces as well as reconstruction of the GRIN distribution of the isolated human lens. In a small group of eyes, we found age-dependent variation of the lens shape, and changes in the shape of the GRIN profile.

We found similar changes in the radii of curvature to those reported by Borja et al. [2008] in isolated lenses using shadowphotography. The changes are more prominent in the anterior surface, as previously reported to occur in vivo as a function of age and as a function of accommodation [Koretz et al., 2002; Dubbelman et al., 2005a; Rosales et al., 2008]. A remarkable feature is the biphasic pattern of the variation of the lens radii with age [Borja et al., 2008].

We found that the surface and nuclear refractive indices were constant with age. However, the values suffered from a relatively large scatter. A larger number of samples may confirm with statistical certainty if these indices change with age. The lack of systematic variation of the surface and nucleus indices with age had been previously reported using destructive methods [Pierscionek, 1997] and with the MRI approach [Jones et al., 2005] on a larger population. The shape of the GRIN profile varied significantly

with age, with a more distributed index in the young lens, and an increase of the central plateau with increasing age, confirming results obtained from a Purkinje method [Hemenger et al., 1995] and MRI [Moffat et al., 2002a; Jones et al., 2005]. The average refractive index agrees with previously published results [Uhlhorn et al., 2008], the range of refractive indices (1.392 to 1.425) is similar to previous reports (1.316 to 1.416), and the scattering of the data is large in all studies. The reconstructed surface and nucleus indices of refraction also show a large inter-subject variability. The variability of the surface and nucleus indices is probably not the reflection of the true biological variability, but caused by measurement uncertainties. A precision of ± 0.01 in the refractive index correspond to a relative error of less than 1%. In general, the lens refractive index is derived indirectly from several independent measurements, each with its own sources of error. Small measurement errors can produce significant variations of the refractive index. In this study, the refractive index is calculated from two separate images of the crystalline lens. The extreme values of two of the adult lenses could be due to small positioning errors between the two measurements (see below). Overall, our reconstructed indices (1.351 to 1.388 for the surface refractive index and 1.399 to 1.434 for the nucleus refractive index) are in agreement with those from Jones et al. [2005] using MRI (1.36 and 1.38 for the surface refractive index and 1.395 to 1.430 for the nucleus refractive index).

The only parameter that is found to change systematically with age is the power coefficient of the GRIN model. Some studies in the literature describe the progressive development of a central refractive index plateau area in the lens with aging [Hemenger et al., 1995; Jones et al., 2005]. The three-variable model can account for a gradual variation of the profile (low power coefficients) or the presence of a plateau (high power coefficients), without requiring a highly complex GRIN model definition. We found that the power coefficient increases steadily with age. This is consistent with a monotonic variation of the profiles in young lenses, and a relatively flat profile, with a steep decrease of the index near the surface in old lenses. These results are in accordance with previous literature using MRI of the change of the GRIN structure in crystalline lenses with age [Jones et al., 2005].

The use of OCT imaging to reconstruct GRIN in the human lens is novel. We had theoretically suggested that optical path differences from OCT contained information of the GRIN distribution [Ortiz et al., 2004]. The first experimental application of OCT to retrieve GRIN was performed in the fish lens (using a simple spherical lens and spherical GRIN model) by Verma et al.

[2007]. The difference between the distorted and undistorted lens shape is a key factor in the reconstruction. The OCT technique provides high resolution in surface shape measurements (in comparison with shadow photography, Scheimpflug of MRI) and GRIN estimates. The precision of the GRIN reconstruction technique is mainly limited by experimental errors. Lens surface elevation is limited by the resolution of the OCT system (around 10 μm in our system) and the centering of the lens. Tilt is corrected in the images but residual tilt, and particularly a decentration of the lens (i.e. A-scan not passing through the apex of the lens) will result in an underestimation of the thicknesses and overestimation of the radii of curvature. Also, although special care was taken to ensure that, when flipping the lens over, the meridian under measurement remained unchanged, errors may arise due to decentration or rotation. If rotated, astigmatism in the surfaces or possible asymmetries in the GRIN distribution will introduce an error in the measurements. While we believe that these effects are not significantly affecting the overall findings, they increase the variability. In particular, potential trends for variations in the surface and nucleus index can be confirmed by increasing the sample size. Also, some of the errors can be minimized by extending the method to 3-D images of the lens. Future 3-D reconstruction will also make it possible to take into account the possible astigmatism of the lens surfaces and meridional variations in the GRIN profile.

5.5 Conclusion

The reconstruction of the GRIN of in vitro human lenses using optimization techniques is novel. Particularly we have shown that the OCT images contain enough information to study the GRIN of the crystalline lenses. The method and technique proposed in this thesis was first demonstrated in a porcine lens and now proved also robust in human lenses of different ages.

The variation of the profile in aging human lenses is consistent with MRI measurements and the formation of a refractive index plateau. This is addressed in our study, using optical techniques and relatively simple experimental equipment compared with MRI studies.

The distortion introduced in the posterior surface by the GRIN distribution of the crystalline lens was used as input data to reconstruct the refractive index of the lens. Conversely, the GRIN distorts the image of the posterior lens surface in OCT imaging. The effect of GRIN on the estimation of the

posterior lens shape parameters and the correction of this distortions will be addressed in chapters 6 and 7.

Chapter 6

Distortions of the posterior surface in optical coherence tomography images of the isolated crystalline lens: effect of the lens gradient refractive index

This chapter is based in the paper by Borja et al. [2010]: "Distortion of the posterior surface in optical coherence tomography images of the isolated crystalline lens: effect of the lens index gradient," Biomedical Optics Express 1(5):1331-40, 2010.

The contribution of the author of this thesis was the programming of the algorithms to simulate the distortions produced when the lens is imaged with an Optical Coherence Tomography system, the comparison between the distorted and the measured surfaces, and the correction of the distorted surfaces supposing a homogeneous or a graded index media in the lens.

The coauthors of this study are David Borja, Damian Siedlecki, Stephen Uhlhorn, Sergio Ortiz, Esdras Arrieta, Jean Marie Parel, Susana Marcos and Fabrice Manns.

6.1 Introduction

Since the gradient index (GRIN) contributes significantly to both paraxial and optical properties and higher-order aberrations of the lens [Sands, 1970; Smith et al., 2008], it affects the distortion of the images of the crystalline lens acquired in vivo or in vitro using Scheimpflug imaging [Dubbelman and van der Heijde, 2001; Rosales et al., 2006; Rosales and Marcos, 2009], or Optical Coherence Tomography (OCT) [Verma et al., 2007; Uhlhorn et al., 2008]. In images acquired in vivo, the shape of the anterior lens surface is distorted due to refraction at the cornea [Rosales et al., 2006; Dunne et al., 2007]. Additionally, in images acquired in vivo or in vitro, the shapes of the posterior lens surface and internal boundaries are distorted due to refraction at the anterior lens surface, and internally through the refractive gradient index.

Several correction algorithms, generally relying on a ray trace through the ocular surface and media, have been developed to correct for refractive distortions of the cornea or lens in Scheimpflug imaging [Dubbelman and van der Heijde, 2001], and OCT [Westphal et al., 2002; Podoleanu et al., 2004]. Three-dimensional correction algorithms have been developed only very recently [Ortiz et al., 2010]. One of the limitations of these correction algorithms is that they rely on ray traces in homogeneous media. Correction algorithms for the crystalline lens assume that the lens is homogeneous, with a fixed refractive index equal to the equivalent index [Dubbelman and van der Heijde, 2001; Ortiz et al., 2010]. Differences in the ray path between the real crystalline lens with its gradient refractive index and the uniform equivalent refractive index, introduce uncertainties in the shape of the internal boundaries and posterior surface produced by the correction algorithms.

The purpose of this chapter is to quantify the measurement error introduced in the posterior lens surface of OCT images of the in vitro lens due to refraction at the anterior lens surface and through the GRIN of the lens. Implications for the correction of OCT images of the crystalline lens are discussed.

6.2 Material and methods

6.2.1 General description

Cross-sectional OCT images of isolated human crystalline lenses were acquired with the time domain OCT system described in section 2.4.2. The lens was first imaged with the OCT scanning beam incident on the anterior lens surface ("anterior up" image) and then flipped over and imaged with the OCT scanning beam incident on the posterior lens surface ("posterior up" image). As said before, in the "anterior up" images the posterior lens surface is distorted due to refraction at the anterior lens surface and due to the index gradient. The "posterior up" image provides the undistorted shape of the posterior lens surface. The effect of the GRIN on the posterior shape of the lens is quantified by comparing the radius of curvature and asphericity of the posterior lens surface obtained from the "anterior up" and "posterior up" images. The results were also compared with the predictions from an optical model of the lens with refractive index gradient.

6.2.2 Donor tissue preparation

All human eyes were obtained and used in compliance with the guidelines of the Declaration of Helsinki for research involving the use of human tissue. Experiments were performed on 12 lenses from 12 different donor eyes within 1 to 4 days post-mortem (average: 57 ± 25 hours). The donor age ranged from 6 to 90 years (average 47 ± 22 years). The lenses were isolated from the eye and immediately immersed in a small chamber filled with preservation medium [Augusteyn et al., 2006]. The lens rests at the bottom of the chamber on a soft rubber o-ring which prevents any contact of the lens surface with the chamber wall [Uhlhorn et al., 2008].

6.2.3 Image acquisition

The time-domain OCT system described in section 2.4.2 [Uhlhorn et al., 2008], was used to acquire cross-sectional images of the whole crystalline lens. The axial and lateral position of the lens was first adjusted using a continuous real-time display of the central A-scan as a guide, until the lens was centered (maximum signal strength and maximum separation between the lens anterior and posterior signal peaks). Tilt and tip were then adjusted using real-time B-scan images for guidance.

Once the lens was centered and aligned, a cross-sectional OCT image was acquired first with the lens resting on its posterior surface and with the anterior surface facing the OCT beam, "anterior up". The lens was then carefully flipped with a surgical spoon, re-aligned, and a cross-sectional OCT image is acquired with the lens resting on its anterior surface and with the posterior surface facing the OCT beam, "posterior up". Each cross-sectional OCT image consists of 500 A-lines acquired over a 10 mm lateral scan length with 5000 points per A-line.

6.2.4 Optical Coherence Tomography image analysis

An edge-detection program developed in MatLab was used to detect the position of the intensity peaks corresponding to the anterior and posterior surfaces of the lens on each A-line of the uncorrected OCT image. Any residual tilt was then corrected using a procedure described by Urs et al. [2010]. Along each A-line of the processed image, the position of the intensity peaks is determined by the optical path length traveled between the boundaries of interest by a ray entering the measurement chamber in a direction parallel to the optical axis. With the coordinate system and notation of figure 6.1, the uncorrected positions of the first and second surfaces are therefore calculated using:

$$z_1(x) = \frac{d_1(x)}{n_{DMEM}} \qquad z_2(x) = z_1(x) + \frac{d_2(x) - d_1(x)}{n_L(x)} \tag{6.1}$$

In Eq. 6.1, $n_{DMEM} = 1.345$ is the group refractive index of DMEM and $n_L(x)$ is the average value of the group refractive index of the lens along the ray path, both measured at the central wavelength of the OCT beam ($\lambda = 825\,nm$). The average group refractive index of the lens was measured directly using Uhlhorn's method [Uhlhorn et al., 2008]. The lengths $d_1(x)$ and $d_2(x)$ correspond to the optical distances and the lengths $z_1(x)$ and $z_2(x)$ correspond to the actual distances along the ray. The curve $z_1(x)$ is the corrected shape of the first lens surface. The curve $z_2(x)$ is the shape of the second lens surface corrected for the refractive index but not for refraction at the first lens surface or within the lens. In the "anterior up" images, the first surface is the anterior lens surface. In the "posterior up" images, the first surface is the posterior lens surface. The cross-sectional profiles, $z_1(x)$ and $z_2(x)$, were fitted with conic functions over the central 6 mm zone to calculate the radius of curvatures (R) and asphericity (Q) of both lens surfaces [Manns et al., 2004; Rosen et al., 2006].

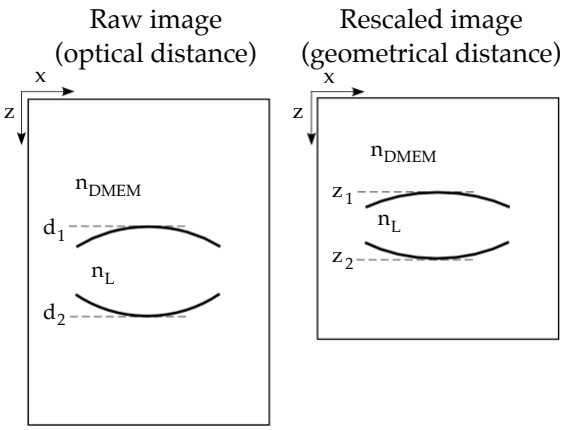

Figure 6.1: Optical and geometric location of the lens surfaces in OCT images. Left: Raw image. Right: Image corrected for the refractive index using Eq. 6.1. (Reproduced from Borja et al. [2010], Biomedical Optics Express).

To evaluate the measurement repeatability, one lens (age = 6 years) was imaged three times in the anterior up position. The standard deviation was 0.07 mm (± 3.5% of the mean) for the anterior radius of curvature and 0.48 mm (± 13% of the mean) for the posterior surface. A separate analysis shows that this measurement variability is due almost entirely to variability in the lens position between successive measurements, not to the processing algorithm.

6.2.5 Simulations

Effect of the GRIN on distortions

In a first set of simulations, the posterior surface distortions predicted using an exact ray-trace through a homogeneous and GRIN model of the lens were compared with the experimental results. The measured posterior lens surface radius and asphericity obtained from anterior-up images were compared with values obtained from conic fits of the simulated posterior surface. For the homogenous model, simulations were run with two different values of the index: the "average" index and the "best" index. The average refractive index define above was obtained by dividing the optical path length in the center of the lens by the actual central lens thickness obtained from

shadow photography images of the same lens [Rosen et al., 2006; Borja et al., 2008]. The best index is the homogeneous index that minimizes the RMS error between the measured and simulated posterior lens surface as imaged through the anterior surface. For the GRIN model, we assumed a gradient index distribution based on the three-variable model proposed by Goncharov and Dainty [2007]. This model was used in the simulations of chapter 3. The model assumes fixed values for the index of refraction in the core (n_N) and the surface (n_S) of the lens, and a radius for the posterior isoindicial surface profile (r_{pp}) which does not coincide with the radius of the posterior surface.

We performed calculations for a lens from a 6 year old donor using the undistorted lens surface parameters obtained from the anterior and posterior surface up measurements as the nominal values. The measured average index was 1.419. The gradient index parameters were obtained using the reconstruction methods described before with optical path differences as input data. This produced the following values: $n_S = 1.374$; $n_N = 1.443$; $r_{pp} = -3.526$ mm. Given the potential interactions between radius of curvature and asphericity [Pérez-Escudero et al., 2010], the differences between the nominal (measured) and simulated surfaces are given in terms of the RMS difference of their elevation. A summary of this simulation is illustrated in the top panel of figure 6.2 (Simulation 1).

Effect of the GRIN on distortion correction

A second set of simulations was designed to provide an estimate of the relative contribution of surface refraction and gradient index to the optical distortion, figure 6.2 (Simulation 2). In these simulations, the shape of the undistorted measured posterior lens surface obtained directly from posterior-up images was compared with the shape obtained from anterior-up images after correction using two different methods. In the first method, the distortion is corrected by division by a constant homogeneous index of refraction, as in Eq. 6.1. In the second method, the distortion is corrected using an exact ray-trace assuming both homogeneous and GRIN models, using the same parameters as above. Optical distortion correction in OCT has been described in detail previously for the cornea and lens, and validated using artificial eye models, but the methods were presented only for homogeneous indices of refraction [Westphal et al., 2002; Ortiz et al., 2010]. For the posterior surface reconstruction from OCT in the presence of GRIN we have developed here an iterative procedure, which assumes knowledge

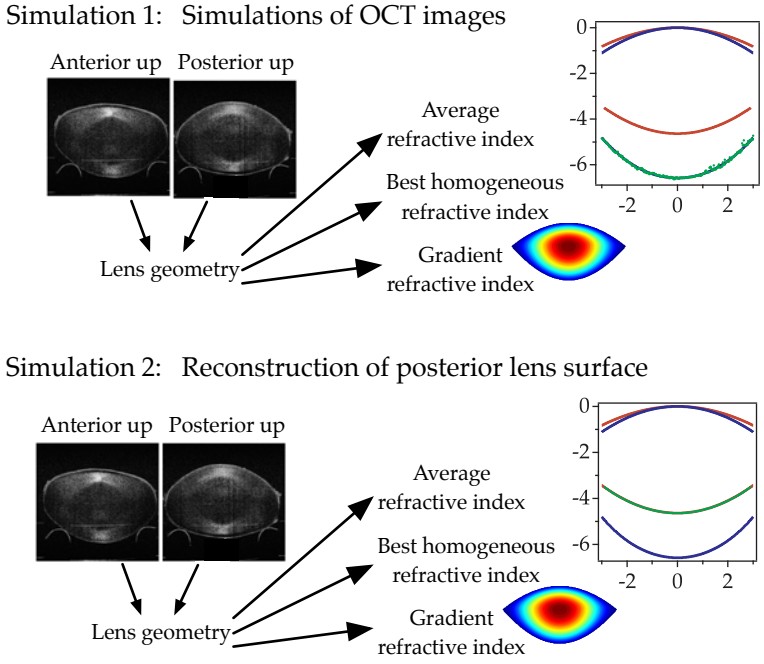

Figure 6.2: Schematic diagram of the methods used in the simulations. In Simulation 1 (upper panel) the posterior surface of the lens obtained with OCT is simulated and compared to the measured distorted posterior lens surface, assuming knowledge of the anterior surface (obtained from OCT) and either the measured average refractive index, the best homogeneous index (producing best match with experimental data) and a GRIN distribution in the lens. The figure on the upper right shows the actual lens shape in red, the measured surface in blue and an example of the simulated distorted posterior surface in green. In simulation 2 (lower panel) distortion correction algorithms are applied to reconstruct the posterior lens shape. The reconstructed shape is compared to the actual geometry obtained by OCT imaging of the flipped-over lens. The algorithm is applied for a homogeneous refractive index and GRIN. The figure in the lower right panel shows the actual lens shape in red, the distorted lens shape in blue, and the reconstructed posterior lens shape in green. (Reproduced from Borja et al. [2010], Biomedical Optics Express).

of the anterior surface shape and the general GRIN distribution, and the posterior surface shape obtained by the simple division by the refractive index method as a starting estimate. The method applies Sharma's algorithm for ray tracing in the GRIN structure [Sharma et al., 1982], and calculates the points that match the optical path measured directly from OCT images, in order to estimate the posterior lens surface in the next iteration. The surface parameters and thickness produce a change in the GRIN distribution in each iteration. The algorithm convergence criterion is established at a difference less than 0.1 μm between the fitting radii of curvature in two successive iterations. The procedure converges rapidly, within in a few iterations. The method will be described and studied in detail in the next chapter of this thesis.

6.3 Results

6.3.1 Experimental results

The imaging experiments were successful in all 9 eyes. In 2 eyes, the average group refractive index could not be measured directly. In these two eyes, the index was estimated by using the regression equation as a function of age provided by Uhlhorn et al [Uhlhorn et al., 2008]. Illustrative examples of raw and corrected anterior-up OCT and posterior-up OCT of the same lens are shown in figure 6.3. Conic section fits provided an accurate description of the central lens profile in all lenses. A Bland-Altman analysis comparing the anterior-up (undistorted) and posterior-up (distorted) measurements of the anterior surface shows that the mean difference (± 95% confidence interval) between the distorted and undistorted shape is 0.20 ± 0.93 mm for the radius of curvature and 0.642 ± 6.153 for the asphericity (figure 6.4). A similar analysis for the posterior radius produces values of 0.12 ± 0.73 mm for the radius of curvature and -0.182 ± 1.940 for the asphericity (figure 6.5). Overall the analysis shows that the distorted surface overestimates the true radius of curvature and asphericity. With an error that is within the reproducibility of the measurement.

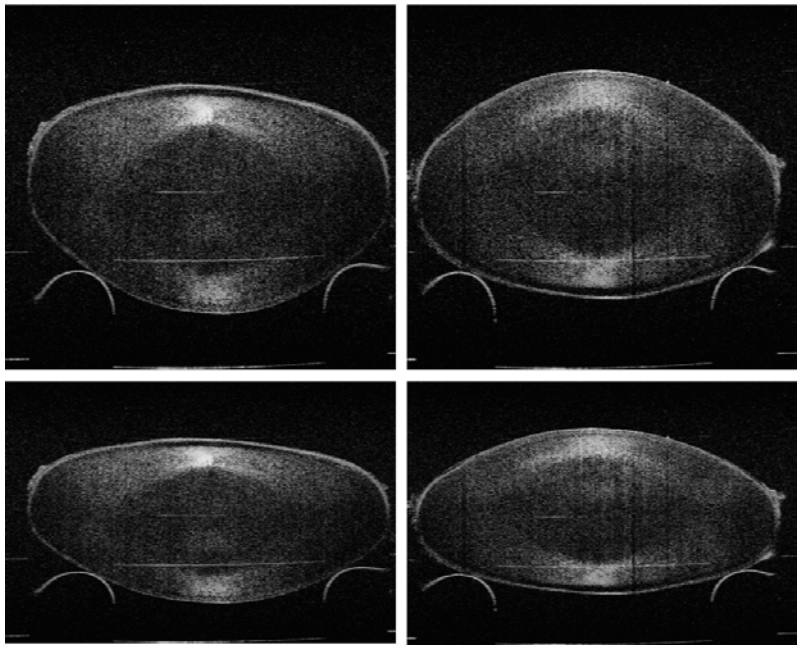

Figure 6.3: Raw (top) and rescaled (bottom) OCT images of a 49 year old human crystalline. Left: Anterior-up OCT image; Right: Posterior-up OCT image. Tilt errors are corrected during post-processing before calculating the radius of curvature and asphericity. (Reproduced from Borja et al. [2010], Biomedical Optics Express).

6.3.2 Simulation of the distortion of the Optical Coherence Tomography images

We found a substantially good correspondence between the experimental and the simulated OCT images, with the difference between the simulated and measured distorted posterior surfaces being much lower when refraction from the anterior surface and GRIN is considered. Table 6.1 shows the fitted parameters (radius of curvature and asphericity) of the measured and simulated distorted posterior surface when imaged through the lens, and the RMS difference between the nominal and simulated surfaces, with the three different models to distort the image (average refractive index (1.419); best result for a homogeneous index (1.417); and GRIN model ($n_N = 1.443$,

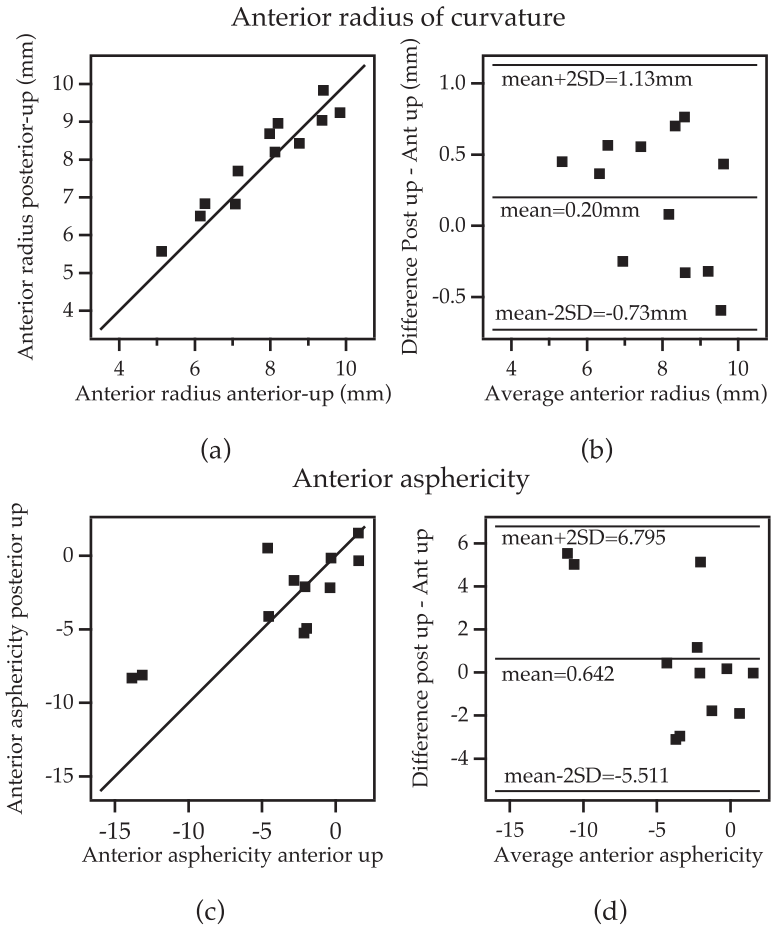

Figure 6.4: Bland-Altman analysis of the distorted versus undistorted anterior surface. Top graphs: Radius of curvature; Bottom graphs: Asphericity. The graphs on the left show the distorted parameter (vertical axis) versus the undistorted parameter (horizontal axis). The diagonal is the 1:1 line (perfect correlation). The graphs on the right show for each lens the difference between the distorted and undistorted parameters for each eye versus the average of the two values (mean difference plots). The central horizontal line corresponds to the mean difference. The top and bottom lines correspond to the 95% confidence intervals (± 2SD from the mean). (Reproduced from Borja et al. [2010], Biomedical Optics Express).

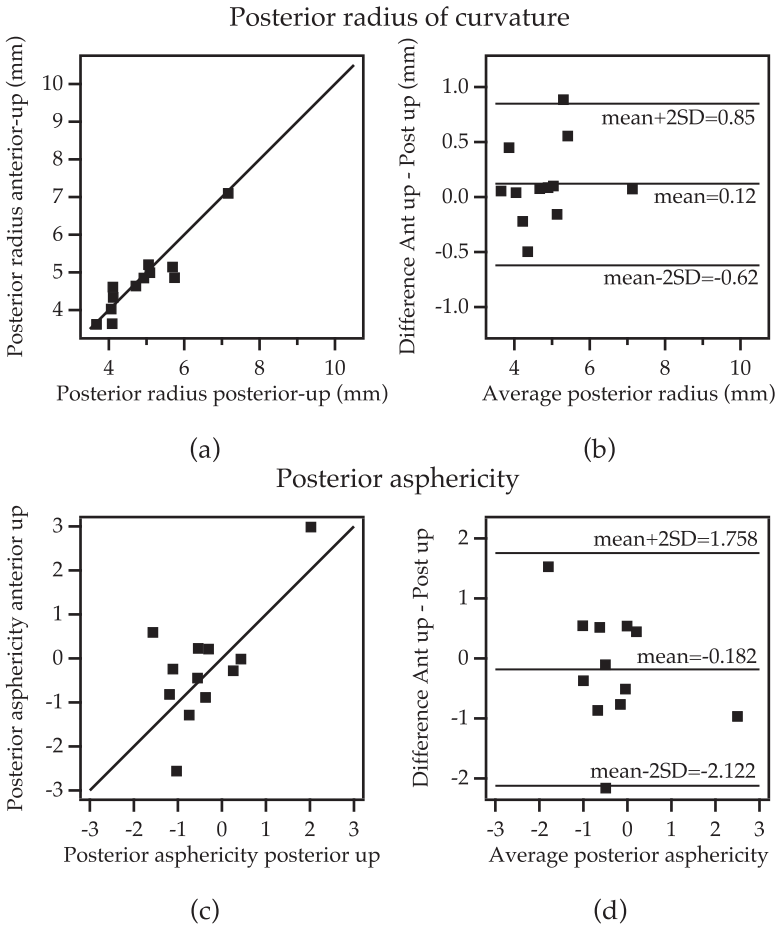

Figure 6.5: Bland-Altman analysis of the distorted versus undistorted posterior surface. Top graphs: Radius of curvature; Bottom graphs: Asphericity. The graphs on the left show the distorted parameter (vertical axis) versus the undistorted parameter (horizontal axis). The diagonal is the 1:1 line (perfect correlation). The graphs on the right show for each lens the difference between the distorted and undistorted parameters for each eye versus the average of the two values (mean difference plots). The central horizontal line corresponds to the mean difference. The top and bottom lines correspond to the 95% confidence intervals (± 2SD from the mean). (Reproduced from Borja et al. [2010], Biomedical Optics Express).

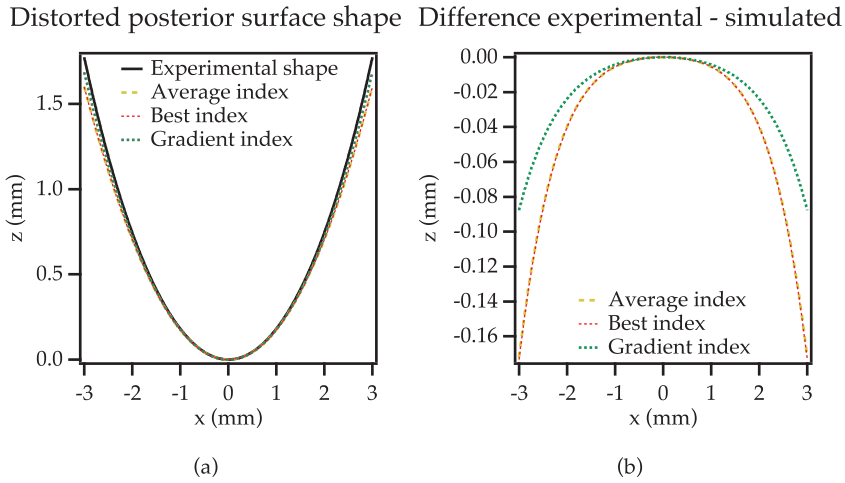

Figure 6.6: Simulations result for a lens from a 6 year old donor. (a) Comparison of the actual measured distorted posterior lens contour (experimental shape, in green) with the posterior contour simulated using the three different refractive index models. (b) Difference between experimental and simulated distorted posterior surfaces. Average and best homogeneous refractive index are hardly distinguishable. The best agreement with the experimental shape is found for the GRIN model. (Reproduced from Borja et al. [2010], Biomedical Optics Express).

$n_S = 1.374$, $r_{pp} = -3.526\,\text{mm}$)). The best prediction of the distorted surface is obtained when using the GRIN structure. The difference is particularly important in the asphericity of the surface. Figure 6.6 shows the comparison of the shapes of the simulated distorted surfaces.

6.3.3 Optical Coherence Tomography distortion correction analysis

In the previous simulations, we estimated how the posterior lens would appear through the lens in an OCT image, and demonstrated that the best prediction of the distorted surface (in comparison with the real distorted surface) is obtained when a GRIN structure is assumed. Different optical distortion correction methods for retrieval of the posterior lens surface through the anterior lens in OCT were investigated as well and retrieved

Table 6.1: Measured and simulated distorted posterior surface parameters.

		homogeneous index		
	measured	average	best	GRIN
Posterior lens radius (mm)	2.792	2.858	2.858	2.852
Posterior lens asphericity	0.289	0.063	0.060	0.219
RMS surface difference (mm)	n.a.	0.026	0.024	0.006

Table 6.2: Nominal and reconstructed posterior surface parameters. Assuming a refractive index of 1.373 for the lens surface and 1.336 for aqueous, the posterior surface powers are 10.1 D (nominal), 9.0 D (average index), 10.1 D (homogeneous index), 10.3 D (GRIN).

			optical distortion correction	
	nominal	division by average index	homogeneous index	GRIN
Posterior lens radius (mm)	3.662	4.120	3.672	3.586
Posterior lens asphericity	-0.135	0.652	0.362	0.034
RMS surface difference (mm)	n.a.	0.023	0.018	0.006

surface parameters were compared to their nominal values. The different OCT processing methods include: (*1*) simple division of OCT optical paths by an homogeneous index of refraction; (*2*) refraction by anterior lens surface, assuming a homogeneous index of refraction model for the lens; and (*3*) refraction by anterior lens surface and gradient refractive index distribution of the lens, assuming the GRIN model described above. The corrective iterative method using GRIN provided the most accurate results (Table 6.2).

The simple division by the value of the average refractive index produced a discrepancy of 0.46 mm (12.5%) in the radius of curvature and 0.79 in

the asphericity. The incorporation of optical distortion correction methods (refraction by the anterior surface) assuming a homogeneous lens with the average refractive index produced a discrepancy of 0.010 mm (0.27%) in the radius of curvature and 0.49 in the asphericity. The correction of refraction from the anterior lens surface assuming a GRIN distribution produced the smallest overall discrepancy: 0.08 mm (2.1%), in the radius of curvature, 0.17 in the asphericity and 0.006 mm in the RMS surface difference.

6.4 Discussion

Our experimental results show that the distortion due to refraction at the anterior surface and within the gradient produces an error in the posterior radius of curvature that is within the experimental variability of the system. This finding suggests that accurate values of the in vitro posterior radius can be obtained by simply rescaling the distances using Eq. 6.1 with the appropriate value of the index. Experimentally, the average error in the posterior radius of curvature was found to 0.12 mm with a 95% confidence interval of 0.73 mm, which is very close to the error found with the simulations. The results of the simulations (Table 6.1 and Table 6.2) show that most of the error can be corrected by using a ray-tracing procedure assuming a uniform refractive index equal to the average group refractive index of the lens. Interestingly, the optimal refractive index for the correction is closer to the average index than the equivalent index. The majority of previous studies have used the equivalent index for correction.

The effect of the distortions on asphericity was more variable. For the posterior surface, the distortion produces a mean difference of -0.182, with a 95% confidence interval of ± 1.9. The experimental results suggest that reliable measurements of asphericity of the distorted surface cannot be obtained with the simple correction of equation 6.1. The result of the simulations (Table 6.2) suggest that a correction algorithm taking into account the GRIN is required to produce accurate values of the asphericity.

Overall, the simulations show that the GRIN makes a significant contribution to the distortion of the posterior surface, particularly in its estimated asphericity. When the GRIN is considered, the simulated posterior surface radius and asphericity are in very good agreement with the measurements obtained through the anterior surface (Table 6.1). Also, the best reconstruction of the posterior lens surface from OCT images in comparison to the nom-

inal surface (obtained by direct imaging of the posterior surface in "posterior up" position) is obtained when the optical distortion correction algorithm considers the GRIN (Table 6.2). Interestingly, the results of Table 6.2 suggest that correction of the optical refraction by the anterior surface using a GRIN model produces a relatively small improvement for the radius of curvature over a model that assumes a homogeneous index of refraction. The presence of GRIN has a larger impact in the reconstruction of the peripheral areas of the lens, as the largest improvements occur for the asphericity estimates.

In the current study, we used the Goncharov 3-variable model to describe the GRIN. While it is not the only possible GRIN lens model (we have obtained similar results with a different 3-variable model), choosing an adequate GRIN model that is representative of the actual lens gradient is critical. Simpler models, such as Goncharov's 2-variable models, failed to reproduce the distortion of the posterior surface.

In summary, we show that the GRIN produces significant distortions of the posterior shape of the lens, particularly in the lens periphery. However, when imaging in vitro lenses, accurate values of the central radius of curvature can be obtained using a simple correction that does not take into account refraction. The distortions can be predicted and corrected using a ray-tracing algorithm that incorporates an adequate model of the GRIN of the lens. Correction algorithms that assume a homogeneous index provide accurate values of the radius of curvature, but not of the asphericity. It is important to remember that these findings are applicable to in vitro studies. When imaging the lens in vivo, refraction by the cornea may induce significant additional distortions in both the radius and the asphericity.

6.5 Conclusion

The study reveals that the gradient index of refraction distorts the posterior surface of the lens when this is seen through the lens itself, as is occurs in all the in vivo methods to image the lens such as Scheimpflug or Optical Coherence Tomography.

The comparison between simulations using the ray tracing algorithm described in 2.2, and detected surfaces of different lenses using the OCT imaging system described in 2.4.2 shows that, in in vitro lenses, this influence is more relevant in the periphery of the lens.

While dividing the distorted surface heights by a homogeneous refrac-

tive index, or correcting the distortion assuming a homogeneous refractive index for the lens, provides good estimates for the radius of curvature of the posterior surface of the lens, the asphericity values retrieved are only accurate if the gradient index distribution of the crystalline lens is taken into account.

The description of the proposed method will be detailed in the next chapter and the correction will be applied to a set of lenses to study its performance with different gradient refractive index distributions.

Chapter 7

Distortion correction of Optical Coherence Tomography images of the crystalline lens: a gradient refractive index approach

This chapter is based on the paper by Siedlecki et al. [2012] "Distortion correction of OCT images of the crystalline lens: GRIN approach," Optometry and Vision Science 89(5), 709-18, 2012.

The contribution of the author of this thesis to the study was the design and implementation of the correction algorithm in MatLab and support in the discussion of the results and the writing of the paper.

The coauthors of this study were Damian Siedlecki, Enrique Gambra, Sergio Ortiz, David Borja, Stephen Uhlhorn, Fabrice Manns, Jean Marie Parel and Susana Marcos.

7.1 Introduction

In the previous chapters, we have shown that the optical distortion produced when imaging the crystalline lens with Optical Coherence Tomography (OCT) systems can be successfully used for gathering additional information on the sample. In fact, the presence of optical distortion in the images of the posterior surface of the crystalline lens (viewed through the anterior surface and the crystalline lens gradient refractive index (GRIN), has been used to reconstruct the GRIN distribution in simple spherical fish lenses [Verma et al., 2007], and the GRIN distribution of the crystalline lens in porcine (chapter 4) and human lenses (chapter 5).

The standard processing of OCT anterior segment images involves simple division of the optical path length signals by the tissue group index of refraction. A further sophistication of the method involves ray tracing through the tissue, and correction for the distortion produced by refraction, considering the deflection of the rays at the optical surfaces, but assuming a constant refractive index in the cornea, in the lens and in the aqueous humor. Fan and optical distortion correction algorithms have made possible to estimate the true shapes of all the ocular surfaces from the anterior segment in vivo, although the posterior surface of the crystalline lens is affected by the GRIN distribution in the lens.

We have previously studied the impact of the GRIN on the visualization and quantification of the posterior shape of crystalline lenses in vitro from OCT images (chapter 6). Comparisons with the actual lens posterior shape were possible, since the crystalline lenses were also imaged with the posterior surface up. Those comparisons suggested that, although the presence of GRIN seemed to have a minor influence on the estimated radius of curvature, the peripheral shape of the lens is misestimated if the actual GRIN distribution is not taken into account in the correction.

In this chapter we present the method to correct the distortion due to the lens optics and study the results in several human crystalline lenses in vitro. With an appropriate model of the GRIN distribution, the new algorithm would enable the in vivo estimation of the shape of the entire crystalline lens, and to assess its changes during aging or accommodation, providing a better understanding of these processes.

7.2 Methods

We propose a method for correction of optical distortion through the crystalline lens, applicable to estimate the undistorted posterior shape of the crystalline lens and lens thickness in vivo. The method was applied to a set of nine human lenses in vitro, as this allowed us a direct comparison of the reconstructed posterior lens surface and the actual posterior lens surface (also imaged with the posterior lens up), and the lens thickness. Images were obtained 2-dimensionally with the time-domain OCT system described in section 2.4.2, and the algorithm was based on the ray tracing algorithm through GRIN media described in methods chapter.

Figure 7.1 depicts a schematic diagram of the whole GRIN optical distortion procedure.

7.2.1 Human lens samples

The lenses used in this study are the set of lenses previously used in the study of the change of the GRIN with age in chapter 5. The mean age of the donor was 45 ± 20 years (ranged from 6 to 72 years). Eyes were received within 48 hours post-mortem, with measurements performed within an hour of lens extraction from the globe. The lenses were imaged with the OCT described in section 2.4.2. The surfaces of the lens were segmented and its thicknesses were calculated from the distortion produced in the cuvette holding the lens and the preservation medium [Uhlhorn et al., 2008].

7.2.2 Gradient refractive index model

For the purposes of this study we used the GRIN model introduced by Manns et al. [2010] used in chapters 4 and 5, where the gradient index is described by means of power coefficient p from the nucleus (with refractive index n_N) to the surface (with refractive index n_S) in all directions (equation 1.1).

The actual GRIN parameters for each lens were obtained from the previous study (chapter 5), where the same OCT data were used to estimate the GRIN distribution from the shape of the distorted posterior surface. In our calculations, we used both exact parameters of GRIN distribution estimated for each eye (those reported in chapter 5), as well as age-related fits to the experimental data. The surface and refractive indices at the nucleus, n_N, and at the surface, n_S, were obtained by linear fits to the data. A statistical

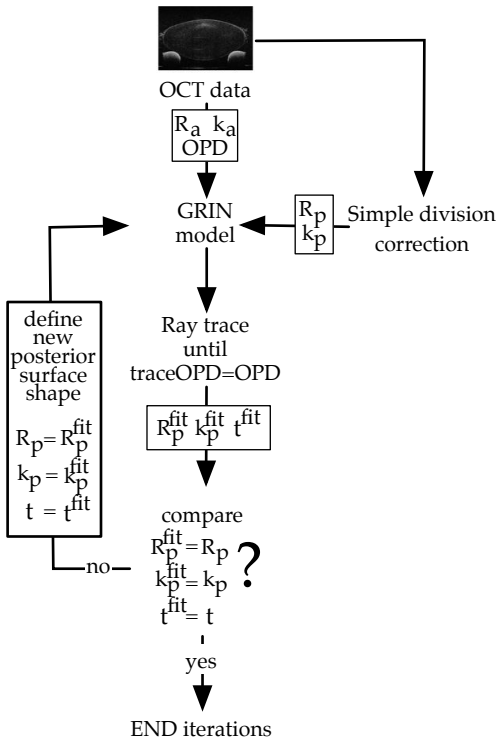

Figure 7.1: Block diagram illustrating the main steps of the GRIN distortion correction algorithm. Ra: anterior radius; ka: anterior conic constant; Rp: posterior radius of curvature; kp: posterior conic constant, t: thickness. (Reproduced from Siedlecki et al. [2012], Optometry and Vision Science).

analysis revealed that this was approach was not statistically significantly different than the mean ($n_N = 1.425$ and $n_S = 1.381$). The power coefficient, p, was fitted exponentially as a function of age (see figure 7.2).

7.2.3 Gradient refractive index distortion correction algorithm

In the natural orientation (anterior up position), the posterior surface of the lens is distorted by the deflection of the rays in the anterior surface and by the presence of a GRIN distribution in the lens. In order to retrieve the information on its shape, we developed an iterative algorithm based on Sharma's ray tracing algorithm in GRIN medium, where the parameters responsible

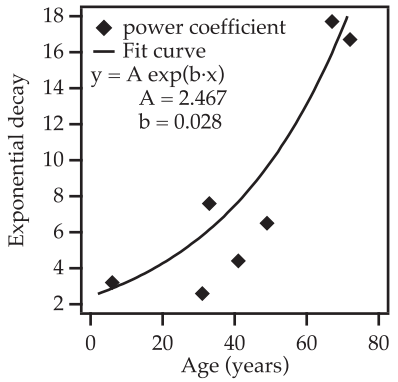

Figure 7.2: Exponential fit curve to the power coefficient data as a function of age. (Reproduced from Siedlecki et al. [2012], Optometry and Vision Science).

for posterior lens shape, and in consequence, for the GRIN distribution, are changed between iterations.

An anatomically plausible model of the GRIN distribution is assumed. Usually, the GRIN distribution is described by parameters that are independent from the lens shape (central and peripheral refractive indices and GRIN profile factor) and dependent of the lens shape (radius R_a and conic constant k_a of the lens anterior surface, radius R_p and conic constant k_p of the posterior lens surface, and thickness t).

1. An initial posterior lens surface defined by R_p, k_p and t is assumed. For the purpose of this calculation, the initial posterior lens surface was computed applying optical distortion correction algorithms assuming a constant refractive index

2. Rays are traced through the GRIN model using Sharma's algorithm until the OPD accumulated conincides with that measured with the OCT at every location. The intercepts between the ray and the posterior surface are not calculated. If the surface is posterior to the measured optical path distance (OPD), then the ray tracing is stopped before the ray reaches the surface. Otherwise, the model is extended so that the OPDs coincides.

3. The estimated locations in step 2 are fitted to a conic (R_p^{fit}, k_p^{fit} and t^{fit})

and the values of R_p, k_p and t parameters are substituted by the values of the new ones. The algorithm returns to step 2.

4. The iterations are stopped when the surface resulting from two consecutive iterations are comparable (i.e. less than 0.1 μm difference in terms of RMS metric).

As the Sharma algorithm is based on the Runge-Kutta method, it does not provide an exact match of the optical path length within the lens. However, we verified that this effect was negligible for sufficiently small discrete step sizes. A total of 400 rays, within a 4 mm pupil were used in the ray tracing. Unless otherwise noted, the Sharma step was set to 1 μm .

7.2.4 Data analysis

The accuracy of the lens posterior surface shape and lens thickness obtained from the application of the developed refraction and GRIN distortion correction algorithm on OCT images, was compared to those obtained from two other approaches for posterior lens shape and lens thickness estimations: (*a*) Division of heights of the points of distorted surface by an homogeneous index. This approach does not take into account refraction in the anterior lens surface nor the presence of a GRIN distribution in the lens and is followed widely in OCT imaging. (*b*) Application of optical (refraction) correction algorithms, considering the refraction at the anterior lens surface, but assuming a homogeneous refractive index. The algorithm works by calculating the refraction at every point of the anterior surface, and estimating the locations where the estimated OPD coincides with the measured one. For (*a*) and (*b*), the homogeneous average refractive indices were obtained from the study of Uhlhorn et al. [2008], were the group (not phase) refractive index was obtained at 825 nm, and an age-dependent expression is provided.

The accuracy of the posterior shape and lens thickness correction methods (the standard methods ((*a*) and (*b*) above) as well as the new method –using individual or fitted parameters in the GRIN model– was given as the differences with respect to the actual posterior lens shape and lens thickness, obtained from the crystalline lens.

A one-way ANOVA was used to test for significance of differences between the correction results.

7.3 Results

7.3.1 Accuracy in the reconstruction of the posterior lens shape

Figure 7.3 shows the shifts in the reconstructed lens surface radii of curvature (upper panels) and conic constant (lower panels), for individual subjects (a, c) and averaged across subjects (b, d), for the different reconstruction methods. Data are given relative to the actual parameters on the posterior lens shape (obtained from posterior-up measurements). Although there are great differences across subjects, the largest shift in radius of curvature, on average, occurs for the simple division method, while the refraction distortion correction (with a homogeneous index) and GRIN distortion correction (for both fitted and measured data) provide similar estimates of radius and conic constant in the posterior surface. The conic constant tends to be similarly retrieved with all methods.

While an independent analysis of radius of curvature and conic constant did not reveal significant differences across reconstruction methods ($F(3,32) = 0.056$, p-value = 0.982 for radius of curvature and $F(3,32) = 0.998$, p-value = 0.960 for conic constant), a comparison of the overall surface shape showed differences across methods. Figure 7.4 shows an example of difference maps (reconstructed-actual) for the four different reconstruction methods, for a 41 year old lens. When differences are expressed in terms of RMS and peak to valley differences, the GRIN distortion correction method (particularly with the actual GRIN parameters) showed significantly higher accuracy ($F(3,32) = 3.260$, p-value = 0.034 and $F(3,32) = 3.212$, p-value = 0.036 for RMS and peak to valley analysis, respectively), with the lowest accuracy found for the simple division by refractive index method (Figure 7.5).

7.3.2 Accuracy in the estimates of lens thickness

In particular, the GRIN distortion correction method produced significantly better estimates of the crystalline lens thickness ($F(3,32) = 3.983$, p-value = 0.032), compared to the other methods (Figure 7.6). The simple division and refraction (with homogeneous refractive index) provided, as expected, identical thickness estimates.

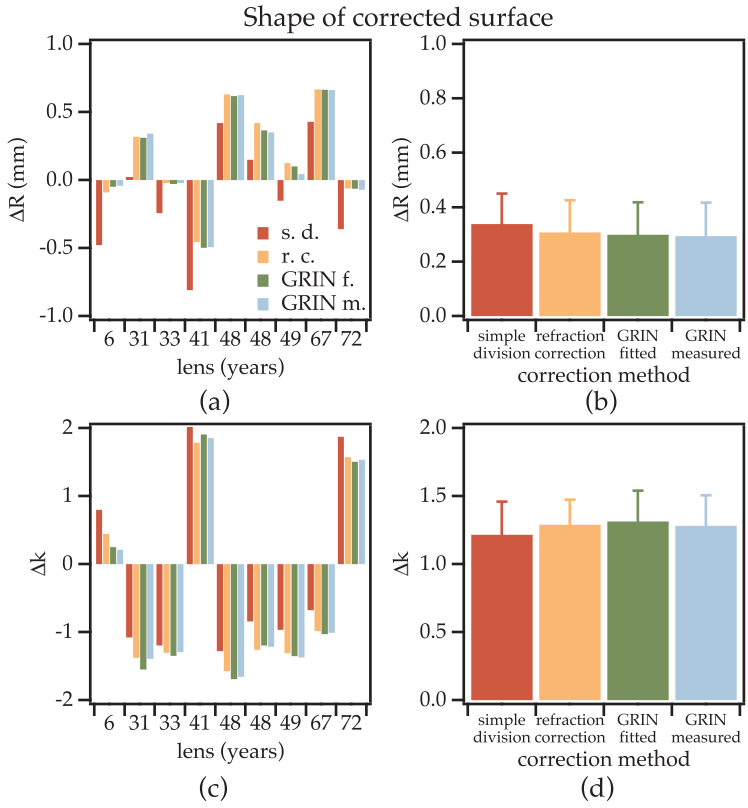

Figure 7.3: Differences between the shapes of the surface corrected for distortion relative to the actual shape, in terms of radius of curvature and asphericity. a) differences in radii of curvature obtained with the different methods for all the lenses from the study; b) mean values of the absolute difference between the corrected and actual radii of curvature. Error bars stand for standard deviation of the mean; c) differences in asphericity obtained with the different methods for all the lenses from the study; d) mean values of the absolute difference between the corrected and actual conic constants. Error bars stand for standard deviation of the mean. "s.d." stands for simple division method, "r.c." for refraction correction method; "GRIN-f" for GRIN distortion correction method with fitted shape independent parameters; "GRIN-m" for GRIN distortion correction method with optimal shape independent parameters. (Reproduced from Siedlecki et al. [2012], Optometry and Vision Science).

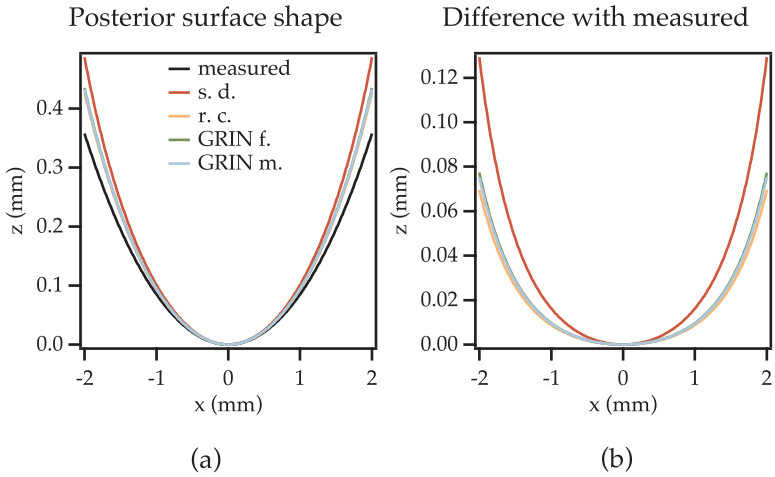

Figure 7.4: Differences between the real shapes of the posterior part of the 41 y.o. crystalline lens and the reconstructed ones with use of simple division correction (s.d), refraction correction (r.c), GRIN correction with approximated parameters of GRIN (GRIN f.), and GRIN correction with optimal parameters (GRIN m.).

7.3.3 Influence of Sharma step size

Decreasing the step of the Sharma ray tracing algorithm, increased the accuracy of the reconstruction (at the expense of increasing computational time). Figure 7.7 shows the average difference between the reconstructed and actual posterior surface (in terms of RMS or peak to valley) as a function of the ray tracing step, for both implementations of the GRIN distortion correction algorithm. Although in all cases the accuracy is very high ($< 30\,\mu m$), reducing the iteration step increased accuracy.

7.3.4 Convergence

The reconstruction algorithm is characterized by a very good convergence. For all the processed lenses, no more than 10 iterations were needed to reach the final parameters in the GRIN distortion correction procedure. In isolated cases (6, 31 and 48 year old lenses), the reconstruction algorithm provided two slightly different local minima, resulting in two slightly different sets of

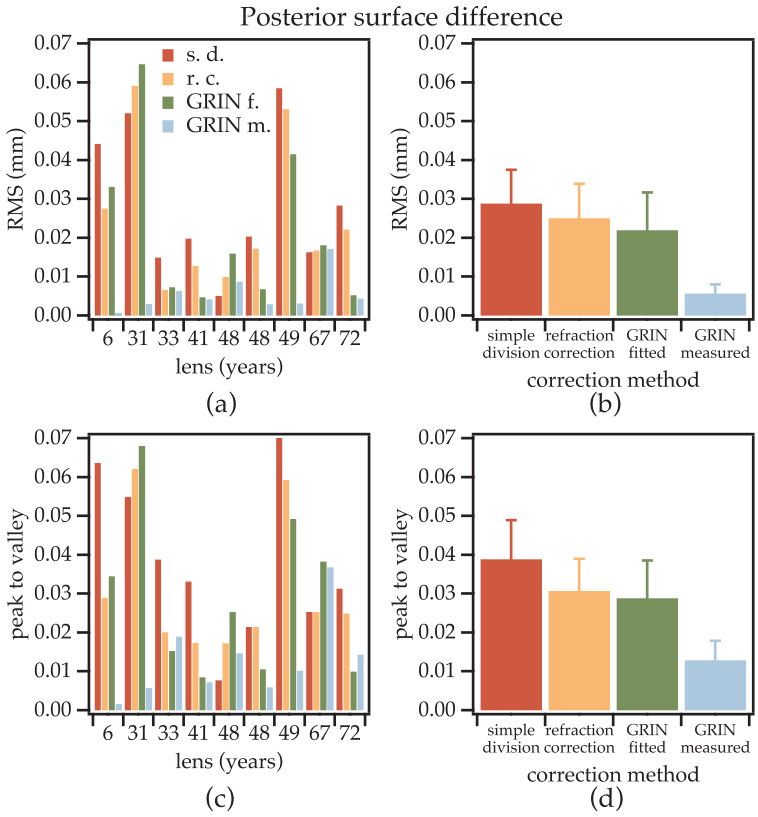

Figure 7.5: Differences between the shapes of the surface corrected for distortion relative to the actual shape, in terms of the calculated RMS error and peak to valley, from different reconstruction methods. a) RMS calculated for all the lenses from the study; b) mean RMS. Error bars stand for standard deviations of the mean; c) peak to valley differences for all the lenses from the study; d) mean values of peak to valley. Error bars stand for standard deviations of the mean. "s.d." stands for simple division method, "r.c." for refraction correction method; "GRIN-f" for GRIN distortion correction method with fitted shape independent parameters; "GRIN-m" for GRIN distortion correction method with optimal shape independent parameters. (Reproduced from Siedlecki et al. [2012], Optometry and Vision Science).

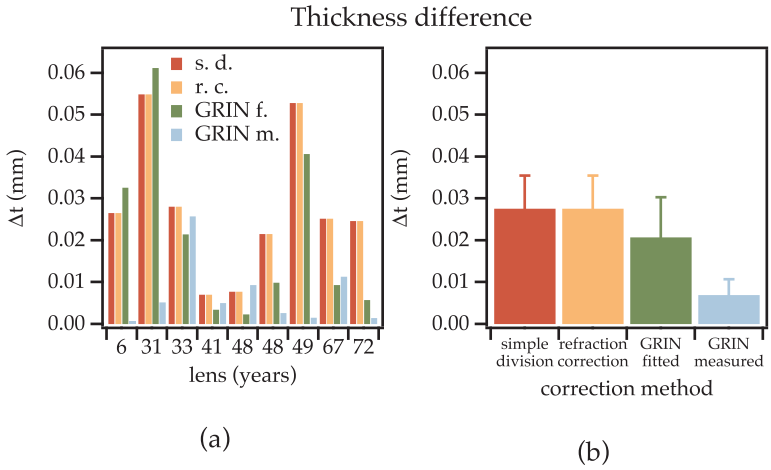

Figure 7.6: Differences between the thicknesses of the crystalline lens obtained for different methods of correction, relative to the actual thickness. a) thickness obtained with use of different methods for all the lenses from the study; b) mean values of the difference between the corrected and actual thickness obtained for different methods. "s.d." stands for simple division method, "r.c." stands for refraction correction method; "GRIN f." stands for GRIN distortion correction method with fitted shape independent parameters; "GRIN m." stands for GRIN distortion correction method with optimal shape independent parameters. (Reproduced from Siedlecki et al. [2012], Optometry and Vision Science).

values of radius of curvature and conic constant but the same value of lens thickness. Although for these minima, the differences of RMS error were small (up to 1%), the results described above referred to data from the solution which provides smaller RMS error between the actual and reconstructed shapes.

7.4 Discussion

In the present study we proposed an iterative method of optical distortion correction in OCT images of the crystalline lens incorporating the GRIN distribution inside the crystalline lens medium. A comparison with other

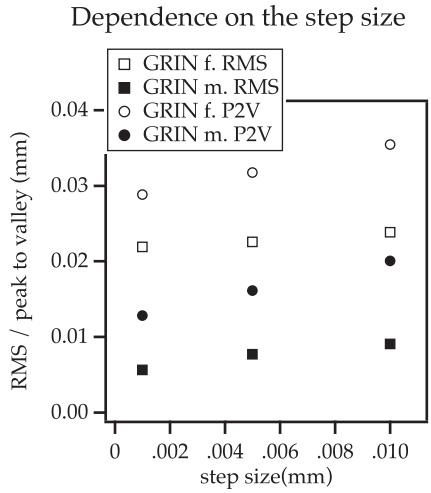

Figure 7.7: Dependence of the RMS and peak to valley of the posterior surface GRIN reconstruction algorithm on the step of the iteration in the Sharma's ray tracing algorithm. "GRIN-f" stands for GRIN distortion correction method with fitted shape independent parameters; "GRIN-m" stands for GRIN distortion correction method with optimal shape independent parameters. (Reproduced from Siedlecki et al. [2012], Optometry and Vision Science).

existing methods of posterior lens shape reconstruction shows slight improvements in the shape reconstruction for averaged input parameters of the GRIN model distribution and a significant improvement when optimal parameters for the GRIN (i.e., those corresponding to the same lens) were used. Very interestingly, the method has proved to reconstruct with high accuracy lens thickness, with knowledge of the anterior surface shape and distorted posterior lens shape only (and a model for GRIN distribution). The accuracy of the reconstruction (6 μm in the optimized GRIN reconstruction method) is similar to the reported accuracy of shadowphotography (12 μm), broadly used for biometric measurements of the crystalline lenses in vitro [Rosen et al., 2006]. Our findings show that, with an appropriate GRIN model, the use of GRIN distortion correction algorithms could reach similar accuracies in vivo. In fact, such accuracy is similar to the repeatability of in vivo lens thickness measurement by means of commercial OCT (8 μm) [Lehman et al., 2009]. It needs to be noted that according to the results presented in the

previous section, the thickness estimation has significant contribution to the RMS errors between the actual and reconstructed surfaces.

No significant differences were found across methods in the retrieved radius of curvature and conic constant, although the surface shape is generally best retrieved with the new reconstruction algorithm. This may be in part due to inaccuracies of the surface fitting. Urs et al. [2009] studied different methods for fitting the contours of isolated lens images, and found RMS errors in the fits, ranging from 11 to 70 μm, when using 10th order polynomial one lens curve fitting in the posterior lens surface. These fitting errors are of the order of magnitude of the RMS errors of our reconstruction. The use of conic surfaces, with less fitting parameters, is likely prone to higher inaccuracies. In fact, we have shown that comparisons of surfaces using a separate analysis of radius and asphericity may estimate incorrectly the statistical significance in the differences between surfaces, as various combinations of radius and asphericity may describe with similar accuracy the same noisy surface [Pérez-Escudero et al., 2010]. For example, the ranges of (correlated) radius and asphericity which described similarly Scheimpflug posterior corneal elevation data, were close to 0.2 mm and 0.6, respectively, only slightly lower than the accuracy found for those parameters in this study.

Our reconstruction algorithm is suited for in vivo OCT images of the crystalline lens. The access to the posterior lens surface and cuvette available only in vitro of the current study has only been used for comparison purposes. However, a limitation of the study is the general lack of GRIN distribution parametric data. Furthermore, as the OCT technique uses a low coherent light source, which is characterized by broadband wavelengths in the near infrared, taking into account the chromatic dispersion of the lens medium we assumed that the reconstructed GRIN was coincident with the group refractive index of the crystalline lens. In this study, we used GRIN data that came from our previous work [de Castro et al., 2011b], which included the set of lenses evaluated in the current study. As a result, it is not surprising that the best reconstruction was achieved with the optimal shape parameters of the GRIN in the individual lenses. As more data of GRIN distribution in larger sample become available, it is likely that the GRIN parameters obtained from fitting represent more robustly the population data. It should be noted that the GRIN distribution of isolated lenses will represent more closely the GRIN profile in a maximally accommodated lens, which should be considered when extrapolating GRIN models to perform recon-

structions from OCT in vivo measurements [Kasthurirangan et al., 2008]. GRIN distribution estimates in lenses in vitro under simulated accommodation (i.e. with an artificial stretching system) [Manns et al., 2007], may allow a more direct application of GRIN models to measurements in vivo.

In the current study we have described a possible implementation of the algorithm, but its core is quite flexible. Basically, instead of Sharma's, other numerical ray tracing and optical path estimation procedures, could be adapted to different GRIN models. The only condition for the GRIN model is that it is anatomically plausible, with the isoindicial surfaces functionally related to the external shape of the lens.

We have described an implementation of the algorithm in 2-D, but it could be easily extended three-dimensionally. In a previous work we demonstrated computationally a significantly higher accuracy in the reconstruction of the posterior surface when optical distortion correction algorithms were applied in 3-D [Ortiz et al., 2010]. For example, in a computer eye model with homogeneous index of refraction (and simulated conic surfaces), there was not a significant difference in the reconstruction of the posterior lens asphericity by applying a simple division by the refractive index or 2-D refraction distortion correction (with discrepancies of about 50% from the nominal value). However, 3-D refraction distortion correction allowed retrieval of the asphericity within 0.3% error.

The algorithm for optical distortion correction through gradient index proposed in the current study will therefore show full potential on 3-D images of the crystalline lens in vivo [Gambra et al., 2010], particularly as GRIN models of the crystalline lens based on larger populations than current data become available.

7.5 Conclusions

The study confirmed that the distortion of the optical surfaces observed in OCT images can be corrected taking into account the gradient refractive index of the crystalline lens. If the GRIN is known, this correction would improve the simple division or refraction correction method using an homogeneous refractive index.

The improvement is not apparent in this study when radius of curvature or asphericity are treated independently. However, the differences between methods are statistically significant when comparing both surfaces directly.

A larger pupil size would allow to study the periphery of the lens where the differences between GRIN and homogeneous index would be more relevant as shown in chapter 6.

The method can be applied if the gradient refractive index of the crystalline lens is known. In this study we corrected the distortion observed in a set of lenses whose GRIN was previously calculated. However, as larger data sets of GRIN profiles in human lenses are gathered, average data (in different age groups) could be used in the reconstruction of the posterior surface.

Chapter 8

Conclusions

This thesis addresses the reconstruction of the gradient index of refraction (GRIN) of the non-spherical crystalline lens using an optimization to estimate the best parameters of a GRIN model that fits the experimental data. We have validated the method with computational simulations, studied the influence of the GRIN in the optics of the crystalline lens and shown the benefits of correcting the Optical Coherence Tomography (OCT) images considering the refractive index distribution of the lens.

In this thesis, we have accomplished the following achievements:

- A novel reconstruction method of the GRIN distribution in non-spherical lenses, using for the first time in the literature a genetic algorithm approach.
- Experimentally estimated errors of the input data for the GRIN reconstruction algorithms, from Laser Ray Tracing and Optical Coherence Tomography
- State of the art accuracy in the reconstruction of GRIN.
- First reconstruction of GRIN distributions in a porcine lens using OCT images.
- First three dimensional measurements of the GRIN distribution, including the first report of meridional changes in the GRIN distribution.
- First direct estimate of the role of the surface shape and GRIN on the spherical aberration and astigmatism.
- First report on the variation of the GRIN with age of human crystalline lenses, based on optical methods.
- First study of the effect of GRIN on OCT imaging of the posterior lens surface.
- First proposal for optical distortion correction of OCT images of the crystalline lens involving ray tracing through GRIN.

The development of the reconstruction method and the experimental results allow us to conclude that:

1 It is possible to reconstruct the GRIN of the non-spherical crystalline lens with optimization methods when the external geometry of the lens is known. We have shown, with computational simulations, that different experimental data from Laser Ray Tracing of Optical Coherence Tomography can be used to reconstruct the GRIN, and that the best accuracy is achieved if optical path extracted from OCT images is used (RMS difference below 0.005).

2 The GRIN of the porcine crystalline lenses can be reconstructed with the method proposed in this thesis using a 3-D exponential model. The surface and nucleus phase refractive index at 633 nm were estimated to be 1.354 and 1.434 respectively, and the exponential decay factor was 2.6 in axis and changed from 3.5 and 5.1 in the meridional axis.

3 The presence of the GRIN impacts the optics of the crystalline lens. In particular, the presence of GRIN shifts the spherical aberration of the lens from positive values (considering the same surface and a homogeneous refractive index) towards negative values. The presence of GRIN also influences the astigmatism of the lens.

4 The human crystalline lens GRIN distribution changes with age. In younger subjects the GRIN of the lens shows a smooth distribution while in older there is an abrupt refractive index increase near the surface. The results show that although surface and nucleus refractive indices do not change with age, there is a statistically significant change of the exponential decay factor that describes the profile shape, at a rate of 0.24 ± 0.05 per year. Average values of the surface and nucleus phase refractive indices at 589 nm were 1.373 ± 0.014 and 1.417 ± 0.011.

5 The effect of the GRIN in the distortion of the posterior surface observed through the anterior lens in OCT, is relevant mainly in the periphery of the lens. The correction of the distortion assuming a GRIN model improves the methods previously proposed in the literature, which currently assume a homogeneous index. The quantification of the OCT images to extract the biometry of the posterior surface of the lens benefits if the GRIN of the lens is considered.

Future work

A direct follow-up of the studies presented here includes the 3-D reconstruction of a larger number of human crystalline lenses, of various ages. The results will support and provide a deeper understanding of the GRIN distribution in human lenses. The author of this thesis is currently involved in this part of the work.

Other options in the optimization methods must be studied. In particular, the incorporation of additional input data, such as the focal length of the crystalline lens or the optical path at different orientations, will allow a more robust search, and a more accurate reconstruction of the crystalline lens GRIN. Current improvements of the method in our lab incorporate the measurement of the back focal length of the crystalline lenses for two pupil diameters. Twelve human crystalline lens data have been already measured three-dimensionally with the additional input data.

In vitro studies allow the possibility of studying the crystalline lens under different levels of simulated accommodation. The change of the distribution of refractive index when the external shape is modified, and its influence in the accommodative process, will provide extremely valuable information for the understanding of the physical changes occurring in the lens with accommodation. Measurements in Cynomolgus monkey lenses have been performed in collaboration with the Bascom Palmer Eye Institute, and the data analysis is in progress.

Ultimately, a major application of the developed methods for GRIN distribution estimation is the reconstruction of the GRIN in vivo. The performance of the method with additional input data will allow us to test their potential viability for in vivo reconstruction. A major challenge to the in vivo reconstruction of GRIN from OCT data, is that posterior surface shape is dependent on the GRIN and therefore the shape of the refractive index profile and the shape of the posterior surface are strongly coupled. However, a deeper knowledge of the GRIN distribution, as measured in vitro, will allow to narrow the solution space sufficiently to be able to extract a measurement of the GRIN in in vivo eyes with optical methods.

Summary of the chapters in Spanish

Esta tesis estudia la óptica del sistema visual y en particular la estructura del cristalino, desarrollando métodos para estimar el gradiente de índice de refracción (GRIN) del mismo. A pesar de que hay una larga tradición en modelar las propiedades refractivas del ojo, todavía se discuten la óptica del cristalino y los valores específicos de índice de refracción. El conocimiento preciso del gradiente de índice de refracción permitirá comprender mejor las propiedades ópticas del cristalino y la contribución del mismo a la calidad óptica del ojo.

El cristalino permite cambiar el estado refractivo del ojo, acomodar, para hacer imagen de objetos a distintas distancias. El estudio de la acomodación del cristalino ha estado limitado, hasta no hace mucho, a la medida de los cambios en la forma de las superficies. Además, el cristalino crece continuamente con la edad y esto podría afectar a la distribución de índices de refracción. Para describir con precisión la óptica del ojo, se necesita un conocimiento más detallado de la óptica del cristalino.

La investigación llevada a cabo en esta tesis se centra en la reconstrucción del gradiente de índice de refracción del cristalino con métodos de optimización. Utilizando un modelo apropiado del GRIN del cristalino, los parámetros que mejor ajustan los datos experimentales (y por tanto la distribución GRIN) pueden ser encontrados con un algoritmo de optimización.

Los primeros estudios relativos al índice de refracción del cristalino usaron métodos destructivos, por ejemplo, seccionando el cristalino en láminas delgadas para medir el índice de refracción estudiando la reflexión o la refrac-

ción de un rayo al pasar por ellas. Estudios más recientes, proponen extraer datos de la estructura de gradiente de índice usando datos experimentales en lentes aisladas, in vitro. Uno de estos métodos, el uso de imágenes de resonancia magnética, ha sido aplicado por primera vez in vivo en una publicación. Sin embargo, hay muchas preguntas abiertas dado que todos los métodos tienen desventajas. En los valores publicados de índice de refracción en el centro o el borde del cristalino reportados en la literatura, se observa mucha dispersión y todavía se desconoce si esto es debido al error experimental de la medida o realmente, dicha dispersión se encuentra en la población. Además, la distribución de índices de refracción, es decir, el modo en que el índice de refracción cambia desde el núcleo hasta la superficie, no es un consenso en la comunidad científica. La dificultad en las medidas oculta una explicación clara sobre la influencia de la estructura de gradiente de índice en la óptica del ojo.

Capítulo 1: Introducción

En la introducción de esta tesis se realiza una revisión de los conocimientos sobre la óptica del cristalino humano. El cristalino es una lente biconvexa con una distribución de gradiente de índice de refracción que alcanza su máximo cerca del centro del cristalino y decae hacia la superficie.

Los métodos de medida de la forma de las superficies del cristalino son revisados. En medidas in vitro la forma exterior del cristalino es accesible pero en medidas in vivo el cristalino es observado a través de la córnea, lo cual distorsiona la imagen. Es posible obtener la forma de la superficie anterior del cristalino conociendo la forma de la córnea y el índice de refracción de los medios precedentes. Sin embargo, el estudio de la superficie posterior del cristalino, al igual que su posición dentro del ojo, ha estado siempre limitado por el desconocimiento del gradiente de índice del mismo. Normalmente se asume un índice equivalente (aquel con el que una lente con la misma forma externa tiene igual potencia que el cristalino), pero los errores cometidos al realizar esta aproximación no han sido cuidadosamente estudiados.

Desde hace ya más de un siglo, se construyen modelos de gradiente de índice para simular el comportamiento del cristalino y estudiar las propiedades del mismo. Los modelos más relevantes del cristalino humano son descritos y el origen y diferencias entre ellos discutidos.

No hay muchos estudios sobre la dispersión cromática del cristalino. Dado que en la literatura, las medidas se realizan con fuentes de luz de diferentes longitudes de onda, esto es algo a tener en cuenta en nuestro estudio sobre el gradiente de índice de refracción del cristalino.

Por último se hace una revisión de los métodos de medida del gradiente de índice de refracción. Hace ya tres siglos de los primeros estudios sobre el índice de refracción del cristalino. La llegada del refractómetro de Abbe permitió un instrumento preciso para medir índices de refracción pero no solucionó el problema definitivamente dado que es una técnica destructiva y el tejido puede alterarse al ser extraído para su medida.

Desde hace poco más de 30 años se ha avanzado en distintos métodos de medida o estimación del gradiente de índice de refracción en cristalinos in vitro, es decir, sin destruir el mismo para la medida de su gradiente de índice.

Asumiendo ciertas condiciones se puede relacionar, por medio de una

integral, el gradiente de índice del cristalino con la desviación que sufren los rayos al pasar por el mismo. De la inversión de esa integral resulta un método de medida que ha sido muy utilizado en las úlitmas décadas en cristalinos in vitro.

Hay varios trabajos en la literatura que intentan obtener datos del gradiente de índice con optimizaciones, es decir, minimizando una función de mérito. Se trata de buscar los parámetros de un modelo que mejor representan los datos experimentales. Es en este apartado donde se encuadra el método propuesto en esta tesis doctoral. Hasta el momento los estudios en esta dirección o bien tenían pocos datos del cristalino o bien utilizaban un modelo simple debido a las dificultades de la optimización. En el trabajo realizado en esta tesis doctoral hemos utilizado algoritmos genéticos como algoritmo de optimización y hemos estudiado qué datos experimentales son necesarios para reconstruir el gradiente de índice de refracción del cristalino con una precisión aceptable.

Por último, muy recientemente, se han aportado datos de medida de gradiente de índice de refracción utilizando imágenes de resonancia magnética. Este método ha sido el primero, y por ahora el único, en utilizarse in vivo y gracias a él, se han publicado estudios sobre el cambio en la distribución de gradiente de índice no solo con la edad sino también con la acomodación en cristalinos in vivo. Sin embargo, la precisión del método depende de una cuidadosa calibración que es discutida y la baja precisión del mismo y el coste en la obtención de las imágenes, parecen ralentizar su desarrollo.

Capítulo 2: Métodos

Este capítulo describe los algoritmos y los métodos experimentales utilizados en el trabajo de tesis doctoral.

Se ha programado un algoritmo de trazado de rayos sobre medios homogéneos y sobre medios de gradiente de índice de refracción en MatLab para simular los datos observados experimentalmente. Este algoritmo es descrito y validado con un programa de diseño óptico.

El trazado de rayos sobre medios de gradiente de índice se hace por medio del método de Runge-Kutta, que es una solución numérica de la ecuación diferencial paso a paso. El tamaño de dicho paso es un compromiso entre velocidad (pasos grandes) y precisión (pasos pequeños). El paso más adecuado para la forma y magnitud del gradiente de índice fue calculado observando distintos datos de trazado de rayos a través del cristalino con distintos tamaños de paso.

Se describen los algoritmos genéticos y las distintas posibilidades de los mismos así como la implementación final en MatLab. El algoritmo de búsqueda propuesto para reconstruir el gradiente de índice de refracción del cristalino realiza una búsqueda global para evitar caer en mínimos locales, seguida de una búsqueda local una vez que el área donde se encuentra el mínimo está localizado.

Por último los sistemas experimentales de medida utilizados son descritos. Se implementó un sistema experimental para estudiar los datos accesibles con una vista lateral del trazado de rayos o los impactos en una retina artificial y se realizaron medidas en lentes de vidrio para obtener una medida del error experimental en este tipo de medidas. Se utilizaron también dos sistemas de Tomografía de Coherencia Óptica (OCT). Uno de ellos hace imagen en el dominio del tiempo. Fue desarrollado e implementado en el Ophthalmic Biophysics Center del Bascom Palmer Eye Institute de Miami, Estados Unidos, y se utilizó para obtener imágenes bidimensiones del cristalinos humanos. Otro sistema, que utiliza el dominio de la frecuencia para extraer imágenes y que fue desarrollado e implementado en el Instituto de Óptica en colaboración con la Copernicus University en Toruń, Polonia, permite la obtención de imágenes tridimensionales. En esta tesis fue utilizado para hacer imagen de un cristalino porcino y para reconstruir tridimensionalmente su índice de refracción.

Capítulo 3: Precisión en la reconstrucción del gradiente de índice con métodos de reconstrucción basados en datos de trazado de rayos o tomografía de coherencia óptica

En este capítulo estudiamos la precisión de la reconstrucción del gradiente de índice (GRIN) usando métodos de optimización cuando se utilizan distintos datos experimentales. El capítulo está basado en el artículo [de Castro et al., 2011a], publicado en la revista Optics Express.

Algunos métodos, previamente propuestos en la literatura, de reconstrucción del GRIN usan las desviaciones de los rayos que pasan por el cristalino como data de entrada para los algoritmos de optimización [Axelrod et al., 1988; Garner et al., 2001] y otros, relacionan estos datos con el GRIN obteniendo éste último por medio de la inversión de una integral [Campbell, 1984; Chan et al., 1988; Pierscionek et al., 1988] o, por medio de un proceso iterativo [Acosta et al., 2005; Vazquez et al., 2006]. Las desviaciones de los rayos, debido al paso a través del cristalino, pueden medirse si se sitúa una cámara enfocando el plano meridional. Estos datos se han usado para obtener el GRIN de cristalinos esféricos y no esféricos extraidos de ojos de peces y cerdos respectivamente.

Sin embargo, el diagrama de impactos puede ser obtenido si la cámara se sitúa después del cristalino. Este tipo de configuración se ha usado en validaciones de técnicas aberrométricas basadas en trazado de rayos. En contra de las técnicas basadas en imágenes laterales de los rayos, una configuración basada en la grabación del diagrama de impactos, podría ser implementada in vivo por medio de una configuración de doble paso.

En una imagen de Tomografía de Coherencia Óptica (OCT) las distncias verticales entre superficies son una medida del camino óptico acumulado por cada rayo a su paso a través del cristalino. El uso de las diferencias de camino óptico ha sido utilizado para reconstruir el gradiente de índice en lentes esféricas de ojos de pez in vivo por Verma et al. [2007].

En este capítulo comparamos la precisión de la reconstrucción en cristalinos no esféricos utilizando cinco tipos de datos experimentales accesibles con los sistemas descritos en el capítulo anterior: (*1*) la deflexión de los rayos al pasar por el cristalino, (*2*) la deflexión de los rayos a su paso por el crista-

lino y el punto de salida del mismo, (*3*) los impactos en un plano posterior al cristalino, (*4*) el camino óptico acumulado por los rayos al atravesar el cristalino, i.e. entre la cara anterior y la cara posterior del cristalino y (*5*) el camino óptico acumulado hasta la superficie posterior del cristalino y hasta un plano posterior. Asumiremos en todos los casos que la forma del cristalino y su espesor es conocido y comprobaremos las reconstrucciones bajo diferentes niveles de error en los datos experimentales.

Para estimar el error experimental, hemos realizado medidas experimentales en lentes de vidrio cuyos valores nominales pueden ser calculados con un trazado de rayos teórico con los datos de las especificaciones. También hemos estudiado la influencia del error en la estimación de la forma de la superficie y su efecto en la reconstrucción del GRIN. Finalmente hemos estudiado la dependencia de la reconstrucción con la cantidad de datos experimentales simulando la reconstrucción con un número creciente de rayos.

La desviación de la reconstrucción del gradiente de índice de la distribución nominal se incrementa cuando lo hace el error en los datos de entrada. Sin embargo, para niveles de error del orden de los medidos experimentalmente en el sistema de trazado de rayos y OCT, el gradiente de índice es reconstruido con una precisión de 0.005 de media en todo el cristalino. Se demuestra además que, para la misma cantidad de error experimental, las mejores reconstrucciones se obtienen con datos de diferencia de camino óptico de los rayos entre la superficie anterior y posterior del cristalino (configuración 4) y diferencia de camino óptico hasta la superficie posterior y hasta un plano posterior al cristalino (configuración 5). Esto significa que los datos de diferencia de camino óptico son los más adecuados como datos de entrada para la reconstrucción del gradiente de índice con métodos de optimización y, por ello, serán los datos utilizados en los próximos capítulos.

Capítulo 4: Reconstrucción tridimensional del gradiente de índice de refracción del cristalino con imágenes de tomografía de coherencia óptica

En este capítulo presentamos una aplicación directa de los métodos de optimización antes descritos. En concreto se utilizan imágenes de Tomografía de Coherencia Óptica (OCT) para recuperar el gradiente de índice de refracción (GRIN) de un cristalino porcino. El capítulo está basado en el artículo [de Castro et al., 2010], publicado en la revista Optics Express.

Se tomaron imágenes tridimensionales de un cristalino in vitro con el OCT en dos orientaciones (con la superficie anterior hacia arriba y con la superficie posterior hacia arriba), lo que permitió calcular la geometría del cristalino. El espesor se calculó observando la deformación de la cuveta utilizada en las medidas in vitro al ser observada a través del cristalino [Uhlhorn et al., 2008]. El método de reconstrucción buscó los parámetros de un modelo de gradiente de índice de refracción de 4 variables que mejor ajustaban la distorsión observada en la cara posterior del cristalino, esto es, el GRIN que mejor simulaba los datos de camino óptico acumulado por los rayos a su paso por el cristalino medidos en las imágenes de OCT. En el modelo [Manns et al., 2010], el índice de refracción varía siguiendo una ecuación exponencial entre el núcleo y la superficie, que mantiene un índice constante.

Se realizaron simulaciones para estudiar la precisión de la reconstrucción en presencia de ruido en la detección de las superficies con el modelo de 4 variables utilizado en este estudio. Las simulaciones muestran que suponiendo un ruido de 5 μm en el cálculo de las diferencias de camino óptico, los índices en la superficie y en el núcleo del cristalino pueden ser calculados con una precisión de 0.010 y 0.003 respectivamente.

Experimentalmente hemos encontrado en un cristalino porcino un índice de refracción variable entre 1.353, en la superficie, y 1.434, en el núcleo. El factor de decaimiento exponencial que mejor ajustaba los datos experimentales fue 2.62, en el eje óptico, y variable entre 3.56 y 5.18, meridionalmente.

Se estudió el efecto del GRIN en las aberraciones trazando rayos en un modelo con las superficies medidas y, o bien el índice equivalente o bien el GRIN calculado. La aberración esférica estimada del cristalino fue

2.87 μm asumiendo el índice homogéneo. La presencia del GRIN desplazó la aberración esférica hacia valores negativos, −0.97 μm, para una pupila de 6 mm de diámetro. El gradiente de índice del cristalino recuperado, debido a su asimetría, cambia además el signo del astigmatismo.

En éste capítulo se valida el método antes propuesto y se reconstruye el GRIN de un cristalino porcino, estudiado ya en la literatura con otras técnicas. Además de aportar datos, por primera vez en la literatura, que implican que el astigmatismo del cristalino no es solo debido a la forma de sus superficies sino también, a la distinta distribución de GRIN en distintos meridianos.

Capítulo 5: Cambio del gradiente de índice de refracción del cristalino humano con la edad

Se aplicaron las técnicas de optimización basadas en el estudio de las imágenes de Tomografía de Coherencia Óptica (OCT) para reconstruir la distribución del gradiente de índice de refracción (GRIN) presente en el cristalino humano. Se estudió la dependencia con la edad de las variaciones de esta distribución. Este capítulo está basado en el artículo [de Castro et al., 2011b], publicado en la revista Journal of Modern Optics.

Se estudiaron imágenes de nueve cristalinos humanos con edades entre 6 y 7 años (tiempo post mortem entre 1 y 4 días) con un sistema de OCT. Los cristalinos se extrajeron de ojos cadaver y se midieron en una cámara rellena de líquido de preservación (DMEM). Se hizo imagen de los cristalinos con la superficie anterior hacia arriba y luego se les dio la vuelta para hacer de nuevo imagen con la cara posterior hacia arriba. De esta forma se obtuvo la superficie anterior y posterior de los mismos sin distorsión, y distorsionada debido a la refracción a través de la otra superficie y el GRIN del cristalino. El espesor del cristalino se calculó estudiando la deformación de la cuveta en las imágenes.

La distribución de GRIN se describió con tres variables por medio de una ecuación exponencial. Las variables fueron el índice del núcleo, el índice de la superficie y el coeficiente exponencial que describe la caída de índice de refracción entre el núcleo y la superficie. Utilizamos el método de optimización para buscar el valor de las tres variables que mejor ajustaba la distorsión producida en las imágenes de OCT. Dicha distorsión fue simulada con una precisión similar a la resolución del sistema de medida (por debajo de 15 μm).

Los valores de índice de refracción de superficie y núcleo para las distintas lentes fueron entre 1.356 y 1.388, y entre 1.396 y 1.434 respectivamente. No se observó un cambio significativo de estos parámetros con la edad. Sin embargo se puede ver en los resultados que el coeficiente exponencial se incrementa significativamente con la edad a un ritmo de 0.24 cada año. Este coeficiente tomo valores entre 3 y 18.

Se concluye así que el método propuesto en esta tesis permite medidas no invasivas del perfil de gradiente de índice del cristalino humano ex vivo. La variación con la edad del GRIN resultado de este estudio es consistente

con datos previos utilizando técnicas de resonancia magnética, y con la formación progresiva de un plateau de índice de refracción constante en el centro del cristalino.

Capítulo 6: Distorsiones en la superficie posterior del cristalino en imagenes de tomografía de coherencia óptica en cristalinos in vitro: efecto del gradiente de índice

En este capítulo se cuantifica al influencia del gradiente de índice de refracción (GRIN) en la distorsión observada en las imágenes de Tomografía de Coherencia Óptica (OCT) de cristalinos aislados. Está basado en el artículo Borja et al. [2010], publicado en la revista Biomedical Optics Express.

Se utilizaron 12 cristalinos de 12 donantes distintos con edades entre 6 y 90 años. Se tomaron imágenes de OCT en las dos posiciones descritas en el capítulo anterior (superficie anterior arriba y superficie posterior arriba) para cuantificar la forma de la superficie con y sin distorsión.

Se comparó la superficie distorsionada (la posterior en las imágenes con la superficie anterior arriba o la anterior en las imágenes con la superficie posterior arriba) con predicciones de un trazado de rayos suponiendo un modelo de cristalino descrito por un índice de refracción homogéneo, ya sea el índice equivalente o el índice promedio, y con un modelo de gradiente de índice. También se estudió la posible corrección de la distorsión observada usando tres estrategias distintas (*1*) sin tener en cuenta la refracción en la primera superficie del cristalino ni el efecto del gradiente de índice, (*2*) simulando la refracción en la primera superficie asumiendo un modelo homogéneo de índice de refracción y (*3*) simulando la refracción tanto en la superficie como en el gradiente de índice y modelando este último con un modelo dependiente de 3 variables propuesto por Goncharov and Dainty [2007].

Los resultados muestran que el error, al simular la distorsión utilizando modelos con y sin gradiente de índice, en el radio de curvatura, está en el orden de reproducibilidad de las medidas. De forma similar, la corrección asumiendo que el cristalino se puede describir con un índice homogéneo dio buenos resultados en términos de radio de curvatura. Así, la distorsión puede ser simulada y corregida asumiendo un índice de refracción homogéneo, y obtener valores correctos de radio de curvatura. A pesar de que la mayoría de estudios que corrigen las imágenes de OCT y asumen un índice homogéneo utilizan el índice de refracción equivalente, definido estudiando

la potencia del cristalino, se observó que el índice homogéneo que resultaba más conveniente para obtener la forma de la superficie posterior era el índice promedio, que se define a través de la diferencia de camino óptico en el centro del cristalino.

Sin embargo, para simular correctamente la asfericidad de la superficie distorsionada, es necesario tener en cuenta el gradiente de índice de refracción. De igual manera, la corrección de la distorsión produce buenos resultados en términos de asfericidad solo cuando el gradiente de índice de la lente es introducido en el algoritmo de corrección.

En resumen, hemos encontrado que el GRIN produce una distorsión significativa en la superficie posterior del cristalino cuando se hace imagen del mismo con un sistema OCT y que esta distorsión es notoria en la periferia del cristalino. No obstante, en medidas in vitro, se pueden obtener radios de curvatura de forma precisa utilizando una corrección sencilla que no tenga en cuenta la refracción en la primera superficie. La distorsión puede ser predicha y corregida con un algoritmo que incorpore trazado de rayos y un modelo adecuado de gradiente de índice. Estos resultados son aplicables en estudios in vitro ya que, en imágenes del cristalino in vivo, la refracción en la córnea puede introducir otras distorsiones en el radio de curvatura y la asfericidad de las superficies distorsionadas.

Capítulo 7: Corrección de la distorsion en imágenes de tomografía de coherencia óptica teniendo en cuenta el gradiente de índice del mismo

En este capítulo se propone un método para corregir la distorsión de las imágenes de Tomografía de Coherencia Óptica (OCT) de la superficie posterior del cristalino humano teniendo en cuenta su distribución de gradiente de índice de refracción (GRIN) y se compara dicha reconstrucción con los métodos utilizados en la literatura. El capítulo está basado en el artículo Siedlecki et al. [2012], aceptado para su publicación en la revista Optometry and Vision Science.

Las medidas con OCT sobre el set de cristalinos que se utilizó en el capítulo 5 y el modelo y la distribución GRIN calculada en dicho estudio, se utilizan ahora para validar el método. Los resultados de la corrección fueron evaluados comparando con la forma nominal de la superficie (accesible en estas medidas in vitro en la imagen con la superficie posterior arriba). Además se compara el resultado del nuevo método con otros dos existentes: (*1*) división del camino óptico por un índice homogéneo, esto es, sin tener en cuenta ni la refracción de los rayos en la superficie anterior ni el gradiente de índice y (*2*) corrección de la refracción suponiendo un índice constante. Se compararon los radios de curvatura de las superficies, la constante cónica y la raíz cuadrática media y el valor máximo de la diferencia entre la superficie corregida y la nominal.

No se encontraron diferencias estadísticamente significativas en el radio y la constante cónica recuperadas con los distintos métodos. Sin embargo la corrección teniendo en cuenta el GRIN produjo resultados más precisos en términos de raíz cuadrática media y valores máximos de la diferencia con errores de menos de 6 μm y 13 μm de media respectivamente. Se encontró también que el espesor es calculado con más precisión con el nuevo método, con una diferencia promedia de 8 μm

De los resultados se concluye que la superficie posterior del cristalino y el espesor del mismo pueden ser reconstruidos de forma muy precisa desde las imágenes de OCT y que la precisión mejora si se tiene un modelo acertado de la distribución de índice de refracción del cristalino. El algoritmo propuesto puede ser utilizado para mejorar el conocimiento del cristalino en imágenes

de OCT in vivo. Aunque las mejoras sobre otros métodos son modestas en dos dimensiones y con pupilas de 4 mm de diámetro, es de esperar que estudios con un mayor tamaño de pupila se beneficiarán en mayor medida de la técnica propuesta. El método también se beneficiaría de un mayor número de datos experimentales de la distribución de gradiente de índice del cristalino.

Translation of conclusions to Spanish

Esta tesis estudia la reconstrucción del gradiente de índice de refracción (GRIN) del cristalino no esférico utilizando una optimización para buscar los parámetros de un modelo de GRIN que reproducen con más precisión los datos experimentales. Hemos validado el método con simulaciones y hemos reconstruido el gradiente de índice de un cristalino porcino tridimensionalmente y de un set de cristalinos humanos para estudiar la influencia del GRIN en la óptica del cristalino, su cambio con la edad. Además hemos estudiado los beneficios en la corrección de la distorsión en las imágenes de Tomografía de Coherencia Óptica (OCT) cuando se considera la distribución de índice de refracción del cristalino.

En esta tesis, reportamos los siguientes logros:

- Un método nuevo de reconstrucción del GRIN en cristalinos no esféricos que utiliza, por primera vez en la literatura, un algoritmo global basado en algoritmos genéticos.
- Los errores de los datos de entrada al algoritmo (datos de trazado de rayos y Tomografía de Coherencia Optica) han sido estimados experimentalmente en lentes de vidrio.
- El método alcanza la precisión reportada por otros métodos, en la reconstrucción del GRIN.
- Primera reconstrucción de la distribución GRIN en un cristalino porcino utilizando imágenes de OCT.
- Primera medida tridimensional del GRIN, primer reporte de cambios meridionales de la distribución de GRIN.
- Primera estimación directa del papel de la forma de las superficies y del GRIN en la aberración esférica del cristalino y su astigmatismo.
- Primer estudio basado en métodos ópticos de la variación del GRIN con la edad en cristalinos humanos.
- Primera propuesta de un método de corrección de imágenes de OCT del cristalino que involucra un trazado de rayos a través del GRIN

El desarrollo del método de reconstrucción presentado en esta tesis y los resultados experimentales nos permiten concluir que:

1 Es posible reconstruir el GRIN de un cristalino no esférico con métodos de optimización cuando la geometría externa del mismo es conocida. Hemos mostrado, por medio de simulaciones, que diferentes datos experimentales obtenidos con un trazado de rayos o una imagen Tomografía de Coherencia Óptica pueden ser usados para reconstruir el GRIN y que la mejor reconstrucción es obtenida si se utilizan los datos de camino óptico obtenidos de imágenes de OCT (raiz cuadrática media de la diferencia menor que 0.005).

2 El GRIN de un cristalino porcine puede ser reconstruido con el método propuesto en esta tesis utilizando un modelo tridimensional. Los índices de refracción de fase de la superficie y el núcleo para una longitud de onda de 633 nm estimados, fueron 1.354 y 1.434 respectivamente, y el factor de decaimiento exponencial fue 2.6 en eje y variable entre 3.5 y 5.1 en el eje meridional.

3 La presencia de GRIN tiene un impacto en la óptica del cristalino. En particular, el GRIN desplaza la aberración esférica del cristalino de valores positivos (que se obtendrían considerando las mismas superficies y un índice homogéneo) hacia valores negativos. La presencia del GRIN también tiene una influencia en el astigmatismo del cristalino.

4 El GRIN del cristalino humano cambia con la edad. En lentes jóvenes el cambio entre superficie y núcleo es suave mientras en cristalinos mayores este cambio está concentrado en la superficie. Los resultados muestran que, aunque los índices de refracción de la superficie y el núcleo no cambian con la edad, el factor de decaimiento exponencial que describe la forma del perfil aumenta significativamente 0.24 cada año. Los valores promedio de índice de refracción para una longitud de onda de 589 nm fueron 1.373 ± 0.014 y 1.417 ± 0.011.

5 El efecto del GRIN en la distorsión de la superficie posterior observada a través de la anterior en las imágenes de OCT, es relevante principalmente en la periferia del cristalino. La corrección de la distorsión asumiendo un modelo de GRIN mejora los métodos propuestos anteriormente en la literatura, que asumen un índice homogéneo. La precisión en la obtención de la biometría de la superficie posterior del cristalino con imágenes de OCT mejora si el GRIN del cristalino es tenido en cuenta.

Bibliography

Acosta, E., Bueno, J. M., Schwarz, C., and Artal, P. (2010). Relationship between wave aberrations and histological features in ex vivo porcine crystalline lenses. *J Biomed Opt*, 15(5):055001.

Acosta, E., Vazquez, D., Garner, L., and Smith, G. (2005). Tomographic method for measurement of the gradient refractive index of the crystalline lens. I. The spherical fish lens. *J Opt Soc Am A*, 22(3):424–433.

Al-Ahdali, I. H. and El-Messiery, M. A. (1995). Examination of the effect of the fibrous structure of a lens on the optical characteristics of the human eye: a computer-simulated model. *Appl Opt*, 34(25):5738–5745.

Artal, P., Berrio, E., Guirao, A., and Piers, P. (2002). Contribution of the cornea and internal surfaces to the change of ocular aberrations with age. *J Opt Soc Am A*, 19(1):137–143.

Atchison, D. A., Markwell, E. L., Kasthurirangan, S., Pope, J. M., Smith, G., and Swann, P. G. (2008). Age-related changes in optical and biometric characteristics of emmetropic eyes. *J Vis*, 8(4):29.1–2920.

Atchison, D. A. and Smith, G. (1995). Continuous gradient index and shell models of the human lens. *Vision Res*, 35(18):2529–2538.

Atchison, D. A. and Smith, G. (2005). Chromatic dispersions of the ocular media of human eyes. *J Opt Soc Am A*, 22(1):29–37.

Augusteyn, R. C., Jones, C. E., and Pope, J. M. (2008). Age-related development of a refractive index plateau in the human lens: evidence for a distinct nucleus. *Clin Exp Optom*, 91(3):296–301.

Augusteyn, R. C., Rosen, A. M., Borja, D., Ziebarth, N. M., and Parel, J. M. (2006). Biometry of primate lenses during immersion in preservation media. *Mol Vis*, 12:740–747.

Axelrod, D., Lerner, D., and Sands, P. J. (1988). Refractive index within the lens of a goldfish eye determined from the paths of thin laser beams. *Vision Res*, 28(1):57–65.

Baer, E., Hiltner, P. A., and Shirk, J. S. (2006). Multilayer polymer gradient index (GRIN) lenses. U.S. Patent 7002754.

Bahrami, M. and Goncharov, A. V. (2012). Geometry-invariant gradient refractive index lens: analytical ray tracing. *J Biomed Opt*, 17((5)):055001.

Barbero, S., Glasser, A., Clark, C., and Marcos, S. (2004). Accuracy and possibilities for evaluating the lens gradient-index using a ray tracing tomography global optimization strategy. *Invest Ophthalmol Vis Sci*, 45: E–Abstract 1723.

Barbero, S., Marcos, S., and Merayo-Lloves, J. (2002). Corneal and total optical aberrations in a unilateral aphakic patient. *J Cataract Refract Surg*, 28(9):1594–1600.

Barrell, K. and Pask, C. (1978). Nondestructive index profile measurement of non-circular optical fibre preforms. *Optics Communications*, 27(2):230 – 234.

Beadie, G., Shirk, J. S., Rosenberg, A., Lane, P. A., Fleet, E., Kamdar, A. R., Jin, Y., Ponting, M., Kazmierczak, T., Yang, Y., Hiltner, A., and Baer, E. (2008). Optical properties of a bio-inspired gradient refractive index polymer lens. *Opt Express*, 16(15):11540–11547.

Beers, A. P. and van der Heijde, R. G. L. (1996). Age-related changes in the accommodation mechanism. *Optom Vis Sci*, 73(4):235–242.

Beliakov, G. and Chan, D. Y. (1998). Analysis of inhomogeneous optical systems by the use of ray tracing. II. Three-dimensional systems with symmetry. *Appl Opt*, 37(22):5106–5111.

Blaker, J. W. (1980). Toward an adaptive model of the human eye. *J Opt Soc Am*, 70(2):220–223.

Borja, D., Manns, F., Ho, A., Ziebarth, N., Rosen, A. M., Jain, R., Amelinckx, A., Arrieta, E., Augusteyn, R. C., and Parel, J. M. (2008). Optical power of the isolated human crystalline lens. *Invest Ophthalmol Vis Sci*, 49(6):2541–2548.

Borja, D., Siedlecki, D., de Castro, A., Uhlhorn, S., Ortiz, S., Arrieta, E., Parel, J. M., Marcos, S., and Manns, F. (2010). Distortions of the posterior surface in optical coherence tomography images of the isolated crystalline lens: effect of the lens index gradient. *Biomed Opt Express*, 1(5):1331–1340.

Brown, N. (1973a). The change in shape and internal form of the lens of the eye on accommodation. *Exp Eye Res*, 15(4):441–459.

Brown, N. (1973b). Slit-image photography and measurement of the eye. *Med Biol Illus*, 23(4):192–203.

Brown, N. (1974). The change in lens curvature with age. *Exp Eye Res*, 19(2):175–183.

Campbell, C. E. (2010). Nested shell optical model of the lens of the human eye. *J Opt Soc Am A*, 27(11):2432–2441.

Campbell, M. C. (1984). Measurement of refractive index in an intact crystalline lens. *Vision Res*, 24(5):409–415.

Campbell, M. C. and Hughes, A. (1981). An analytic, gradient index schematic lens and eye for the rat which predicts aberrations for finite pupils. *Vision Res*, 21(7):1129–1148.

Chan, D. Y., Ennis, J. P., Pierscionek, B. K., and Smith, G. (1988). Determination and modeling of the 3-D gradient refractive indices in crystalline lenses. *Appl Opt*, 27(5):926–931.

Chossat, M. (1818). Extrait d'un memoire sur le pouvoir réfringent des milieux de l'oeil. *An de Chim et de Phys*, 8:217–223.

Chu, P. (1977). Nondestructive measurement of index profile of an optical-fibre preform. *Electronics Letters*, 13(24):736 –738.

Cook, C. A. and Koretz, J. F. (1998). Methods to obtain quantitative parametric descriptions of the optical surfaces of the human crystalline lens from Scheimpflug slit-lamp images. I. image processing methods. *J Opt Soc Am A*, 15(6):1473–1485.

de Castro, A., Barbero, S., Ortiz, S., and Marcos, S. (2011a). Accuracy of the reconstruction of the crystalline lens gradient index with optimization methods from Ray Tracing and Optical Coherence Tomography data. *Opt Express*, 19(20):19265–19279.

de Castro, A., Ortiz, S., Gambra, E., Siedlecki, D., and Marcos, S. (2010). Three-dimensional reconstruction of the crystalline lens gradient index distribution from oct imaging. *Opt Express*, 18(21):21905–21917.

de Castro, A., Siedlecki, D., Borja, D., Uhlhorn, S., Parel, J. M., Manns, F., and Marcos, S. (2011b). Age-dependent variation of the gradient index profile in human crystalline lenses. *Journal of Modern Optics*, 58(19-20):1781–1787.

Díaz, J., Blazejewski, N., Fernández-Dorado, J., Arasa, J., Sorroche, F., and Pizarro, C. (2011). Analysis of the robustness of the lens grin profile in a schematic model eye. *Journal of Modern Optics*, 58(19-20):1764–1769.

Díaz, J. A., Pizarro, C., and Arasa, J. (2008). Single dispersive gradient-index profile for the aging human lens. *J Opt Soc Am A*, 25(1):250–261.

Dubbelman, M. and van der Heijde, R. G. L. (2001). The shape of the aging human lens: curvature, equivalent refractive index and the lens paradox. *Vision Res*, 41(14):1867–1877.

Dubbelman, M., van der Heijde, R. G. L., and Weeber, H. A. (2001). The thickness

of the aging human lens obtained from corrected Scheimpflug images. *Optom Vis Sci*, 78(6):411–416.

Dubbelman, M., van der Heijde, R. G. L., and Weeber, H. A. (2005a). Change in shape of the aging human crystalline lens with accommodation. *Vision Res*, 45(1):117–132.

Dubbelman, M., van der Heijde, R. G. L., and Weeber, H. A. (2005b). Comment on "Scheimpflug and high-resolution magnetic resonance imaging of the anterior segment: a comparative study". *J Opt Soc Am A*, 22(6):1216–8; discussion 1219–20.

Dubbelman, M., van der Heijde, R. G. L., Weeber, H. A., and Vrensen, G. F. J. M. (2003). Changes in the internal structure of the human crystalline lens with age and accommodation. *Vision Res*, 43(22):2363–2375.

Dunne, M. C. M., Davies, L. N., and Wolffsohn, J. S. (2007). Accuracy of cornea and lens biometry using anterior segment optical coherence tomography. *J Biomed Opt*, 12(6):064023.

El-Hage, S. G. and Berny, F. (1973). Contribution of the crystalline lens to the spherical aberration of the eye. *J Opt Soc Am*, 63(2):205–211.

Escudero-Sanz, I. and Navarro, R. (1999). Off-axis aberrations of a wide-angle schematic eye model. *J Opt Soc Am A*, 16(8):1881–1891.

Fagerholm, P. P., Philipson, B. T., and Lindström, B. (1981). Normal human lens - the distribution of protein. *Exp Eye Res*, 33(6):615–620.

Flores-Arias, M. T., del Rio, A. D., Bao-Varela, C., Pérez, M. V., and Gómez-Reino, C. (2009). Description of gradient-index human eye by a first-order optical system. *J Opt A*, 11(12):125301.

Flores-Arias, M. T., Perez, M. V., Bao, C., Castelo, A., and Gomez-Reino, C. (2006). Gradient-index human lens as a quadratic phase transformer. *Journal of Modern Optics*, 53(4):495–506.

Gambra, E., Ortiz, S., Pérez-Merino, P., Gora, M., Wojtkowski, M., and Marcos, S. (2010). Quantitative 3D-imaging of the in vivo crystalline lens during accommodation. *Invest Ophthalmol Vis Sci*, 51: E–Abstract 5787.

Garner, L. F. (1997). Calculation of the radii of curvature of the crystalline lens surfaces. *Ophthalmic Physiol Opt*, 17(1):75–80.

Garner, L. F., Ooi, C. S., and Smith, G. (1998). Refractive index of the crystalline lens in young and aged eyes. *Clin Exp Optom*, 81(4):145–150.

Garner, L. F. and Smith, G. (1997). Changes in equivalent and gradient refractive index of the crystalline lens with accommodation. *Optom Vis Sci*, 74(2):114–119.

Garner, L. F., Smith, G., Yao, S., and Augusteyn, R. C. (2001). Gradient refractive

index of the crystalline lens of the Black Oreo Dory (Allocyttus Niger): comparison of magnetic resonance imaging (MRI) and laser ray-trace methods. *Vision Res*, 41(8):973–979.

Glasser, A. and Campbell, M. C. (1998). Presbyopia and the optical changes in the human crystalline lens with age. *Vision Res*, 38(2):209–229.

Glasser, A. and Campbell, M. C. (1999). Biometric, optical and physical changes in the isolated human crystalline lens with age in relation to presbyopia. *Vision Res*, 39(11):1991–2015.

Goldsmith, J. A., Li, Y., Chalita, M. R., Westphal, V., Patil, C. A., Rollins, A. M., Izatt, J. A., and Huang, D. (2005). Anterior chamber width measurement by high-speed optical coherence tomography. *Ophthalmology*, 112(2):238–244.

Goncharov, A. V., Burvall, A., and Dainty, C. (2007). Systematic design of an anastigmatic lens axicon. *Appl Opt*, 46(24):6076–6080.

Goncharov, A. V. and Dainty, C. (2007). Wide-field schematic eye models with gradient-index lens. *J Opt Soc Am A*, 24(8):2157–2174.

Goncharov, A. V., Nowakowski, M., Sheehan, M. T., and Dainty, C. (2008). Reconstruction of the optical system of the human eye with reverse ray-tracing. *Opt Express*, 16(3):1692–1703.

Grulkowski, I., Gora, M., Szkulmowski, M., Gorczynska, I., Szlag, D., Marcos, S., Kowalczyk, A., and Wojtkowski, M. (2009). Anterior segment imaging with spectral oct system using a high-speed cmos camera. *Opt Express*, 17(6):4842–4858.

Hamblen, D. P. (1992). Intraocular gradient-index lenses used in eye implantation. U.S. Patent 5152787.

Hauksbee, F. (1710). A description of the apparatus for making experiments on the refractions of fluids: With a table of the specifick gravities, angles of observations, and ratio of refractions of several fluids. *Phil Trans*, 27:204–207.

Helmholtz (1924). *Treatise on Physiological Optics*. The Optical Society of America (translated from Third German Edition by J. P. C. Southall).

Hemenger, R. P., Garner, L. F., and Ooi, C. S. (1995). Change with age of the refractive index gradient of the human ocular lens. *Invest Ophthalmol Vis Sci*, 36(3):703–707.

Hemenger, R. P., Tomlinson, A., and McDonnell, P. J. (1990). Explanation for good visual acuity in uncorrected residual hyperopia and presbyopia after radial keratotomy. *Invest Ophthalmol Vis Sci*, 31(8):1644–1646.

Hermans, E. A., Dubbelman, M., van der Heijde, R. G. L., and Heethaar, R. M. (2008). Equivalent refractive index of the human lens upon accommodative response. *Optom Vis Sci*, 85(12):1179–1184.

Hewak, D. W. and Lit, J. W. Y. (1985). Numerical ray-tracing methods for gradient

index media. *Canadian Journal of Physics*, 63(2):234–239.

Holland, J. H. (1975). *Adaptation in Natural and Artificial Systems*. Ann Arbor: Universtiy of Michigan Press.

Hoshino, M., Uesugi, K., Yagi, N., and Mohri, S. (2010). Investigation of imaging properties of mouse eyes using x-ray phase contrast tomography. *AIP Conference Proceedings*, 1266(1):57–61.

Hoshino, M., Uesugi, K., Yagi, N., Mohri, S., Regini, J., and Pierscionek, B. (2011). Optical properties of in situ eye lenses measured with x-ray talbot interferometry: a novel measure of growth processes. *PLoS One*, 6(9):e25140.

Howcroft, M. J. and Parker, J. A. (1977). Aspheric curvatures for the human lens. *Vision Res*, 17(10):1217–1223.

Huggert, A. (1948). *On the form of the iso-indicial surfaces of the human crystalline lens*. Acta Ophthalmologica supplementum.

Jagger, W. S. (1990). The refractive structure and optical properties of the isolated crystalline lens of the cat. *Vision Res*, 30(5):723–738.

Jagger, W. S. (1992). The optics of the spherical fish lens. *Vision Res*, 32(7):1271–1284.

Jenkins, T. C. (1963). Aberrations of the eye and their effects on vision: part 1. *Br J Physiol Opt*, 20:59–91.

Jones, C. E., Atchison, D. A., Meder, R., and Pope, J. M. (2005). Refractive index distribution and optical properties of the isolated human lens measured using magnetic resonance imaging (MRI). *Vision Res*, 45(18):2352–2366.

Kasthurirangan, S., Markwell, E. L., Atchison, D. A., and Pope, J. M. (2008). In vivo study of changes in refractive index distribution in the human crystalline lens with age and accommodation. *Invest Ophthalmol Vis Sci*, 49(6):2531–2540.

Kim, E., Ehrmann, K., Uhlhorn, S., Borja, D., Arrieta-Quintero, E., and Parel, J. M. (2011). Semiautomated analysis of optical coherence tomography crystalline lens images under simulated accommodation. *J Biomed Opt*, 16(5):056003.

Kim, E., Ehrmann, K., Uhlhorn, S., Borja, D., and Parel, J. M. (2009). Automated analysis of oct images of the crystalline lens. In Manns, F., editor, *Ophthalmic Technologies XIX*, volume 7163. Proc. of SPIE.

Koretz, J. E., Strenk, S. A., Strenk, L. M., and Semmlow, J. L. (2004). Scheimpflug and high-resolution magnetic resonance imaging of the anterior segment: a comparative study. *J Opt Soc Am A*, 21(3):346–354.

Koretz, J. F., Cook, C. A., and Kaufman, P. L. (1997). Accommodation and presbyopia in the human eye. changes in the anterior segment and crystalline lens with focus. *Invest Ophthalmol Vis Sci*, 38(3):569–578.

Koretz, J. F., Cook, C. A., and Kaufman, P. L. (2001). Aging of the human lens: changes in lens shape at zero-diopter accommodation. *J Opt Soc Am A*, 18(2):265–272.

Koretz, J. F., Cook, C. A., and Kaufman, P. L. (2002). Aging of the human lens: changes in lens shape upon accommodation and with accommodative loss. *J Opt Soc Am A*, 19(1):144–151.

Koretz, J. F. and Handelman, G. H. (1986). Modeling age-related accomodative loss in the human eye. *Int J Math Modelling*, 7(5-8):1003 – 1014.

Koretz, J. F., Handelman, G. H., and Brown, N. P. (1984). Analysis of human crystalline lens curvature as a function of accommodative state and age. *Vision Res*, 24(10):1141–1151.

Lagarias, J. C., Reeds, J. A., Wright, M. H., and Wright, P. E. (1998). Convergence properties of the nelder-mead simplex method in low dimensions. *SIAM J Optim*, 9(1):112–47.

Le-Grand, Y. (1964). *Óptica Fisiológica. Tomo III. El espacio visual*. (translated by Sociedad Española de Optometría, 1995).

Lehman, B. M., Berntsen, D. A., Bailey, M. D., and Zadnik, K. (2009). Validation of optical coherence tomography-based crystalline lens thickness measurements in children. *Optom Vis Sci*, 86(3):181–187.

Liou, H. L. and Brennan, N. A. (1997). Anatomically accurate, finite model eye for optical modeling. *J Opt Soc Am A*, 14(8):1684–1695.

Maceo, B. M., Manns, F., Borja, D., Nankivil, D., Uhlhorn, S., Arrieta, E., Ho, A., Augusteyn, R. C., and Parel, J. M. (2011). Contribution of the crystalline lens gradient refractive index to the accommodation amplitude in non-human primates: In vitro studies. *Journal of Vision*, 11(13).

Manns, F., Fernandez, V., Zipper, S., Sandadi, S., Hamaoui, M., Ho, A., and Parel, J. M. (2004). Radius of curvature and asphericity of the anterior and posterior surface of human cadaver crystalline lenses. *Exp Eye Res*, 78(1):39–51.

Manns, F., Ho, A., Borja, D., and Parel, J. M. (2010). Comparison of uniform and gradient paraxial models of the crystalline lens. *Invest Ophthalmol Vis Sci*, 51: E–Abstract 789.

Manns, F., Parel, J. M., Denham, D., Billotte, C., Ziebarth, N., Borja, D., Fernandez, V., Aly, M., Arrieta, E., Ho, A., and Holden, B. (2007). Optomechanical response of human and monkey lenses in a lens stretcher. *Invest Ophthalmol Vis Sci*, 48(7):3260–3268.

Millodot, M. and Sivak, J. (1979). Contribution of the cornea and lens to the spherical aberration of the eye. *Vision Res*, 19(6):685–687.

Moffat, B. A., Atchison, D. A., and Pope, J. M. (2002a). Age-related changes in refractive index distribution and power of the human lens as measured by magnetic resonance micro-imaging in vitro. *Vision Res*, 42(13):1683–1693.

Moffat, B. A., Atchison, D. A., and Pope, J. M. (2002b). Explanation of the lens paradox. *Optom Vis Sci*, 79(3):148–150.

Moffat, B. A. and Pope, J. M. (2002a). Anisotropic water transport in the human eye lens studied by diffusion tensor NMR micro-imaging. *Exp Eye Res*, 74(6):677–687.

Moffat, B. A. and Pope, J. M. (2002b). The interpretation of multi-exponential water proton transverse relaxation in the human and porcine eye lens. *Magn Reson Imaging*, 20(1):83–93.

Moreno-Barriuso, E., Marcos, S., Navarro, R., and Burns, S. A. (2001). Comparing laser ray tracing, the spatially resolved refractometer, and the Hartmann-Shack sensor to measure the ocular wave aberration. *Optom Vis Sci*, 78(3):152–156.

Moreno-Barriuso, E. and Navarro, R. (2000). Laser Ray Tracing versus Hartmann-Shack sensor for measuring optical aberrations in the human eye. *J Opt Soc Am A*, 17(6):974–985.

Mutti, D. O., Zadnik, K., and Adams, A. J. (1992). A video technique for phakometry of the human crystalline lens. *Invest Ophthalmol Vis Sci*, 33(5):1771–1782.

Nakao, S., Fujimoto, S., Nagata, R., and Iwata, K. (1968). Model of refractive-index distribution in the rabbit crystalline lens. *J Opt Soc Am*, 58(8):1125–1130.

Nakao, S., Ono, T., Nagata, R., and Iwata, K. (1969). Model of refractive indices in the human crystalline lens. *Jpn J Clin Ophthalmol*, 23:903–906.

Navarro, R., Palos, F., and González, L. M. (2007a). Adaptive model of the gradient index of the human lens. I. Formulation and model of aging ex vivo lenses. *J Opt Soc Am A*, 24(8):2175–2185.

Navarro, R., Palos, F., and González, L. M. (2007b). Adaptive model of the gradient index of the human lens. II. Optics of the accommodating aging lens. *J Opt Soc Am A*, 24(9):2911–2920.

Navarro, R., Santamaría, J., and Bescós, J. (1985). Accommodation-dependent model of the human eye with aspherics. *J Opt Soc Am A*, 2(8):1273–1281.

Nelder, J. A. and Mead, R. (1965). A simplex method for function minimization. *The Computer Journal*, 7(4):308–313.

Ortiz, S., Barbero, S., and Marcos, S. (2004). Computer simulations of optical coherence tomography a-scans: what can we learn about refractive index distribution? *Invest Ophthalmol Vis Sci*, 45: E–Abstract 2781.

Ortiz, S., Siedlecki, D., Grulkowski, I., Remon, L., Pascual, D., Wojtkowski, M., and Marcos, S. (2010). Optical distortion correction in optical coherence tomography

for quantitative ocular anterior segment by three-dimensional imaging. *Opt Express*, 18(3):2782–2796.

Ortiz, S., Siedlecki, D., Pérez-Merino, P., Chia, N., de Castro, A., Szkulmowski, M., Wojtkowski, M., and Marcos, S. (2011). Corneal topography from spectral optical coherence tomography (sOCT). *Biomed Opt Express*, 2(12):3232–3247.

Ortiz, S., Siedlecki, D., Remon, L., and Marcos, S. (2009). Optical coherence tomography for quantitative surface topography. *Appl Opt*, 48(35):6708–6715.

Palmer, D. A. and Sivak, J. (1981). Crystalline lens dispersion. *J Opt Soc Am*, 71(6):780–782.

Parker, J. A. (1972). Aspheric optics of the human lens. *Can J Ophthalmol*, 7(2):168–175.

Philipson, B. (1969). Distribution of protein within the normal rat lens. *Invest Ophthalmol*, 8(3):258–270.

Phillips, P., Pérez-Emmanuelli, J., Rosskothen, H. D., and Koester, C. J. (1988). Measurement of intraocular lens decentration and tilt in vivo. *J Cataract Refract Surg*, 14(2):129–135.

Pierscionek, B., Smith, G., and Augusteyn, R. C. (1987). The refractive increments of bovine alpha-, beta-, and gamma-crystallins. *Vision Res*, 27(9):1539–1541.

Pierscionek, B. K. (1990). Presbyopia - effect of refractive index. *Clin Exp Optom*, 73(1):23–30.

Pierscionek, B. K. (1993). Surface refractive index of the eye lens determined with an optic fiber sensor. *J Opt Soc Am A*, 10(9):1867–1871.

Pierscionek, B. K. (1994a). Refractive index of decapsulated bovine lens surfaces measured with a reflectometric sensor. *Vision Res*, 34(15):1927–1933.

Pierscionek, B. K. (1994b). Refractive index of the human lens surface measured with an optic fibre sensor. *Ophthalmic Res*, 26(1):32–35.

Pierscionek, B. K. (1997). Refractive index contours in the human lens. *Exp Eye Res*, 64(6):887–893.

Pierscionek, B. K. and Augusteyn, R. C. (1991). Shapes and dimensions of in vitro human lenses. *Clin Exp Optom*, 74(6):223–228.

Pierscionek, B. K., Belaidi, A., and Bruun, H. H. (2005). Refractive index distribution in the porcine eye lens for 532 nm and 633 nm light. *Eye (Lond)*, 19(4):375–381.

Pierscionek, B. K. and Chan, D. Y. (1989). Refractive index gradient of human lenses. *Optom Vis Sci*, 66(12):822–829.

Pierscionek, B. K., Chan, D. Y., Ennis, J. P., Smith, G., and Augusteyn, R. C. (1988). Nondestructive method of constructing three-dimensional gradient index mod-

els for crystalline lenses: I. Theory and experiment. *Am J Optom Physiol Opt*, 65(6):481–491.

Podoleanu, A., Charalambous, I., Plesea, L., Dogariu, A., and Rosen, R. (2004). Correction of distortions in optical coherence tomography imaging of the eye. *Phys Med Biol*, 49(7):1277–1294.

Polack, A. (1923). *Le chromatisme de l'oeil*. Société l'ophtalmologie de Paris.

Pomerantzeff, O., Fish, H., Govignon, J., and Schepens, C. L. (1971). Wide angle optical model of the human eye. *Ann Ophthalmol*, 3(8):815–819.

Pomerantzeff, O., Fish, H., Govignon, J., and Schepens, C. L. (1972). Wide-angle optical model of the eye. *Journal of Modern Optics*, 19(5):387–8.

Pope, J. M., Atchison, D. A., and Jones, C. E. (2008). To the editor: Changes in lens dimensions and refractive index with age and accommodation: Authors' reply. *Opt Vis Sci*, 85(4).

Popiolek-Masajada, A. (1999). Numerical study of the influence of the shell structure of the crystalline lens on the refractive properties of the human eye. *Ophthalmic Physiol Opt*, 19(1):41–49.

Pérez, M. V., Bao, C., Flores-Arias, M. T., Rama, M. A., and Gómez-Reino, C. (2003). Gradient parameter and axial and field rays in the gradient-index crystalline lens model. *J Opt A*, 5(5):S293.

Pérez, M. V., Bao, C., Flores-Arias, M. T., Rama, M. A., and Gómez-Reino, C. (2005). Description of gradient-index crystalline lens by a first-order optical system. *J Opt A*, 7(3):103.

Pérez-Escudero, A., Dorronsoro, C., and Marcos, S. (2010). Correlation between radius and asphericity in surfaces fitted by conics. *J Opt Soc Am A*, 27(7):1541–1548.

Rama, M. A., Pérez, M. V., Bao, C., Flores-Arias, M. T., and Gómez-Reino, C. (2005). Gradient-index crystalline lens model: A new method for determining the paraxial properties by the axial and field rays. *Optics Communications*, 249(4-6):595 – 609.

Reiß, S., Burau, G., Stachs, O., Guthoff, R., and Stolz, H. (2011). Spatially resolved brillouin spectroscopy to determine the rheological properties of the eye lens. *Biomed Opt Express*, 2(8):2144–2159.

Roffman, J. H., Molock, F. F., and Hill, G. A. (2004). Intraocular lenses and methods for their manufacture. U.S. Patent 6695880.

Roorda, A. and Glasser, A. (2004). Wave aberrations of the isolated crystalline lens. *J Vis*, 4(4):250–261.

Rosales, P., Dubbelman, M., Marcos, S., and van der Heijde, R. G. L. (2006). Crys-

talline lens radii of curvature from Purkinje and Scheimpflug imaging. *J Vis*, 6(10):1057–1067.

Rosales, P. and Marcos, S. (2006). Phakometry and lens tilt and decentration using a custom-developed Purkinje imaging apparatus: validation and measurements. *J Opt Soc Am A*, 23(3):509–520.

Rosales, P. and Marcos, S. (2009). Pentacam Scheimpflug quantitative imaging of the crystalline lens and intraocular lens. *J Refract Surg*, 25(5):421–428.

Rosales, P., Wendt, M., Marcos, S., and Glasser, A. (2008). Changes in crystalline lens radii of curvature and lens tilt and decentration during dynamic accommodation in rhesus monkeys. *J Vis*, 8(1):18.1–1812.

Rosen, A. M., Denham, D. B., Fernandez, V., Borja, D., Ho, A., Manns, F., Parel, J. M., and Augusteyn, R. C. (2006). In vitro dimensions and curvatures of human lenses. *Vision Res*, 46(6-7):1002–1009.

Saleh, B. E. A. and Teich, M. C. (1991). *Fundamentals of photonics.* New York: John Wiley & Sons.

Sands, P. J. (1970). Third-order aberrations of inhomogeneous lenses. *J Opt Soc Am*, 60(11):1436–1443.

Scarcelli, G. and Yun, S. H. (2012). In vivo brillouin optical microscopy of the human eye. *Opt Express*, 20(8):9197–9202.

Sharma, A. and Ghatak, A. K. (1986). Ray tracing in gradient-index lenses: computation of ray-surface intersection. *Appl Opt*, 25(19):3409–3412.

Sharma, A., Kumar, D. V., and Ghatak, A. K. (1982). Tracing rays through graded-index media: a new method. *Appl Opt*, 21(6):984–987.

Shinoda, G., Suzuki, T., Nakatani, N., and Nagata, R. (1964). Strain measurement by double diffraction method. *Japan J Appl Phys*, 3(10):633–634.

Siedlecki, D., de Castro, A., Gambra, E., Ortiz, S., Borja, D., Uhlhorn, S., Manns, F., Marcos, S., and Parel, J. M. (2012). Distortion correction of OCT images of the crystalline lens: Gradient index approach. *Optom Vis Sci*, 89(5):709–718.

Siedlecki, D., Kasprzak, H., and Pierscionek, B. K. (2004). Schematic eye with a gradient-index lens and aspheric surfaces. *Opt Lett*, 29(11):1197–1199.

Silverman, R. H. (2009). High-resolution ultrasound imaging of the eye - a review. *Clin Exp Ophthalmol*, 37(1):54–67.

Sivak, J. G. and Kreuzer, R. O. (1983). Spherical aberration of the crystalline lens. *Vision Res*, 23(1):59–70.

Sivak, J. G. and Mandelman, T. (1982). Chromatic dispersion of the ocular media. *Vision Res*, 22(8):997–1003.

Smith, G. and Atchison, D. A. (2001). The gradient index and spherical aberration of the lens of the human eye. *Ophthalmic Physiol Opt*, 21(4):317–326.

Smith, G., Atchison, D. A., and Pierscionek, B. K. (1992). Modeling the power of the aging human eye. *J Opt Soc Am A*, 9(12):2111–2117.

Smith, G., Bedggood, P., Ashman, R., Daaboul, M., and Metha, A. (2008). Exploring ocular aberrations with a schematic human eye model. *Opt Vis Sci*, 85(5):330–340.

Smith, G., Cox, M. J., Calver, R., and Garner, L. F. (2001). The spherical aberration of the crystalline lens of the human eye. *Vision Res*, 41(2):235–243.

Smith, G. and Garner, L. F. (1996). Determination of the radius of curvature of the anterior lens surface from the Purkinje images. *Ophthalmic Physiol Opt*, 16(2):135–143.

Smith, G., Pierscionek, B. K., and Atchison, D. A. (1991). The optical modelling of the human lens. *Ophthalmic Physiol Opt*, 11(4):359–369.

Sorsby, A., Benjamin, B., Sheridan, M., Stone, J., and Leary, G. A. (1961). Refraction and its components during the growth of the eye from the age of three. *Memo Med Res Counc*, 301(Special):1–67.

Stavroudis, O. O. (1972). *The optics of rays, wavefrons and caustics*. New York Academic Press.

Stone, B. D. and Forbes, G. W. (1990). Optimal interpolants for runge-kutta ray tracing in inhomogeneous media. *J Opt Soc Am A*, 7(2):248–254.

Tabernero, J., Benito, A., Nourrit, V., and Artal, P. (2006). Instrument for measuring the misalignments of ocular surfaces. *Opt Express*, 14(22):10945–10956.

Thibos, L. N., Ye, M., Zhang, X., and Bradley, A. (1997). Spherical aberration of the reduced schematic eye with elliptical refracting surface. *Optom Vis Sci*, 74(7):548–556.

Tomlinson, A., Hemenger, R. P., and Garriott, R. (1993). Method for estimating the spheric aberration of the human crystalline lens in vivo. *Invest Ophthalmol Vis Sci*, 34(3):621–629.

Ueberhuber, C. W. (1997). *Numerical Computation 2: Methods, Software, and Analysis.* Berlin: Springer-Verlag.

Uhlhorn, S. R., Borja, D., Manns, F., and Parel, J. M. (2008). Refractive index measurement of the isolated crystalline lens using optical coherence tomography. *Vision Res*, 48(27):2732–2738.

Urs, R., Ho, A., Manns, F., and Parel, J. M. (2010). Age-dependent fourier model of the shape of the isolated ex vivo human crystalline lens. *Vision Res*, 50(11):1041–1047.

Urs, R., Manns, F., Ho, A., Borja, D., Amelinckx, A., Smith, J., Jain, R., Augusteyn, R., and Parel, J. M. (2009). Shape of the isolated ex-vivo human crystalline lens. *Vision Res*, 49(1):74–83.

Vasiljević, D. (2002). *Classical and evolutionary algorithms in the optimization of optical systems*. Kluwer Academic Publishers Boston/Dordrecht/London.

Vazquez, D. (2007). *Tomographic reconstruction of the gradient indices with rotational symmetry. Application to crystalline lenses.* PhD thesis, Universidad de Santiago de Compostela.

Vazquez, D., Acosta, E., Smith, G., and Garner, L. (2006). Tomographic method for measurement of the gradient refractive index of the crystalline lens. II. The rotationally symmetrical lens. *J Opt Soc Am A*, 23(10):2551–2565.

Veen, H. G. V. and Goss, D. A. (1988). Simplified system of Purkinje image photography for phakometry. *Am J Optom Physiol Opt*, 65(11):905–908.

Verma, Y., Rao, K., Suresh, M., Patel, H., and Gupta, P. (2007). Measurement of gradient refractive index profile of crystalline lens of fisheye in vivo using optical coherence tomography. *Appl Phys B*, 87:607–610.

Vilupuru, A. S. and Glasser, A. (2001). Optical and biometric relationships of the isolated pig crystalline lens. *Ophthalmic Physiol Opt*, 21(4):296–311.

Wade, N. J. (1998). *A natural history of vision*. Cambridge, MA: MIT Press.

Wang, X., Zhang, C., Zhang, L., Xue, L., and Tian, J. (2002). Simultaneous refractive index and thickness measurements of bio tissue by optical coherence tomography. *J Biomed Opt*, 7(4):628–632.

Westphal, V., Rollins, A., Radhakrishnan, S., and Izatt, J. (2002). Correction of geometric and refractive image distortions in optical coherence tomography applying fermat's principle. *Opt Express*, 10(9):397–404.

Wintringham, C. (1740). *An experimental inquiry on some parts of the animal structure*.

Wong, K.-H., Koopmans, S. A., Terwee, T., and Kooijman, A. C. (2007). Changes in spherical aberration after lens refilling with a silicone oil. *Invest Ophthalmol Vis Sci*, 48(3):1261–1267.

Wulfeck, J. W. (1955). Infrared photography of the so-called third Purkinje image. *J Opt Soc Am*, 45(11):928–930.

Young, T. (1801). *On the mechanism of the eye*. Philos Trans Royal Soc.

Zawadzki, R. J., Leisser, C., Leitgeb, R., Pircher, M., and Fercher, A. F. (2003). Three-dimensional ophthalmic optical coherence tomography with a refraction correction algorithm. In *Optical Coherence Tomography and Coherence Techniques*.

Publications during this research

SCIENTIFIC PAPERS ASSOCIATED WITH THIS THESIS

1. A. de Castro, S. Ortiz, E. Gambra, D. Siedlecki & S. Marcos, "Three-dimensional reconstruction of the crystalline lens gradient index distribution from OCT imaging". *Opt Express*, 18(21): 21905-17, 2010.
2. D. Borja, D. Siedlecki, A. de Castro, S. Uhlhorn, S. Ortiz, E. Arrieta, J.M. Parel, S. Marcos & F. Manns, "Distortions of the posterior surface in optical coherence tomography images of the isolated crystalline lens: effect of the lens index gradient". *Biomed Opt Express*, 1: 1331-40, 2010.
3. A. de Castro, D. Siedlecki, D. Borja, S. Uhlhorn, J.M. Parel, F. Manns & S. Marcos, "Age-dependent variation of the gradient index profile in human crystalline lenses", *Journal of Modern Optics*, 58(19-20): 1781-7, 2011.
4. A. de Castro, S. Barbero, S. Ortiz & S. Marcos, "Accuracy of the reconstruction of the crystalline lens gradient index with optimization methods from Ray Tracing and Optical Coherence Tomography data", *Opt Express*, 19(20): 19265-79, 2011.
5. D. Siedlecki, A. de Castro, E. Gambra, S. Ortiz, D. Borja, S. Uhlhorn, F. Manns, J.M. Parel & S. Marcos, "Distortion correction of OCT images of the crystalline lens: GRIN approach", *Optometry Vision Sci*, 89(5): 709-18, 2012.

OTHER PUBLICATIONS

1. A. de Castro, P. Rosales & S. Marcos, "Tilt and decentration of intraocular lenses in vivo from Purkinje and Scheimpflug imaging. Validation study". *J Cataract Refr Surg*, 33: 418-29, 2007.
2. E. García de la Cera, G. Rodríguez, A. de Castro, J. Merayo & S. Marcos, "Emmetropization and optical aberrations in a myopic corneal refractive surgery chick model". *Vision Res*, 47: 2465-72, 2007.
3. P. Rosales, A. de Castro, I. Jiménez-Alfaro & S. Marcos, "Intraocular lens alignment from Purkinje and Scheimpflug imaging". *Clin Exp Optom*, invited review, 93(6); 400-8, 2010.
4. S. Ortiz, D. Siedlecki, P. Pérez-Merino, N. Chia, A. de Castro, M. Szkulmowski, M. Wojtkowski & S. Marcos, "Corneal topography from spectral Optical Coherence Tomography (sOCT)", *Biomed Opt Express*, 2(12): 3232-47, 2011.

INTERNATIONAL CONGRESS CONTRIBUTIONS

Personally presented

1. A. de Castro, P. Rosales & S. Marcos, "Crystalline And Intraocular Lens Tilt And Decentration Measured With Scheimpflug Imaging: Experimental Validations". Association for Research in Vision and Ophthalmology's Annual Meeting, poster presentation. IOVS 47: E-Abstract 323. Fort Lauderdale, FL, USA, 2006.
2. A. de Castro, S. Barbero & S. Marcos, "A Reconstruction Technique to Estimate the Gradient-Index Distribution of the Crystalline Lens Using Ray Aberration Data in vivo". Association for Research in Vision and Ophthalmology's Annual Meeting, poster presentation. IOVS 48: E-Abstract 3818. Fort Lauderdale, FL, USA, 2007.
3. A. de Castro, D. Borja, S. Uhlhorn, F. Manns, S. Barbero, J.M. Parel & S. Marcos, "Relative Contribution of Gradient Index Distribution and Surface Geometry to Spherical Aberration in Isolated Primate Crystalline Lenses". Association for Research in Vision and Ophthalmology's Annual Meeting, poster presentation. IOVS 49: E-Abstract 3773. Fort Lauderdale, FL, USA, 2008.
4. A. de Castro, S. Ortiz, E. Gambra, D. Siedlecki & S. Marcos, "Three-dimensional reconstruction of the gradient refractive index of the crystalline lens in vitro from OCT images". 5th European Meeting on Visual And Physiological Optics (EMVPO), oral presentation. Stockholm, Sweden, 2010.

5. A. de Castro, S. Barbero, D. Siedlecki, S. Ortiz, D. Borja, S. Uhlhorn, J.M. Parel, F. Manns & S. Marcos, "Reconstruction of the gradient index of the crystalline lens with optimization techniques." IONS-11 (11th meeting of the International OSA Network of Students), poster presentation, Paris, France, 2012.

Presented by collaborators

1. D. Borja, S. Uhlhorn, K. Ehrmann, A. de Castro, E. Arrieta-Quintero, A. Amelinckx, D. Nankivil, A. Ho, F. Manns & J.M. Parel, "Flattening of the Non-Human Primate Crystalline Lens Surfaces During Simulated Accommodation". Association for Research in Vision and Ophthalmology's Annual Meeting, poster presentation. IOVS 49: E-Abstract 4564. Fort Lauderdale, FL, USA, 2008.
2. S. Marcos, S. Barbero, P. Rosales, A. de Castro, L. Llorente, C. Dorronsoro & I. Jiménez-Alfaro, "Performance of aspherical IOLs". Frontiers in Optics, oral presentation. Rochester, USA, 2010.
3. S. Ortiz, P. Pérez-Merino, E. Gambra, S. Kling, A. de Castro, D. Pascual, I. Grulkwoski, M. Gora, M. Wojtkowski & S. Marcos, "Quantitative three-dimensional anterior segment Imaging optical coherente tomography: developments and applications". 5th European Meeting on Visual and Physiological Optics (EMVPO), oral presentation. Stockholm, Sweden, 2010.
4. D. Siedlecki, A. de Castro, S. Ortiz, D. Borja, S. Uhlhorn, F. Manns & S. Marcos, "Estimation of the contribution of the gradient index structure to the posterior surface optical distortion in excised human crystalline lens imaged by optical coherence tomography". 5th European Meeting on Visual and Physiological Optics (EMVPO), oral presentation. Stockholm, Sweden, 2010.
5. P. Pérez-Merino, S. Ortiz, N. Alejandre, A. de Castro, I. Jiménez-Alfaro & S. Marcos, "Full OCT corneal topography and aberrations in keratoconic patients and their change after intrastromal corneal ring segments (ICRS) implantation". Association for Research in Vision and Ophthalmology's Annual Meeting, poster presentation. IOVS 52: E-Abstract 4181. Fort Lauderdale, FL, USA, 2011.
6. J. Birkenfeld, A. de Castro, S. Ortiz, P. Pérez-Merino, E. Gambra & S. Marcos, "Three-dimensional reconstruction of the isolated human crystalline lens gradient index distribution". Association for Research in Vision and Ophthalmology's Annual Meeting, oral presentation.

IOVS 52: E-Abstract 3404. Fort Lauderdale, FL, USA, 2011.

7. S. Marcos, A. de Castro, E. Gambra, J. Birkenfeld, S. Ortiz, P. Pérez-Merino & C. Dorronsoro, "Ocular imaging and crystalline lens optical properties". Frontiers in Optics, invited oral presentation. San José, CA, USA, 2011.
8. P. Pérez-Merino, S. Ortiz, N. Alejandre, A. de Castro, I. Jiménez-Alfaro & S. Marcos, "Assesing corneal geometrical and optical changes on ICRS-treated corneas with quantitative OCT". Eurokeratoconus II, poster presentation. Bordeaux, France, 2011.
9. J. Birkenfeld, A. de Castro, S. Ortiz, P. Pérez-Merino, E. Gambra, D. Pascual & S. Marcos, "Role of lens surface and gradient index for spherical aberration in mammal lenses". IONS-11 (11^{th} meeting of the International OSA Network of Students), oral presentation. París, France. 2011.
10. P. Pérez-Merino, S. Ortiz, N. Alejandre, A. de Castro, I. Jiménez-Alfaro, S. Marcos, "OCT-based topography corneal aberrations and ray tracing total aberrations in kratoconus before and after intracorneal ring treatment." Association for Research in Vision and Ophthalmology's Annual Meeting, poster presentation. Fort Lauderdale, FL, USA, 2012.
11. J. Birkenfeld, A. de Castro, S. Ortiz, P. Pérez-Merino, E. Gambra, D. Pascual & S. Marcos, "Relative contribution of the crystalline lens surface shape and gradient index distribution to spherical aberration". Association for Research in Vision and Ophthalmology's Annual Meeting, oral presentation. Fort Lauderdale, FL, USA, 2012.
12. J. Birkenfeld, A. de Castro, B. Maceo, E. Arrieta, F. Manns, J.M. Parel& S. Marcos, "Change in the gradient refractive index of Cynomolgus monkey lenses with simulated accommodation". Accommodation club, Miami, FL, USA, 2012.

PUBLICATIONS IN PROCEEDINGS

1. S. Marcos, S. Barbero, P. Rosales, A. de Castro, L. Llorente, C. Dorronsoro & I. Jiménez-Alfaro, "Performance of Aspheric IOLs". Frontiers in Optics, OSA Technical Digest (CD), Optical Society of America, 2010.
2. S. Marcos, A. de Castro, E. Gambra, J. Birkenfeld, S. Ortiz, P. Pérez-Merino & C. Dorronsoro, "Ocular imaging and crystalline lens optical properties". Frontiers in Optics, OSA Technical Digest (CD), Optical Society of America, 2011.

BOOK CHAPTERS

1. S. Marcos, P. Rosales, A. de Castro & I. Jiménez-Alfaro, "Effect of IOL tilt and astigmatism", IOL power, Chapter 40, p 223-230. Kenneth Hoffer, Slack 2011.

Acknowledgments

The moment that for a long time seemed to move away has been approaching these last months little by little, arriving quietly. The work of all these years at Susana Marcos' laboratory in the Institute of Optics has been finally compiled, and the result is in your hands now. Thank you Susana for all this time working in your lab while seeing the group grow. Your ability to make numeric data talk, to later compile the results in one single coherent idea, as well as your constant effort day and night, have been a model of hard work all these years.

I remember how Patricia and Lourdes received me in the Lab. Although the work carried out with Patricia during my first year as a PhD Student is not presented here, she opened to me the door to the underground level of the Institute and showed me the kind of hard work and discipline that my thesis project was going to need. I will never forget not only the affection and care you have always had towards me, but also the concentration level you could achieve with Beethoven at a maximum volume. You both treated everyone of us, the new ones, with respect, always had time to listen to our problems, work-wise or not, and never had a no for an answer. Together with Elena you were the three-people group, four with Susana, which seeded the lab then.

The post-docs working in the Institue showed me the maturity, the know-how and the confidence we all would like for us. Jose Requejo criticized strongly my work during the first years demanding a maximum effort in the alignment of the experimental systems as well as in the design of the simulations. Sergio Barbero guided my first steps in the implementation of the algorithms for ray tracing and optimization. He taught me to always

consider the problems in depth in order to find the beauty of the detailed work. Stephen Uhlhorn taught me the confidence as well as the down to earth philosophy that is necessary to tackle any problem. Damian Siedlecki was always the friendly hand with which I could discuss about my thesis project, or talk honestly about the problems. We usually would come up with some ideas to test, and some of those would later become papers. This thesis would not have been the way it is now without any of you.

As you can see in the manuscript, Ophtalmic Biophysics Center of the Bascom Palmer Eye Institute has a big share in this thesis. David, Stephen, Fabrice and Jean Marie trained me in the lab techniques that I would need, helped me to solve the problems I found on the way, and provided unique data and discussion that enriched this manuscript from the first to the last page.

Working in the project has been easier with the help of many people of the Institute. Among all of them, i have to thank especially Marcial Galván and Sergio Ortiz. Marcial taught me patiently, clearly, and in a single week the way to deal with genetic algorithms as well as the important points that i should study to make them converge to a solution in a limited time. Sergio helped me in the experimental set up of the ray tracing with his knowledge of Visual Basic and improved the precision of the OCT data that i would use later, with the fan distortion correction algorithm.

I cannot forget here my friends from Palencia, those in which you can totally rely on even if time has made us so different, nor those I've met in the institute during this years. I've had a lot of fun with you in our coffee breaks and "fast pitis" at the door of the Institute, in "el gallego" (the one near the institute or the one far away), la Deportiva, Lavapiés or la Latina. You have supported me in the hard moments and you have helped me forget the problems for a while in the really bad ones. I enjoyed the shared moments in Madrid and i hope we will share much more.

To my family, that has constantly supported me without understanding what was taking so much time to finish (i couldn't explain them then and i cannot do it now either), i have to thank a lot. You have encouraged me since i was a kid but showed me always how the important is never in the achievement itself but enjoying the preparation. In family I have to include also the French branch who came with Lucie. You embraced me as one more since the first moment. To Lucie I have all to thank. She knows why but i'm not able to find the words to write the reason here.